UNIVERSITY OF CALIFORNIA

Santa Barbara

Metal-Organic Chemical Vapor Deposition of N-polar InGaN and InN for Electronic Devices

A dissertation submitted in partial satisfaction of the

requirements for the degree Doctor of Philosophy

in Chemistry

by

Cory Christopher Lund

Committee in charge:

Professor Umesh K. Mishra, co-chair

Professor Steven P. DenBaars, co-chair

Professor Ram Seshadri, co-chair

Professor Shuji Nakamura

Professor Martin Moskovits

Dr. Stacia Keller

January 2018

The dissertation of Cory Christopher Lund is approved.

_____

Umesh K. Mishra, co-chair

_____

Steven P. DenBaars, co-chair

_____

Ram Seshadri, co-chair

_____

Shuji Nakamura

_____

Martin Moskovits

_____

Stacia Keller

December 2017

Metal-Organic Chemical Vapor Deposition of N-polar

InGaN and InN for Electronic Devices

by

Cory Christopher Lund

ACKNOWLEDGEMENTS

First and foremost, I would like to thank Dr. Stacia Keller for her guidance and advice throughout my time at UCSB. I had the great pleasure of being trained in hands-on MOCVD growth by Stacia when I first arrived at UCSB, a luxury that few have been able to enjoy in recent years. Through countless discussions, her expertise and intuition into the MOCVD growth process as well as general experimental design has helped shape me into the scientist that I am today.

Next, I would like to thank my primary PhD advisors, Profs. Umesh Mishra and Steve DenBaars. When I visited UCSB before deciding to enroll, the Chemistry Department visitation committee had randomly scheduled me for a meeting with Steve even though he was outside the department. He was willing to work with me even though my background was not in materials or even physics, and when he showed me a packaged LED grown and fabricated at UCSB, I knew instantly that this was what I wanted to pursue. Eventually, I came to be co-advised by Steve and Umesh, and have truly enjoyed working in both groups. As for Umesh, I have often referred to him as “the most interesting man in the world” when telling my friends and family about my time in his lab. I am continually impressed by his passion, innovation, and knowledge not only in GaN devices but also in world politics, economics, and life in general. I would also like to thank the rest of my committee, Profs. Shuji Nakamura, Ram Seshadri, and Martin Moskovits, for their support and guidance. Although our interactions were minimal in time, I appreciate the conversations that we’ve had that help me to put my work into perspective.

The work presented in this thesis could not have been accomplished without the efforts of a team of people working towards a common goal. On the more practical side, I would like to thank Brian Romanczyk for all of our discussions on device fabrication. Whenever I encountered a problem related to processing or electrical measurements, Brian was my go-to resource. I would like to acknowledge Karine Hestroffer for all of the time she spent growing MBE samples for me. Her work provided me with the material needed for one entire project, which made up a significant portion of my thesis. I would also like to thank my fellow growers including Abdullah, Chris, Silvia, Matt L., Anchal, John, Charles, Haoran, Elahe, Nirupam, and Jing for all of our fruitful discussions, as well as for commiserating with me when things didn't go as planned. The entire Mishra group was also a key part of my PhD experience, including Matt G., Chirag, Onur, Maher, Steven, Christian, Xun, Geetak, Trey, and Jeong.

Finally, I would like to thank my family and friends for being there for me throughout this process. My wife, Alicia, has been my biggest supporter and confidant since before we were even in graduate school. I can't begin to imagine what it would've been like to go through the last 5 years without the emotional and physical support she provided throughout the journey that is grad school (all while going through grad school herself). I am also very thankful for the encouragement that my family provided throughout my whole life, including my parents, Chris and Jody, my brothers, Spencer and Drew, my aunt and uncle, Steph and Rick, and my Grandma, Anna Mae. They were always there for me when I was discouraged or didn't know which steps to take next. Last, I would like to thank all of my friends who helped me to unwind and experience life outside of work, including Josh, Zach, Eric, Sam, Tom, Dana, Ryan, and Lexi. I strongly believe in having a healthy work-life balance, and these people all made this possible even during graduate school.

VITA OF CORY CHRISTOPHER LUND

EDUCATION

Ph.D. in Chemistry **January 2018**
University of California, Santa Barbara, CA

B.S. in Chemistry, minors in Physics and Materials Science **June 2011**
Western Washington University, Bellingham, WA

RESEARCH EXPERIENCE

Doctoral Researcher under Umesh Mishra and Steven DenBaars **July 2012 – Present**
University of California, Santa Barbara, CA

- Performed epitaxial growth of III-Nitride films for optoelectronic and electronic applications using metal-organic chemical vapor deposition
- Conducted preventative maintenance and repairs on MOCVD reactor
- Characterized thin films using AFM, XRD, SEM, PL, CL, Hall, and IV measurements
- Fabricated diodes and patterned substrates using optical and holographic lithography techniques

Undergraduate Researcher under David Patrick **June 2008 – June 2011**
Western Washington University, Bellingham, WA

- Built and maintained a scanning tunneling microscope (STM) to operate at room temperature and pressure
- Studied self-assembly of liquid crystal films on surfaces using STM

TEACHING EXPERIENCE

Private tutor in high school and college level math, chemistry, and physics **2009-2016**

Taught 3 quarters physical/inorganic and general chemistry laboratory
University of California, Santa Barbara, CA **2012-2014**

Lead tutor at campus tutoring center
Western Washington University, Bellingham, WA **2010-2011**

Tutor in math, chemistry, and physics at campus tutoring center
Western Washington University, Bellingham, WA **2009-2011**

HONORS

Chemistry Dept. Service Award, University of California, Santa Barbara **2014**

PUBLICATIONS

C. Lund, M. Catalano, L. Wang, C. Wurm, T. Mates, M. Kim, S. Nakamura, S.P. DenBaars, U.K. Mishra, and S. Keller, "Metal-organic chemical vapor deposition of N-polar InN quantum dots and thin films on vicinal GaN," *J. Appl. Phys.* (accepted Jan. 2018).

C. Lund, K. Hestroffer, N. Hatui, S. Nakamura, S.P. DenBaars, U.K. Mishra, and S. Keller, "Digital growth of thick N-polar InGaN films on relaxed InGaN pseudo-substrates," *Appl. Phys. Express* **10**, 111001 (2017).

C. Lund, B. Romanczyk, M. Catalano, Q. Wang, W. Li, D. DiGiovanni, M.J. Kim, P. Fay, S. Nakamura, S.P. DenBaars, U.K. Mishra, and S. Keller, "Metal-organic chemical vapor deposition of high quality, high indium composition N-polar InGaN layers for tunnel devices," *J. Appl, Phys.* **121**, 185707 (2017).

C. Lund, S. Nakamura, S.P. DenBaars, U.K. Mishra, and S. Keller, "Growth of high purity N-polar (In,Ga)N films," *J. Cryst. Growth* **464**, 127 (2017).

K. Hestroffer, **C. Lund**, O. Koksaldi, H. Li, G. Schmidt, M. Trippel, P. Veit, F. Bertram, N. Lu, Q. Wang, J. Christen, M.J. Kim, U.K. Mishra, and S. Keller, "Compositionally graded InGaN layers grown on vicinal N-face GaN substrates by plasma-assisted molecular beam epitaxy," *J. Cryst. Growth* **465**, 55 (2017).

C. Gupta, **C. Lund**, S.H. Chan, A. Agarwal, J. Liu, Y. Enatsu, S. Keller, and U.K. Mishra, "In Situ Oxide, GaN Interlayer-Based Vertical Trench MOSFET (OG-FET) on Bulk GaN substrates," *IEEE Elec. Device Lett.* **38**, 353 (2017).

B. Bonef, M. Catalano, **C. Lund**, S.P. DenBaars, S. Nakamura, U.K. Mishra, M.J. Kim, and S. Keller, "Indium segregation in N-polar InGaN quantum wells evidenced by energy dispersive X-ray spectroscopy and atom probe tomography," *Appl. Phys. Lett.* **110**, 143101 (2017).

K. Hestroffer, **C. Lund**, H. Li, S. Keller, J.S. Speck, and U.K. Mishra, "Plasma-assisted molecular beam epitaxy growth diagram of InGaN on (0001) GaN for the optimized synthesis of InGaN compositional grades," *Physica Status Solidi B* **253**, 626 (2016).

C. Gupta, S.H. Chan, **C. Lund**, A. Agarwal, O.S. Koksaldi, J. Liu, Y. Enatsu, S. Keller, and U.K. Mishra, "Comparing electrical performance of GaN trench-gate MOSFETs with a-plane (11-20) and m-plane (1-100) sidewall channels," *Appl. Phys. Express* **9**, 121001 (2016).

W. Li, L. Cao, **C. Lund**, S. Keller, and P. Fay, "Performance projection of III-nitride heterojunction nanowire tunneling field-effect transistors," *Phys. Status Solidi A* **213**, 905 (2016).

M. Tahhan, J. Nedy, S.H. Chan, **C. Lund**, H. Li, G. Gupta, S. Keller, and U.K. Mishra, "Optimization of a chlorine-based deep vertical etch of GaN demonstrating low damage and low roughness," *J. Vacuum Sci. & Technol. A: Vacuum, Surfaces, and Films* **34**, 031303 (2016).

S. Keller, **C. Lund**, T. Whyland, Y. Hu, C. Neufeld, S. Chan, S. Wienecke, F. Wu, S. Nakamura, J.S. Speck, S.P. DenBaars, and U.K. Mishra, "InGaN lattice constant engineering via growth on (In,Ga)N/GaN nanostripe arrays," *Semicond. Sci. Tech.* **30**, 105020 (2015).

K. Hestroffer, F. Wu, H. Li, **C. Lund**, S. Keller, J.S. Speck, and U.K. Mishra, "Relaxed c-plane InGaN layers for the growth of strain-reduced InGaN quantum wells," *Semicond. Sci. Technol.* **30**, 105015 (2015).

X. Liu, R. Yeluri, J. Kim, S. Lal, A. Raman, **C. Lund**, S. Wienecke, J. Lu, M. Laurent, S. Keller, and U.K. Mishra, "In-situ metalorganic chemical vapor deposition and capacitance-voltage characterizations of Al2O3 on Ga-face GaN metal-oxide-semiconductor capacitors," *Appl. Phys. Lett.* **103**, 053509 (2013).

R. Thompson, **C. Lund**, S.A. Hickman, E. Krohn, and D.L. Patrick, "Stamping oriented molecular monolayers using liquid crystal inks," *Chem. Commun.* **47**, 7668 (2011).

INVITED CONFERENCE PRESENTATIONS

C. Lund, B. Romanczyk, M. Catalano, Q. Wang, W. Li, M.J. Kim, P. Fay, S. Nakamura, S.P. DenBaars, U.K. Mishra, and S. Keller, "Growth of high purity N-polar (In,Ga)N films for tunnel devices," Invited oral presentation delivered at the International Conference on Metal Organic Vapor Phase Epitaxy, San Diego, California, 2016.

CONFERENCE PRESENTATIONS

C. Lund, K. Hestroffer, N. Hatui, S. Nakamura, S.P. DenBaars, U.K. Mishra, and S. Keller "Enhanced indium incorporation into N-polar (In,Ga)N films grown on relaxed InGaN pseudo-substrates," Oral presentation delivered at the International Conference on Nitride Semiconductors, Strasbourg, France, 2017.

C. Lund, M. Catalano, L. Wang, T.E. Mates, M.J. Kim, S. Nakamura, S.P. DenBaars, U.K. Mishra, and S. Keller, "MOCVD growth of N-polar InN quantum dots and thin films on vicinal GaN," Poster presentation delivered at the International Conference on Nitride Semiconductors, Strasbourg, France, 2017.

C. Lund, B. Romanczyk, M. Catalano, Q. Wang, W. Li, N. Lu, M.J. Kim, P. Fay, S. Nakamura, S.P. DenBaars, U.K. Mishra, and S. Keller, "Growth of high quality N-polar $In_xGa_{1-x}N$ films with $x > 0.4$ for tunnel junction devices," Oral presentation delivered at the International Workshop on Nitride Semiconductors, Orlando, Florida, 2016.

C. Lund, S. Keller, T. Wyland, F. Wu, S.H. Chan, C. Neufeld, S. Nakamura, S.P. DenBaars, J.S. Speck, and U.K. Mishra, "Impact of the stripe geometry on the optical and structural properties of InGaN films grown on InGaN stripe arrays," Oral presentation delivered at the International Symposium on Compound Semiconductors, Santa Barbara, California, 2015.

C. Lund, S. Keller, T. Wyland, F. Wu, S.H. Chan, C. Neufeld, S. Nakamura, S.P. DenBaars, J.S. Speck, and U.K. Mishra, "Impact of the stripe geometry on the relaxation behavior of InGaN/GaN MQW nanostripe arrays," Poster delivered at SPIE Photonics West, San Francisco, California, 2014.

ABSTRACT

Metal-Organic Chemical Vapor Deposition of N-polar

InGaN and InN for Electronic Devices

by

Cory Christopher Lund

While most commercial gallium nitride (GaN) devices are grown in the (0001) Ga-polar orientation, the N-polar $(000\bar{1})$ orientation is advantageous for heterostructures which can benefit from reversed polarization fields including transistors, photodetectors, solar cells, and optoelectronic devices. One particularly attractive application is tunnel junctions, since GaN/(In,Ga)N/GaN tunnel junction devices rely on the piezoelectric polarization in the N-polar orientation. In these devices the tunneling probability is proportional to the indium composition in the InGaN layer, motivating the investigation of the upper limit of indium incorporation in N-polar InGaN layers embedded into GaN. Devices with high indium mole fraction active regions (>0.25) typically suffer from high defect densities and low quantum efficiency, primarily due to 1) the large 10% lattice mismatch between InN and GaN, and 2) the low thermal stability of InN, requiring significantly lower deposition temperatures compared to GaN layers. The work presented in this thesis addresses the above challenges in multiple ways.

First, the deposition of N-polar InGaN layers for tunnel devices will be detailed including the optical, structural, and electrical properties of layers with indium compositions up to 0.46. The electrical performance of N-polar GaN/$In_{0.35}Ga_{0.65}N$/GaN tunnel diodes will be discussed,

including temperature-dependent measurements which confirmed tunneling behavior under reverse bias.

Second, the growth of N-polar InN quantum dots and thin films on vicinal GaN base layers will be presented. For thin layers, quantum dot-like features were spontaneously formed to relieve the strain between the InN and GaN layers. For thicker layers above 10 nm, high electron mobilities up to 706 cm^2/Vs were measured using Hall effect measurements indicating high quality layers. The properties of GaN/InN/GaN double heterostructures will be presented as well.

Next, the use of lattice-engineered InGaN pseudo-substrates (PSs) as base layers for InGaN deposition will be discussed as a strategy to mitigate the lattice mismatch when growing layers with high indium content. Relaxed N-polar InGaN films were grown by MOCVD on N-polar InGaN PSs using a novel digital approach which enabled the deposition of thick layers while maintaining smooth surfaces, and InGaN/GaN multiple quantum wells were deposited on both N-polar and Ga-polar InGaN PSs. The use of the InGaN PSs resulted in InGaN layers with about 50% higher In compositions and enhanced optical properties compared to those grown on traditional GaN templates.

Finally, the impurity incorporation behavior of N-polar layers grown at reduced temperatures in the InGaN growth regime will be presented along with the growth and process optimization for the fabrication of reduced temperature p-GaN layers. Although the majority of this thesis focuses on the growth of indium-containing layers, these studies are useful for the fabrication of N-polar devices grown at low temperatures. By minimizing the impurity incorporation and optimizing the p-GaN growth process, p-contact resistances as low as 2.77 $m\Omega cm^2$ were achieved.

TABLE OF CONTENTS

I. Introduction

With a widely tunable direct bandgap ranging from 0.7-6.2 eV, the (In,Al,Ga)N alloy system has many attractive applications in optoelectronic and electronic devices including light emitting diodes, lasers, photodetectors, transistors, and tunnel diodes.[1–5] Most devices to date are grown using either metal-organic chemical vapor deposition (MOCVD) or molecular beam epitaxy (MBE) and consist of alloys with lattice parameters close to that of GaN which are typically grown on bulk GaN, sapphire, SiC, or Si substrates (Figure 1.1). Success in optoelectronic applications so far has been in devices emitting in the ultraviolet to green regime, with InGaN active regions containing up to around 25% indium which can be grown with high quality. In general, the internal quantum efficiency decreases with increasing indium mole fraction and the emission wavelength shifts from blue towards longer wavelength.[1] This effect is more pronounced at longer wavelengths, which is often referred to as the 'green gap'.[6]

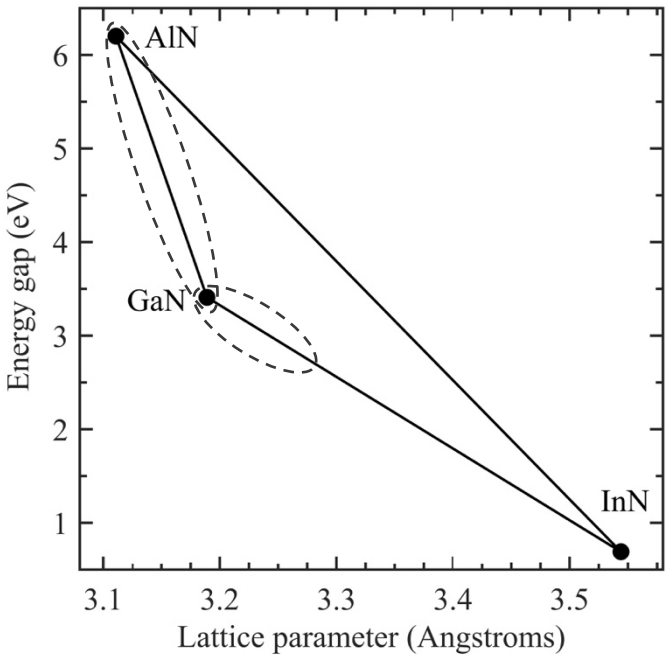

Figure 1.1. Energy band gaps and in-plane lattice constants of III-N alloys (bowing parameters neglected). Dashed ellipses indicate alloys which are used in most applications to date.

The diminished performance with increasing wavelength is related to several factors. (I) With increasing In content in the active region, the lattice mismatch increases, reaching 10% for pure InN on GaN. As the In content in the $In_xGa_{1-x}N$ QW increases, the QW thickness has to be reduced to suppress strain-related defect formation.[7] The use of very thin InGaN layers to avoid such defect formation, on the other hand, leads to a reduced Stokes shift[8] and increased confinement resulting in a blue shift of the emission and requiring even higher indium compositions.[9] (II) Due to the low thermal stability of InN, which begins decomposing around 500 ºC, the growth temperature for InGaN films must be significantly lower than the optimal growth temperature of GaN (~1000 °C) and even lower as the indium composition is increased. This further increases the probability of defect formation due to the reduced surface mobility of adsorbed species and inefficient pyrolysis of the typical N-precursor, NH_3.[10,11] In addition, (III) the incorporation efficiency of C and O impurities increases at lower temperatures.[12] (IV) The indium incorporation efficiency decreases with increasing lattice mismatch at typical MOCVD growth temperatures, known as composition pulling, which again necessitates even lower temperatures to achieve a high In content.[13–15] Finally, (V) as the strain increases in an InGaN/GaN heterostructure grown in the typical *c*-direction the magnitude of the induced piezoelectric field increases, causing electron-hole separation and reducing recombination efficiency as well as causing a blue shift in emission with increasing carrier density.[16] The above factors create serious challenges for the growth of high indium composition InGaN QWs. Most InGaN films reported in the literature contain less than around 30% indium. While some groups have reported the growth of nominal In-polar InN quantum wells,[17] recent analysis has indicated that due to surface reconstruction during growth the true composition of these layers may be around 33%.[18,19]

1.1 N-polar InGaN growth

While the above factors apply to any crystallographic orientation, there have been reports indicating that the indium uptake efficiency is higher for films grown in orientations other than the most commonly used (0001) +c-orientation. Some semipolar planes have been shown to have higher indium uptake efficiencies compared to c-plane growth,[20] and semipolar and nonpolar devices have shown significant potential in light-emitting applications due to the reduced polarization-induced quantum confined Stark effect (QCSE) in these orientations.[21,22] There are also reports of higher indium incorporation efficiency into $(000\bar{1})$ N-polar films.[23–25] The N-polar $(000\bar{1})$ orientation has a reversed polarization direction compared to the (0001) Ga-polar orientation (Figure 1.2),[26,27] which can be utilized for numerous device structures such as GaN/AlGaN high electron mobility transistors (HEMTs),[28–31] light emitters,[32–36] detectors,[37,38] and solar cells.[39]

Growth in the N-polar orientation using MOCVD is in general far less explored than the Ga-polar orientation, largely due to the initial difficulty in obtaining smooth layers with low

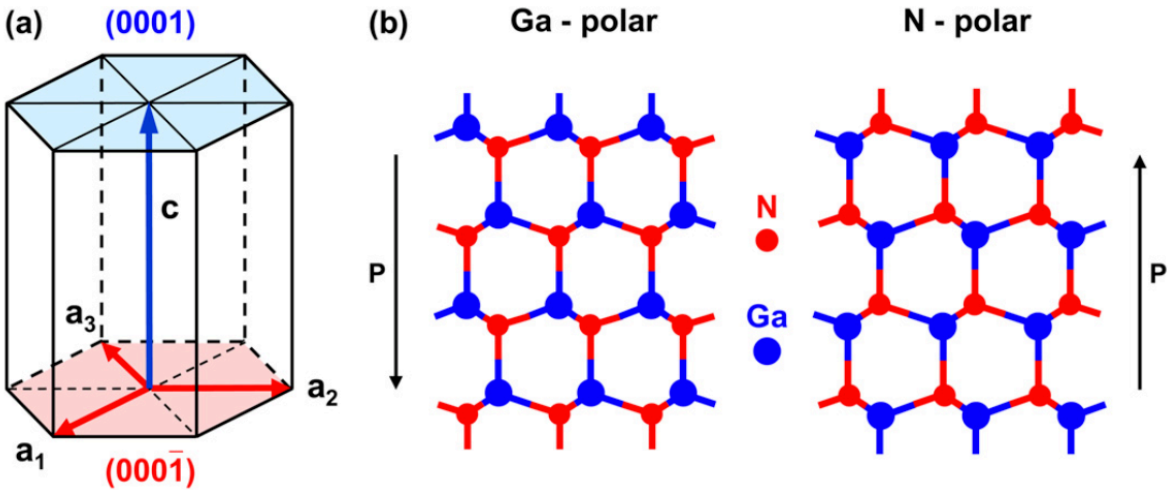

Figure 1.2. a) Illustration of polar planes in wurtzite (Al,Ga,In)N, as well as b) atomic structure of Ga- and N-polar films, indicating the direction of the spontaneous polarization fields in each orientation. (Figure from Ref. 27)

impurity incorporation. However, the use of miscut substrates allows for the deposition of smooth layers,[40,41] and with careful optimization of the growth process the impurity levels in N-polar layers can be decreased to that of Ga-polar layers.[42–44] Nevertheless there are very few groups which have extensively explored N-polar InGaN growth using MOCVD. The majority of the work published on N-polar InGaN growth by MOCVD outside of UCSB has come from the group of Prof. Takashi Matsuoka at Tohoku University in Japan, primarily focusing on the growth of alloys with less than around 25% indium for applications in optoelectronic devices, with little focus on higher composition InGaN alloys or electronic applications.

1.2 Synopsis of this thesis

The work presented in this thesis covers multiple aspects relevant to the growth of devices which utilize high indium contents. While specific device applications are covered in some chapters, this work is primarily meant to expand the toolbox of techniques available for the fabrication of any devices which require high indium contents and low growth temperatures. Additionally, although most of the work in this thesis focuses on N-polar material, the majority of the observed trends remain true for the Ga-polar orientation, and in some cases Ga-polar results will be presented. Chapter II will begin with the growth optimization of N-polar InGaN layers with high In compositions for use in tunnel devices. This chapter will outline the optimization of MQW stacks for maximum indium incorporation through the tuning of the well and barrier growth conditions, reaching a maximum indium content of 0.46. The fabrication of tunnel diodes which utilize the optimized InGaN growth procedure will be presented as well, with preliminary device results.

In Chapter III, the deposition of pure InN films on GaN will be discussed. Due to the large misfit strain between InN and GaN, the first part of this chapter will focus on the structural evolution and relaxation behavior of InN films less than 5 nm thick. In addition, the effects of the InN growth conditions on the electrical properties of InN layers up to 60 nm thick will be presented.

Chapters IV and V outline two different investigations of lattice-engineered substrates with lattice constants larger than GaN in order to reduce the strain in InGaN layers with high indium contents. Chapter IV presents an approach based on the mechanical patterning of a strained Ga-polar InGaN layer which allows the layer to partially relax. The geometry of patterned InGaN layers will be discussed as a means to control the relaxation process and avoid plastic relaxation via defect formation. Chapter V will discuss the regrowth of N-polar InGaN layers on relaxed InGaN pseudo-substrates (PSs) produced by MBE, including the regrowth optimization for the fabrication of 200 nm thick InGaN layers with smooth surfaces and a comparison between InGaN layers grown on InGaN PSs and those grown on traditional GaN templates. In addition, the regrowth of multiple quantum well structures using both N- and Ga-polar InGaN PSs will be presented.

Chapter VI focuses on the O and C impurity incorporation into low-temperature N-polar layers, in a regime relevant to (In,Ga)N and p-GaN layer deposition. For high-quality devices, it is critical to control the impurity incorporation to avoid non-radiative recombination and compensation of Mg acceptors in p-layers, although at low temperatures this process becomes more difficult.

Chapter VII will present the reduced temperature growth and fabrication of N-polar p-GaN for implementation in devices with high indium contents where the p-layer growth

temperature must also be conservative. The effects of the Mg doping scheme and various processing parameters on the electrical properties of N-polar p-GaN layers grown at reduced temperature will be discussed in detail. Finally, Chapter VIII will briefly summarize the work presented in the previous chapters and discuss potential pathways for further improving the quality of high indium content active regions and devices which utilize these layers.

II. Growth of N-polar $In_xGa_{1-x}N$ with x > 0.4 for Tunnel Devices

As discussed in Chapter I, the reversed polarization field in the N-polar orientation opens up the design space for novel polarization-engineered devices. One particularly interesting application is a GaN/InGaN/GaN tunnel diode, which benefits both from the increased indium incorporation efficiency and from the polarization in the N-polar orientation.[45–48] While tunnel junctions have been fabricated with group IV and traditional III/V semiconductors using degenerately doped p-n junctions,[49–51] the wide bandgap of GaN along with limited hole concentrations due to high acceptor activation energy, limited dopant solubility, and acceptor compensation make it difficult to achieve high interband tunneling currents in GaN p-n homojunctions. An alternative approach is to use the intrinsic spontaneous and piezoelectric polarization in the wurtzite crystal structure[52,53] to reduce the tunneling barrier by inserting a strained AlN[54–56] or InGaN layer[45–48] into the p-n junction. In these structures, the high polarization charge discontinuity at a polar hetero-interface creates strong band bending over a very small distance. The energy band diagrams (BandEng[57]) of a GaN homojunction and an InGaN-based tunnel junction are shown in Figure 2.1. While GaN/AlN/GaN devices have been demonstrated, the large bandgap of AlN leads to a high tunneling resistance, lower current density, and higher operating voltages.[55] GaN/InGaN/GaN tunneling devices have been fabricated in the Ga-polar orientation by MBE with buried p-layers,[47] however the compensation of Mg acceptors by hydrogen atoms during the MOCVD growth process makes this orientation less desirable for samples grown by MOCVD since hydrogen cannot readily diffuse through n-GaN layers during post-growth thermal activation. In the N-polar orientation, such a structure can be grown with the p-layer on the top surface of the sample so

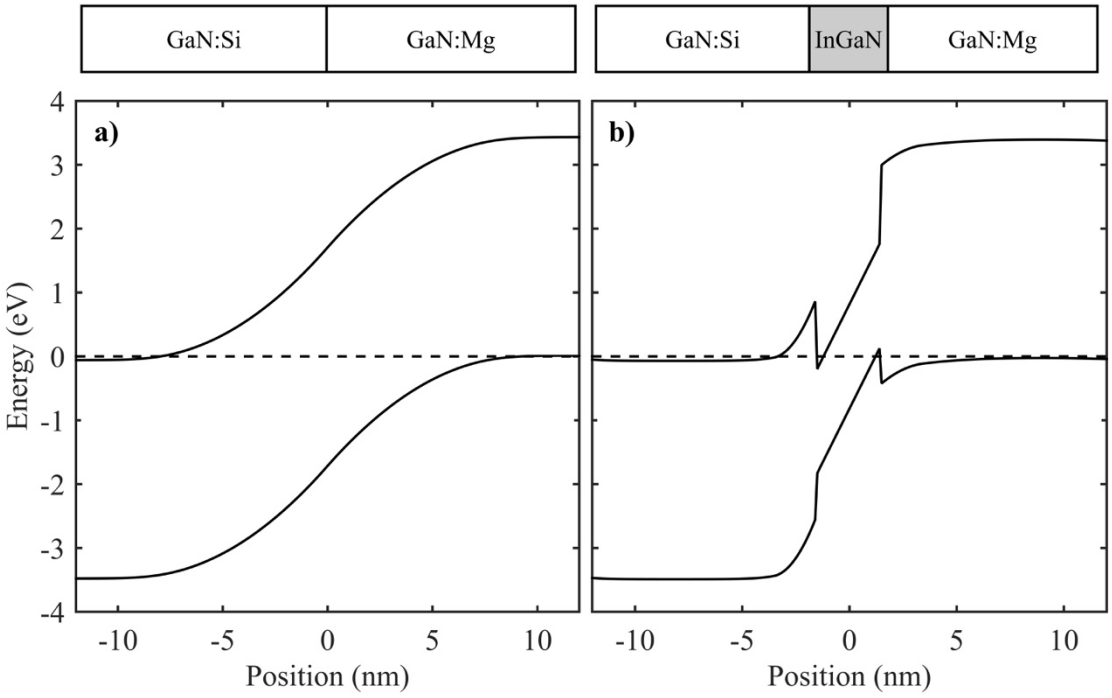

Figure 2.1. Simulated band diagram (BandEng) for a) a GaN p-n homojunction and b) a N-polar n-GaN/InGaN/p-GaN tunnel diode. The polarization-induced electric field which arises from the strained InGaN layer reduces the depletion width significantly compared to the homojunction structure with similar doping.

that hydrogen can diffuse out of the p-layer during activation. The properties of N-polar GaN/(In,Ga)N/GaN tunnel structures are discussed in detail in references [5], [45], and [48]. There are previous experimental reports of N-polar GaN/InGaN/GaN tunnel junctions grown by MBE with In compositions up to 0.40,[45,46,48] however to the best of our knowledge these structures have not been demonstrated using MOCVD.

For high tunneling currents in InGaN-based tunnel junctions, it is important to implement InGaN active regions with high indium compositions. To illustrate this point, Figure 2.2 shows the simulated on-current for a tunnel field effect transistor (TFET) which utilizes an InGaN tunnel junction. The calculated on-current in this structure is strongly dependent on the

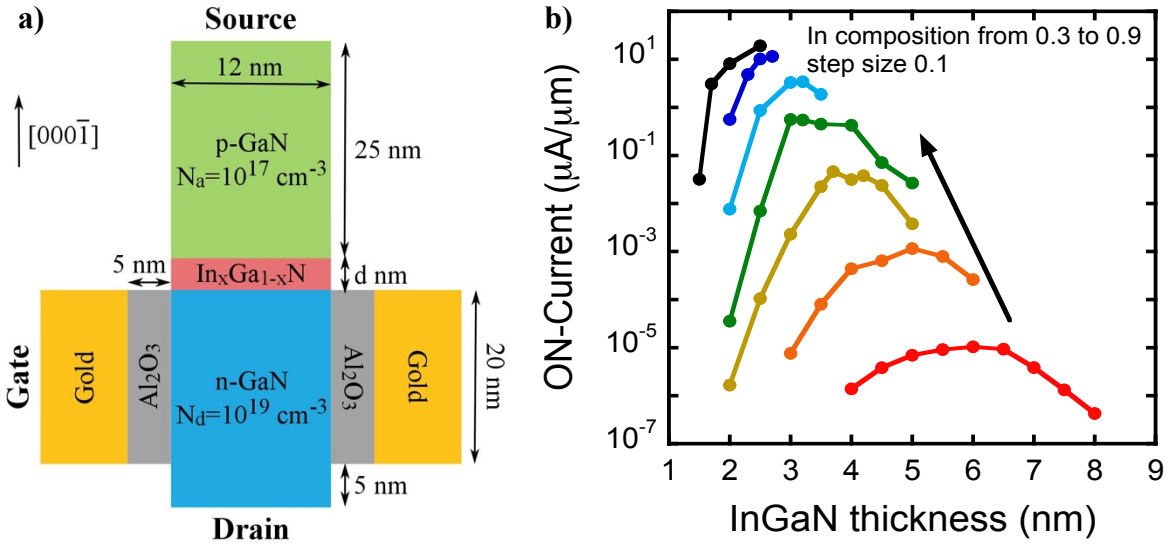

Figure 2.2. a) TFET structure used for simulations, and b) simulated on-current for TFET structures with various InGaN thicknesses and indium compositions.

composition of the InGaN layer, increasing over seven orders of magnitude as the indium composition is increased from 30 to 90%.

In this chapter, the growth of InGaN films in the N-polar orientation is presented with a focus on high indium containing layers. Short period multiple quantum well (MQW) structures were used to investigate the indium incorporation efficiency and the structural properties of N-polar InGaN active regions, while GaN/InGaN/GaN tunnel diodes were grown and fabricated to study the tunneling properties of the InGaN layers.

2.1 Growth and characterization methods for InGaN/GaN MQWs

All samples in this study were grown in an atmospheric pressure two-flow MOCVD reactor. In order to promote smooth surface morphology, the substrates used were sapphire miscut 4 degrees in the *a*-direction, corresponding to a 4 degree miscut in the GaN *m*-

direction.[40] Following nitridation of the surface, 1-2 μm thick GaN templates were grown at 1200 ºC using the procedure reported elsewhere.[27,40] To facilitate characterization of the InGaN layers, triple quantum well (QW) structures composed of 2-5 nm thick InGaN QWs were deposited at temperatures between 725-830 ºC using triethyl gallium (TEGa, 0.92-2.8 μmol/min), trimethyl indium (TMIn, 2.8-38 μmol/min), and NH_3 (1-9.5 slm) as precursors. The GaN barrier layers were grown using a two-step process[23] wherein an initial 4 nm GaN barrier was grown at the same temperature as the well using N_2 carrier gas and the remaining 6 nm GaN barrier was grown using H_2 at a temperature 30 ºC higher than the well growth temperature.

The MQW samples were characterized by room temperature (RT) photoluminescence (PL) using the 325 nm line of a He–Cd laser with an excitation density of 220 W cm^{-2}. The surface morphology was assessed using an Asylum MFP3D atomic force microscope (AFM). The structural properties were determined using x-ray diffraction (XRD). To accommodate for the miscut, the samples were oriented such that the x-ray beam was parallel to the miscut direction (perpendicular to the surface steps), and the miscut was accounted for with an offset in omega. Due to the low number of QWs and the surface undulations present from the miscut, the number of superlattice fringe peaks was limited, reducing the accuracy of the extracted layer thicknesses and compositions. To determine the true local composition and thickness, selected samples were analyzed using a scanning transmission electron microscope (STEM) equipped with an energy-dispersive x-ray (EDX) detector. The cross sectional TEM samples were prepared in a FEI Nova 200 dual-beam FIB/SEM by using the lift-out method. The TEM lamellas were prepared by cutting sections of the samples perpendicular to the [11-20]

direction so that the observation direction was perpendicular to the steps that arose from the crystal misorientation. The atomic STEM-HAADF images were obtained in a JEOL ARM200F microscope equipped with a spherical aberration (Cs) corrector (CEOS GmbH, Heidelberg, Germany) and operated at 200 kV. The corrector was carefully tuned by the Zemlin-tableau method with Cs = 0.5 μm and the resolution was demonstrated to be around 1 Å. Energy dispersive X-ray spectroscopy was performed with an Aztec Energy Advanced Microanalysis System with X-MaxN 100N TLE Windowless 100 mm^2 analytical silicon drift detector. EDX point and line scans were acquired in various regions of each sample. EDX compositions were calibrated using an $In_{0.10}Ga_{0.90}N$ reference sample. For samples where STEM/EDX analysis was not performed, the compositions and thicknesses were extracted from XRD data using a procedure which was adjusted to match STEM/EDX observations for existing samples.

2.2 Quantum well optimization for high indium content

To achieve high quality, high indium composition films, growth parameters in the well and barrier layers such as growth temperature, choice of carrier gas, and input gas flows needed to be carefully considered. One of the primary parameters that determines the solid phase indium composition, x, of the $In_xGa_{1-x}N$ layers is the input gas phase indium composition (x_g). To increase x_g, one can either increase the TMIn flow or decrease the TEGa flow. The effect of decreasing the TEGa flow with constant TMIn flow is three-fold: first, x_g is increased as previously mentioned, second, the growth rate of the layer is reduced, and third the V/III ratio during growth increases. In order to determine the effect of the growth rate and V/III ratio on the resulting InGaN layers, a series of samples was grown where both the TEGa

flow and TMIn flow were varied resulting in five pairs of samples each with the same x_g grown with two different growth rates. For each pair of samples, the resulting x was the same regardless of the growth rate however the quality of the layers as determined by AFM and XRD was higher for samples grown with the lower growth rate and higher V/III ratio. Figures 2.3a and 2.3b show 20x20 μm^2 AFM height scans of representative samples grown with the same x_g=0.835 at a temperature of 740 ˚C with growth rates of 0.22 and 0.29 Å/s, respectively. For both samples, the x in the well layers determined by XRD was 0.33 however the sample with the lower growth rate exhibited a significantly smoother surface and narrower XRD peaks, indicating higher crystalline quality and uniformity. In addition, PL emission at 550 nm was observed for the sample grown at 0.22 Å/s while the sample with the higher growth rate did not show RT PL emission. These results therefore indicated that the composition at a given temperature was primarily determined by the gas phase indium fraction, while a lower growth rate resulted in higher quality layers.

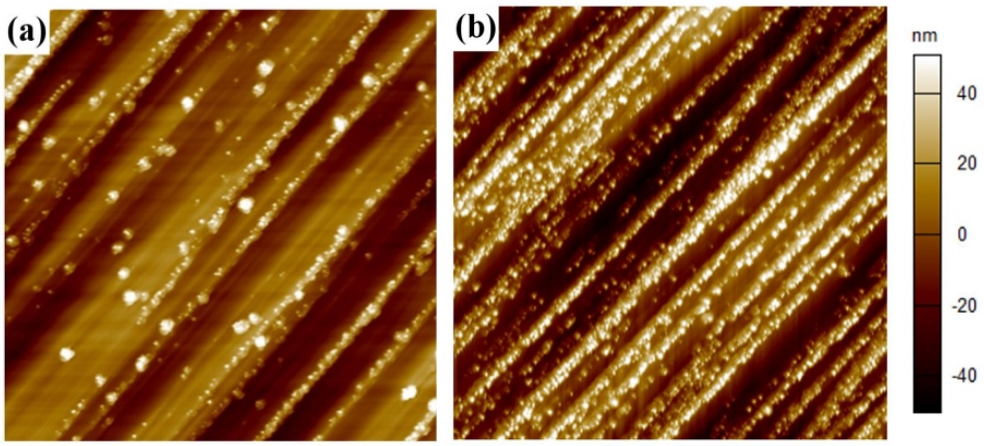

Figure 2.3. 20x20 μm^2 AFM scans of 3QW samples with well growth rates of (a) 0.22 Å/s using TEGa=1.4 µmol/min and TMIn=7.0 µmol/min, and (b) 0.29 Å/s using TEGa=1.8 µmol/min and TMIn=9.3 µmol/min. The NH_3 flow was kept constant at 6 slm. The average x determined by XRD was 0.33 for both samples, however the lower growth rate yielded a smoother surface.

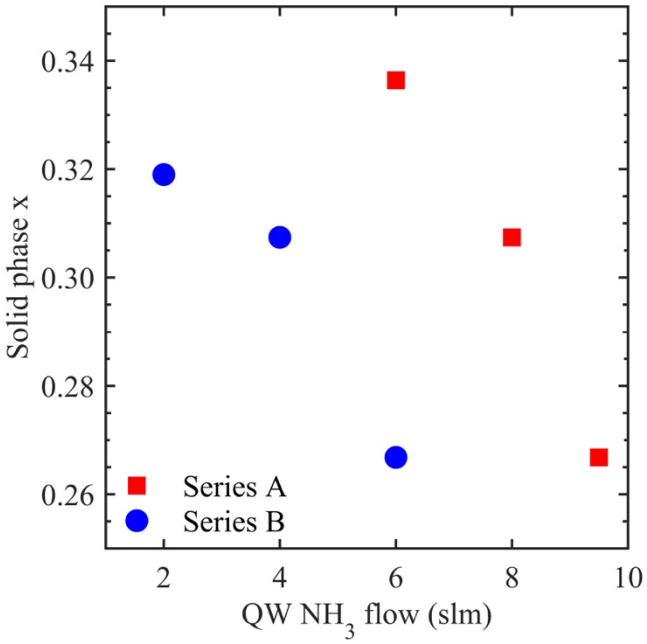

Figure 2.4. Effect of NH_3 flow during well growth on x. Series A was grown at 805 ˚C with TEGa=1.4 µmol/min and TMIn=28.0 µmol/min. Series B was grown at 770 ˚C with TEGa=1.4 µmol/min and TMIn=9.3 µmol/min.

In addition to the group III precursor flows, another critical parameter in this study was the NH_3 flow during growth. While higher NH_3 flows increase the availability of N-species this can also lead to a higher concentration of hydrogen in the growth environment which can decrease the indium uptake.[58–60] To determine the effect of NH_3 on x in the $In_xGa_{1-x}N$ QWs, two series of samples were grown. Series A was grown at 805 ˚C with TEGa=1.4 µmol/min and TMIn=28 µmol/min, while Series B was grown at 770 ˚C with TEGa=1.4 µmol/min and TMIn=9.3 µmol/min. For each series, the NH_3 flow during the well layer deposition was varied. Figure 2.4 shows the resulting x determined by XRD. For both series, within the examined flow range lower NH_3 flows yielded higher x due to the decreased concentration of hydrogen gas in the growth ambient.[59] However, for the samples in Series B grown with NH_3 flows below 6 slm the PL intensity (not shown) decreased by 4x compared to all samples with

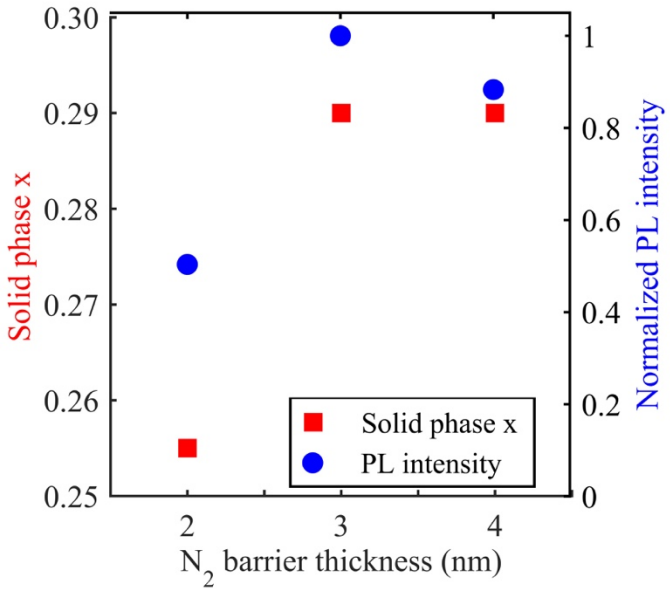

Figure 2.5. Effect of N_2 barrier thickness on x (left axis) and PL intensity (right axis). The TEGa, TMIn and NH_3 flows during well growth were 1.4 μmol/min, 28 μmol/min and 6 slm, respectively.

higher NH_3 flows due to higher impurity concentrations. Low NH_3 flows lead to an increase in the C and O residual impurity incorporation into InGaN films, especially at low growth temperatures, which prompted the investigations in the higher NH_3 flow range in this study.[44]

In addition to tuning the deposition conditions for the InGaN wells, the growth parameters for the barrier layers needed to be carefully chosen to achieve uniform thicknesses and maintain sharp interfaces and smooth surfaces. During the deposition process indium acts as a surfactant[27,61,62] and excess indium adatoms can ride on the surface leading to unintentional In incorporation into subsequent GaN barrier layers[63–66] as well as indium accumulation on the sample surface. In this study, a two-step barrier process was critical for capping the indium-containing well layers. The first part of the barrier layer was grown under the same conditions as the InGaN well using N_2 carrier gas to avoid damage to the InGaN layer.[67] After the InGaN film was sufficiently protected, H_2 was introduced and the growth temperature was

increased in order to achieve smooth barriers without forming hexagonal hillocks.[23] In order to determine the optimal thickness of the N_2 barrier, a series of samples was grown where H_2 was injected during low temperature barrier growth after 2, 3, or 4 nm of GaN growth in N_2 (Fig. 2.5). For the sample where only 2 nm GaN was grown in N_2, the resulting x was below 0.26 whereas the samples with at least 3 nm N_2 barrier resulted in a higher x around 0.29. In addition, the RT PL intensity of the sample with the thinnest N_2 barrier was reduced by a factor of two compared to samples with thicker N_2 barriers. A similar trend was previously observed for Ga-polar InGaN/GaN MQWs.[65,68]

By carefully tuning all of the parameters as discussed above, it was possible to grow MQW stacks with x up to 0.46. As the composition of the InGaN layers was increased, it was necessary to reduce the thickness of the layers in order to maintain a good surface morphology and uniform layer thicknesses. While layers with a thickness of around 5 nm could be grown with x<0.20, intermediate compositions from 0.20 to 0.35 were achievable for 3 nm thick layers, and samples with x>0.35 were grown with a well thickness around 2 nm. A 20x20 μm^2

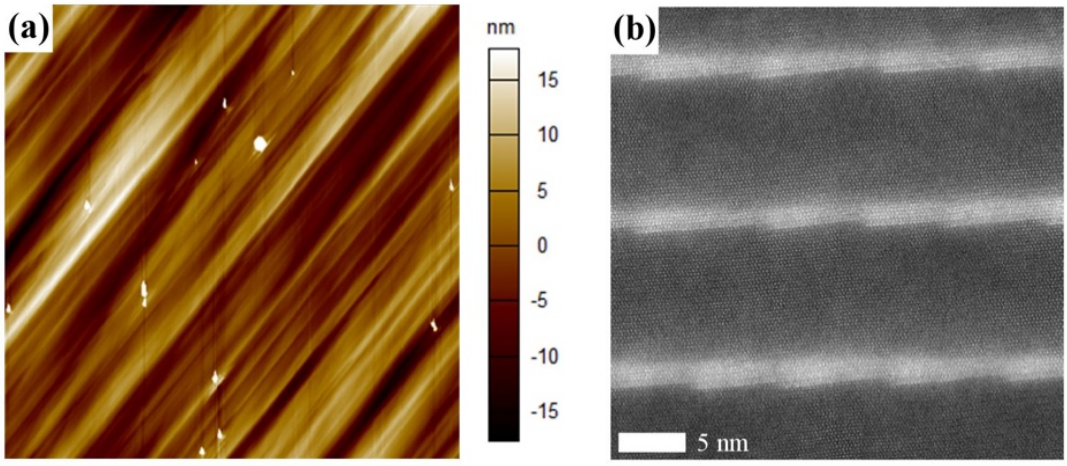

Figure 2.6. a) 20x20 μm^2 AFM image and b) cross-sectional STEM image of a sample containing $In_{0.24}Ga_{0.76}N$ QWs, which were grown with TEGa=2.8 µmol/min, TMIn=28 µmol/min and NH_3=6 slm at 770 ˚C.

AFM scan of a sample with a moderate x=0.24 is shown in Figure 2.6a. The step structure of the underlying template was maintained throughout the growth of the MQW stack, and the surface is smooth with very few indium-rich features present. Figure 2.6b depicts the cross-sectional STEM image of this sample imaged in the <11-20> direction, where the atomic steps from the misorientation are visible at the bottom interface of each well. The thickness and composition of each layer was very uniform across the sample, and EDX point scans in each well layer indicated that the average x in the wells was 0.24.

Figure 2.7a depicts a 20x20 μm^2 AFM scan of a sample with an average x of 0.44. While the density and size of the indium-rich clusters on the surface is significantly higher than in the sample with x=0.24, the underlying step structure is still visible indicating that step-flow growth was maintained. The cross-sectional STEM image of this sample is shown in Figure 2.7b. Even with a significantly higher x, excellent crystalline quality was maintained and no

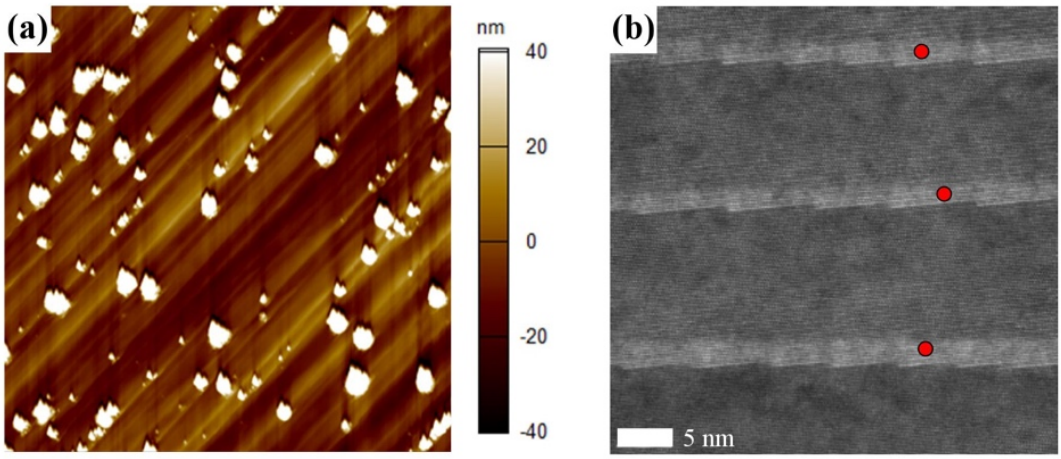

Figure 2.7. a) 20x20 μm^2 AFM image and b) cross-sectional STEM image of a sample containing $In_{0.46}Ga_{0.54}N$ QWs which were grown with TEGa=1.4 µmol/min, TMIn=28 µmol/min and NH_3=6 slm at 740 ˚C. Red circles indicate the location of EDX point scans within each QW.

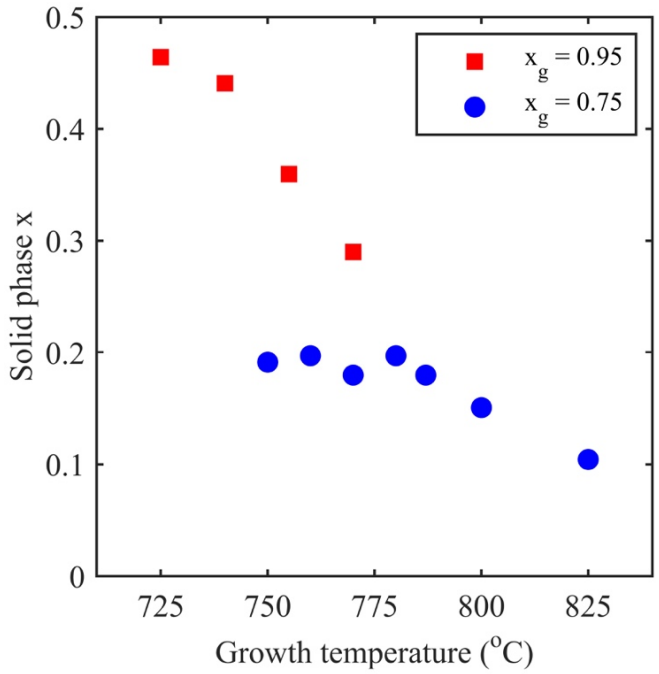

Figure 2.8. Solid phase In composition dependence on the QW growth temperature for two different x_g. Samples with x_g=0.75 were grown with TEGa=2.8 µmol/min, TMIn=8.4 µmol/min and NH_3=6 slm, while samples with x_g=0.95 were grown with TEGa=1.4 µmol/min, TMIn=28 µmol/min and NH_3=6 slm.

defect formation or strain-relaxation was observed. The In compositions determined from EDX point scans within each well layer (marked by red dots in Fig. 2.7b) amounted to 0.46, 0.44, and 0.43 from top to bottom. The indium composition of 46% extracted for the top well was the highest composition confirmed by STEM/EDX in this study. In addition, the unintentional In incorporation during the first part of the GaN barrier growth observed in both the STEM image and the corresponding EDX linescan experiments was around 0.05, comparable to Ga-polar MQWs.[65]

While all of the growth parameters studied had some impact on the structural properties and uniformity of the MQW stacks, as discussed earlier the QW composition was primarily affected by the growth temperature and x_g (Fig. 2.8 and 2.9). As expected, due to the thermal

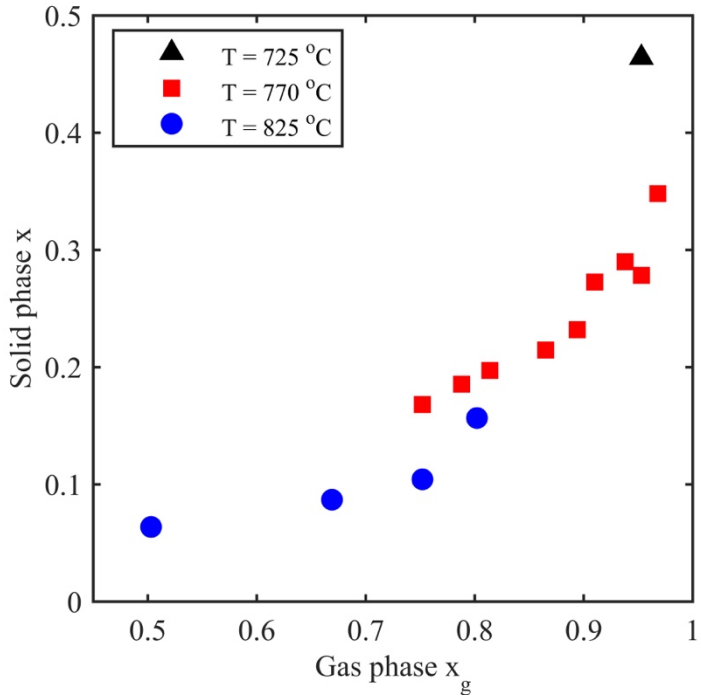

Figure 2.9. Solid phase In composition dependence on x_g at three temperatures. For each temperature, the thickness and growth rate of the layers was constant and only the TMIn flow was varied.

instability of InN, which sublimes at temperatures around 550 ºC, lower growth temperatures yielded films with higher x. The dependence of x on the QW growth temperature is shown in Figure 2.8 for two different x_g. For films with x_g=0.75, corresponding to a TEGa flow of 2.8 µmol/min and a TMIn flow of 8.4 µmol/min, x in the solid increased from 0.10 to 0.20 as the growth temperature was reduced from 825 to 770 ºC, then saturated for lower growth temperatures. In order to achieve higher In compositions, x_g was increased to 0.95 by decreasing the TEGa flow to 1.4 µmol/min and increasing the TMIn flow to 28 µmol/min. The resulting x increased significantly from 0.28 to a maximum of 0.46 when the growth temperature was further reduced from 770 to 725 ºC. For growth temperatures below 725 ºC the layer quality and uniformity declined significantly, likely due to the reduced efficiency of

NH_3 cracking at low temperatures and the increased strain in the InGaN layers[10,13,14] resulting in the tendency to form metallic In droplets on the surface rather than incorporating In into the growing film.

Figure 2.9 shows the dependence of x in the $In_xGa_{1-x}N$ QWs on x_g for three different growth temperatures. At a growth temperature of 825 ºC, In compositions between 0.08 and 0.16 were achievable by increasing x_g from 0.50 to 0.80. When the temperature was reduced to 770 ºC, higher compositions between 0.19 and 0.36 were obtained as x_g was increased from 0.75 to 0.97. As discussed earlier, in order to maintain good structural quality for samples with x>0.30, it was necessary to decrease the TEGa flow (and correspondingly decrease the growth rate and increase the V/III ratio) in addition to increasing the TMIn flow.

2.3 Luminescence properties of N-polar MQWs

Though the focus of this project was to fabricate tunnel junction devices, the optical properties of the InGaN MQW stacks were studied to gain further insight into the quality of the InGaN layers. The MQW structures in this study exhibited bright photoluminescence at room temperature ranging from blue to yellow for layers with x<0.35 (Figure 2.10). The emission wavelength increased linearly with increasing x, with a maximum wavelength of 600 nm. To achieve emission from layers with x>0.25, the thickness needed to be reduced to 2 nm. For these samples, the emission was blue shifted due to the decreased Stokes shift and the increased confinement in the thinner QWs,[8,9] resulting in emission wavelengths up to 560 nm for x<0.35. The band edge nature of the observed luminescence was confirmed in excitation dependent PL measurements (not shown). Previous temperature dependent PL

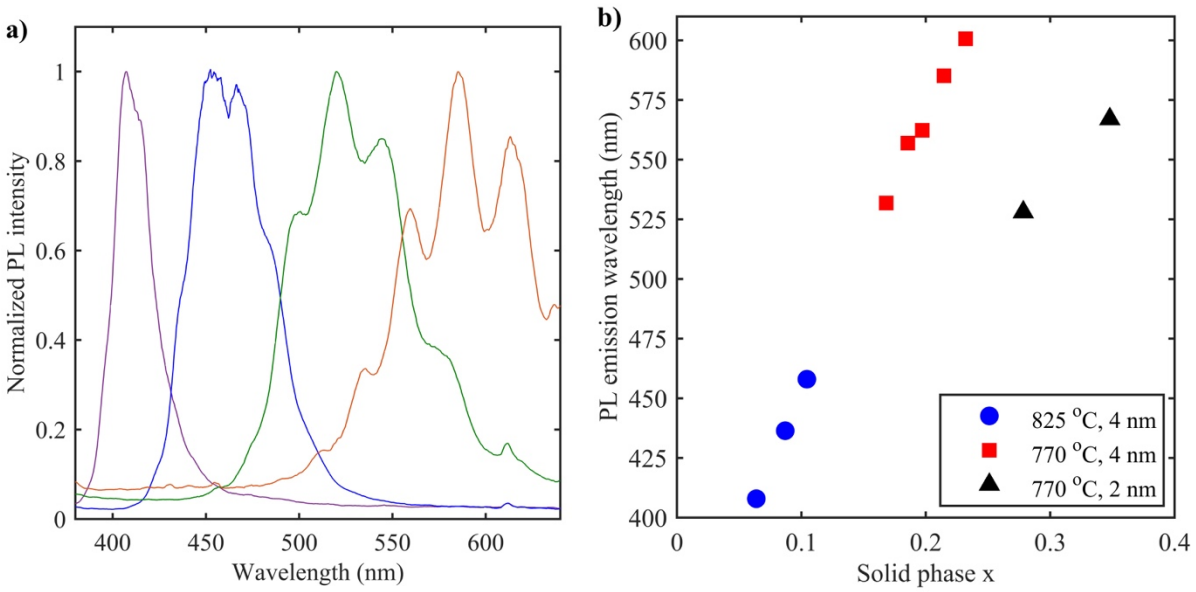

Figure 2.10. a) Representative PL spectra for samples with 4 nm thick QWs and b) dependence of RT PL emission wavelength on x. For the highest compositions, the emission is blue shifted due to the reduced thickness of the InGaN layers.

measurements on similar MQW samples also showed the band edge character of the MQW related luminescence.[27,69] While films with higher compositions were achieved, there was no observable luminescence at room temperature for these samples. This is most likely due to the circumstance that the highest composition layers were grown at very low temperatures (725-740 ºC) resulting in an increase in the unintentional incorporation of carbon and oxygen. Carbon and oxygen both incorporate predominately on the N site in GaN, forming deep acceptor and shallow donor states respectively.[70–72] In addition, both carbon and oxygen can also exist in complexes with Ga vacancies resulting in the creation of additional states within the bandgap.[73–75] These mid-gap states act as non-radiative recombination centers, decreasing the luminescence intensity.

2.4 Comparison of co-loaded N-polar and Ga-polar MQWs

In order to investigate the effect of the crystallographic orientation on the structural and optical properties of InGaN films, a separate side study was conducted where N-polar and Ga-polar MQWs were simultaneously deposited using four different gas phase indium compositions. Pieces of N-polar and Ga-polar GaN templates were co-loaded into the MOCVD reactor and InGaN quantum wells with a nominal thickness of 1.8 nm were deposited at 770 ºC using various TEGa flows according to Table 2.1. The barrier layers were grown using the two-step process discussed previously in this chapter. By changing the TEGa flow, both the growth rates and gas phase indium compositions were varied between samples. The layer structure and growth conditions for these samples are the same as for the N-polar InGaN/GaN MQWs discussed previously in this chapter.

The resulting XRD ω-2θ scans around the GaN (0004) reflection are shown in Figure 2.11 for all samples grown. According to the zero-order superlattice peak position, the Ga-polar samples contained slightly higher average indium contents in the full MQW stacks compared to their N-polar counterparts. Additionally, the Ga-polar samples resulted in a higher number of superlattice fringe peaks. Since the N-polar samples were loaded into the XRD instrument such that the incident beam was directed parallel to the miscut direction, the long-range surface undulations in this orientation reduced the intensity of the XRD reflections. The room

Table 2.1. Growth parameters for co-loaded N-polar and Ga-polar MQW growths.

TEGa flow (µmol/min)	TMIn flow (µmol/min)	R_g (Å/s)	x_{gas}
6.5	9.3	1.03	0.59
4.6	9.3	0.73	0.67
2.8	9.3	0.44	0.77
1.4	9.3	0.22	0.87

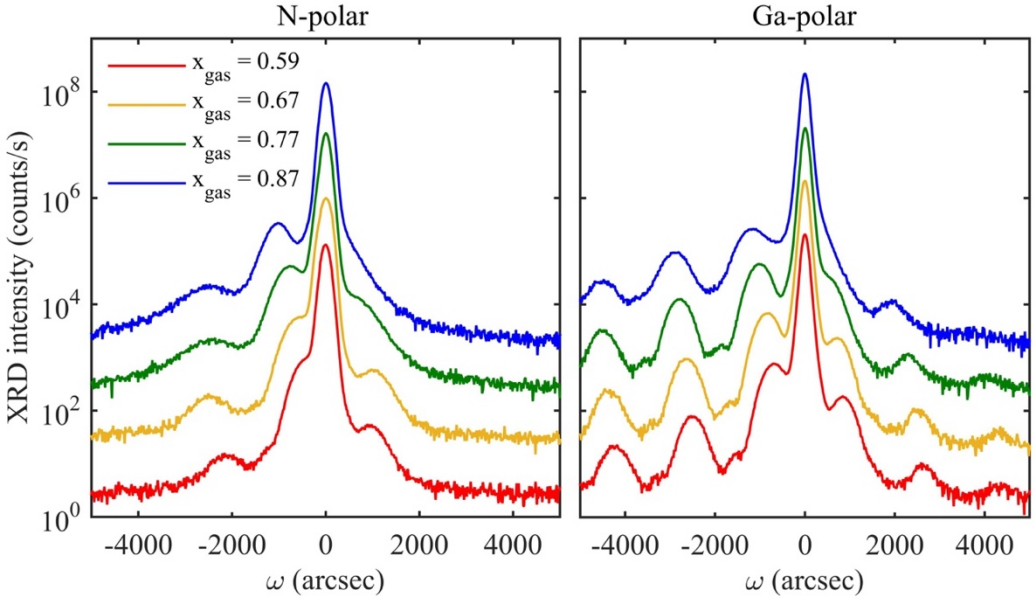

Figure 2.11. (0004) XRD ω-2θ scans for N-polar (left) and Ga-polar (right) MQW samples. For each x_{gas}, the two orientations were co-loaded together during growth.

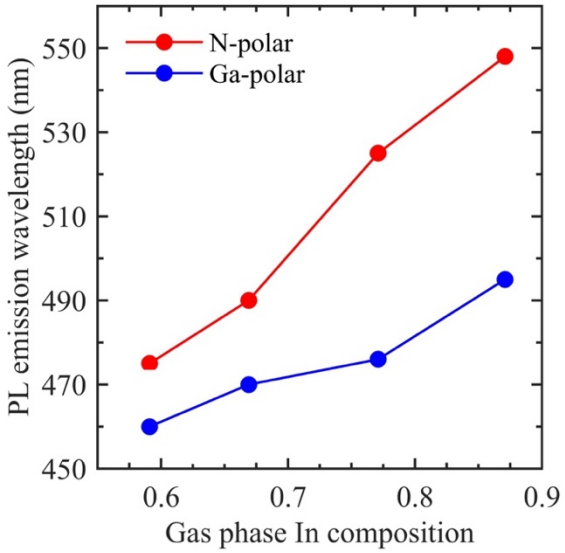

Figure 2.12. Room temperature PL emission wavelengths for N-polar and Ga-polar layers with various x_{gas}.

temperature PL emission wavelengths of these samples are presented in Figure 2.12. For each pair of co-loaded samples, the peak PL emission wavelength for the N-polar layer was 15-50 nm higher than the Ga-polar layer, with increased red shift for higher gas phase indium compositions (lower growth rates).

The local structures of the pair of samples with x_{gas}=0.87 were inspected using both STEM/EDX and atom probe tomography (APT). The results of the STEM/EDX measurements for both samples are shown in Figure 2.13. For the N-polar sample shown in Fig. 2.13a, the bottom interface of each well is atomically abrupt while the upper interface of each well is slightly less abrupt, with some indium incorporated into the GaN:N_2 barrier

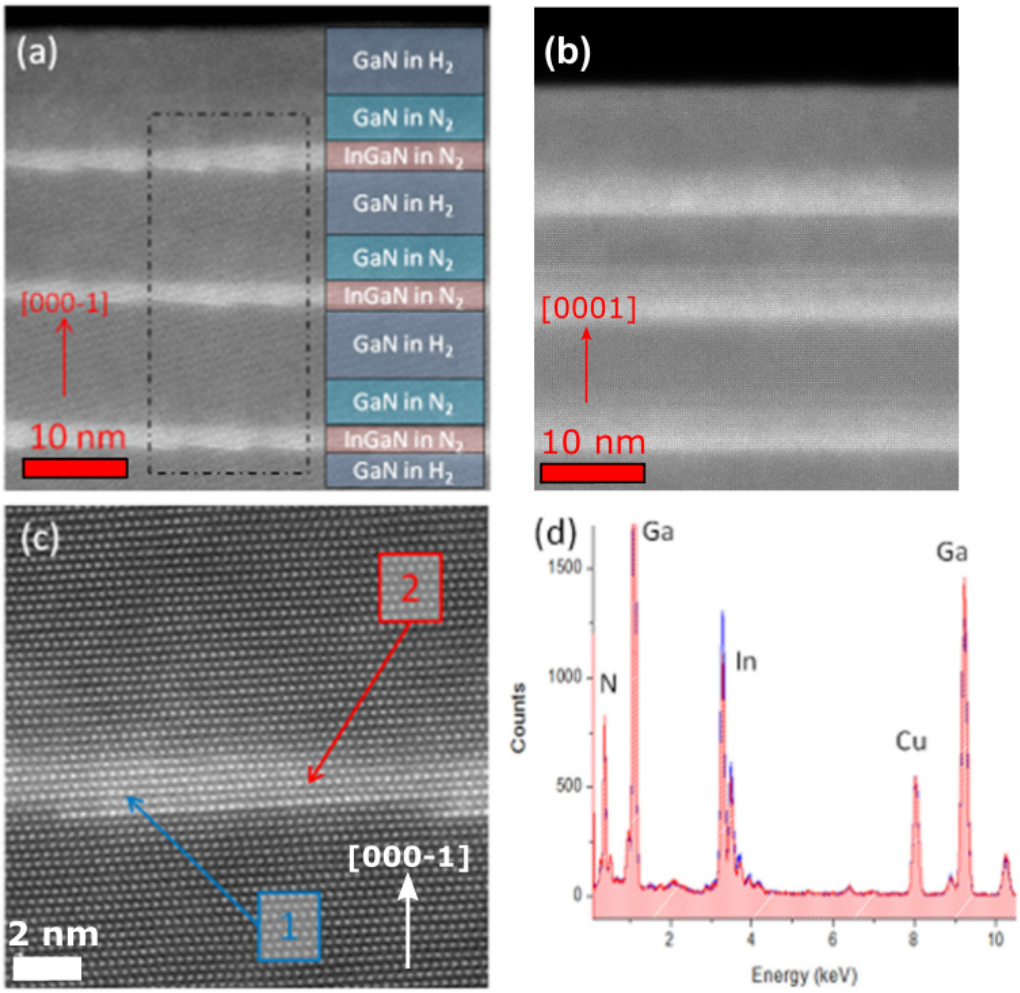

Figure 2.13. a) STEM-HAADF image of the N-polar InGaN/GaN quantum wells and barrier layers showing the growth steps. b) STEM-HAADF image of the Ga-polar InGaN/GaN quantum wells and barrier layers. c) STEM-HAADF image of the second quantum well showing a growth step and the lateral segregation of In. d) Point EDX spectrum taken on areas 1 (blue) and 2 (red) in c).

layers. In the case of the Ga-polar sample in Fig. 2.13b, the upper interface of each well layer is even more diffuse with a higher amount of indium incorporated into the GaN barriers. This effect was also observed in APT measurements on these samples, as shown in Fig. 2.14. In the N-polar sample, the wells are more clearly defined with less than around 5% indium in the barrier layers, while the Ga-polar sample contains slightly thicker well layers with triangular indium concentration profiles. In order to estimate the total amount of indium in each sample,

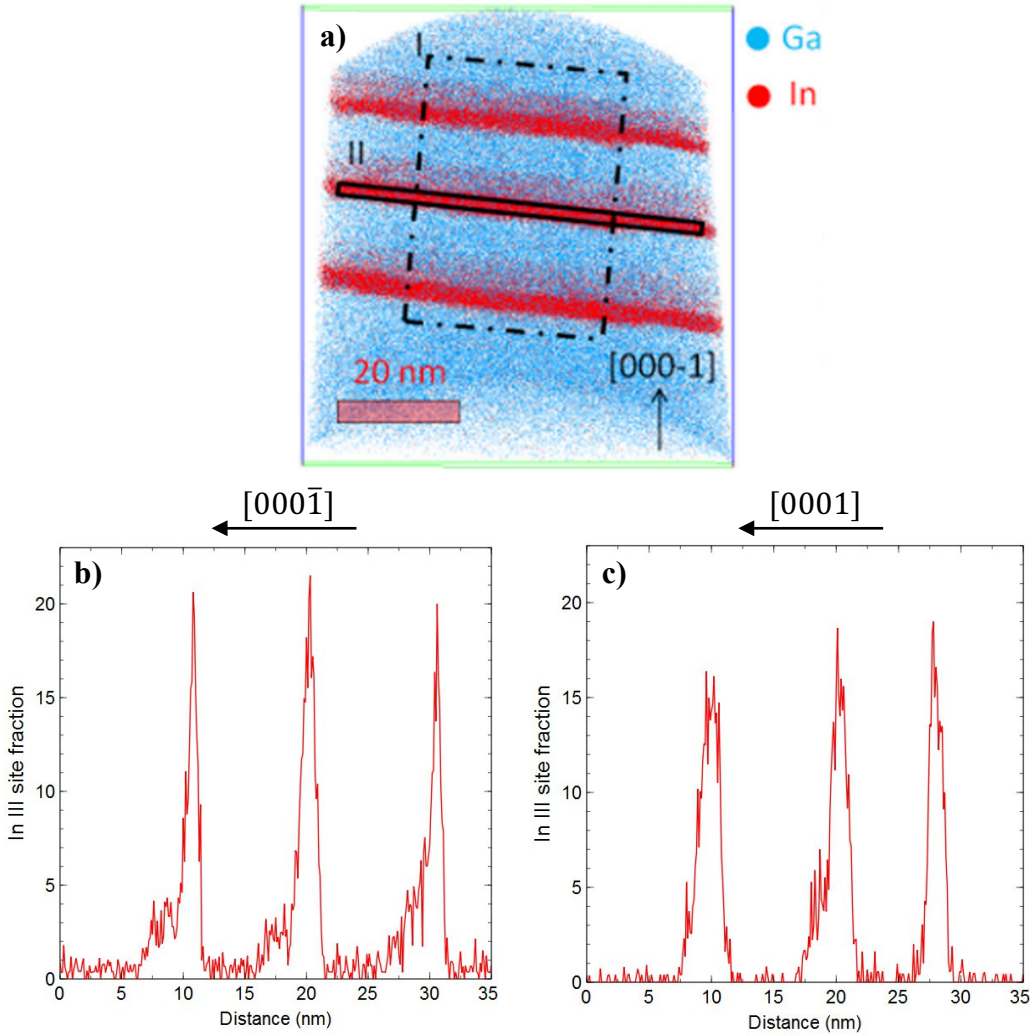

Figure 2.14. a) 3D APT reconstruction of the N-polar InGaN/GaN quantum wells and barrier layers. b) Evolution of the indium III site fraction taken from the sampling volume "I" in a). c) Evolution of the indium III site fraction in the Ga-polar sample.

the fraction of indium atoms contained within a 15x15x35 nm^3 section of the 3D APT reconstruction was calculated for each sample. The average indium content in the N-polar sample was around 2.6%, while the Ga-polar sample contained around 3.4% indium. These results agree well with the XRD observations, where the average indium content in the Ga-polar sample was slightly higher than in the N-polar sample.

In order to observe the indium distribution within the plane of the quantum wells, 2D APT maps were constructed from the second quantum well (region "II" in Fig. 2.14a) of each sample and are displayed in Figure 2.15. The N-polar sample shown in Fig. 2.15a has a higher magnitude of compositional fluctuations within the well with distinct In-rich stripes parallel to the surface steps which arise from the vicinal substrate. On the other hand, the indium distribution in the Ga-polar InGaN layer is more homogeneous with fewer In-rich clusters (Fig. 2.15b). To further investigate the compositional fluctuations, lateral In concentration profiles were extracted and are shown in Figures 2.15c-2.15d. The N-polar sample resulted in a periodic fluctuation in indium content with a larger magnitude compared to the random fluctuations observed in the Ga-polar sample, while the average indium content was similar in both samples. The indium clustering parallel to the surface steps in the N-polar sample was also observed in STEM/EDX experiments, as shown in Figure 2.13c-2.13d. Near each step edge in the N-polar sample, a higher indium content was observed compared to further out on the terrace as can be seen from the HAADF image contrast in Fig. 2.13c as well as in the EDX point spectra in Fig. 2.13d.

The increased indium content at the step edges in the N-polar sample is a result of the higher adsorption energy of indium adatoms in this position.[76] It has been previously observed

that in the N-polar orientation there is a higher occurrence of two monolayer high steps compared to the Ga-polar orientation where single monolayer high steps are typically observed. This effect was attributed to the difference in step energies of type *A* and type *B* steps on the N-polar surface due to the configuration of surface bonds in this orientation,

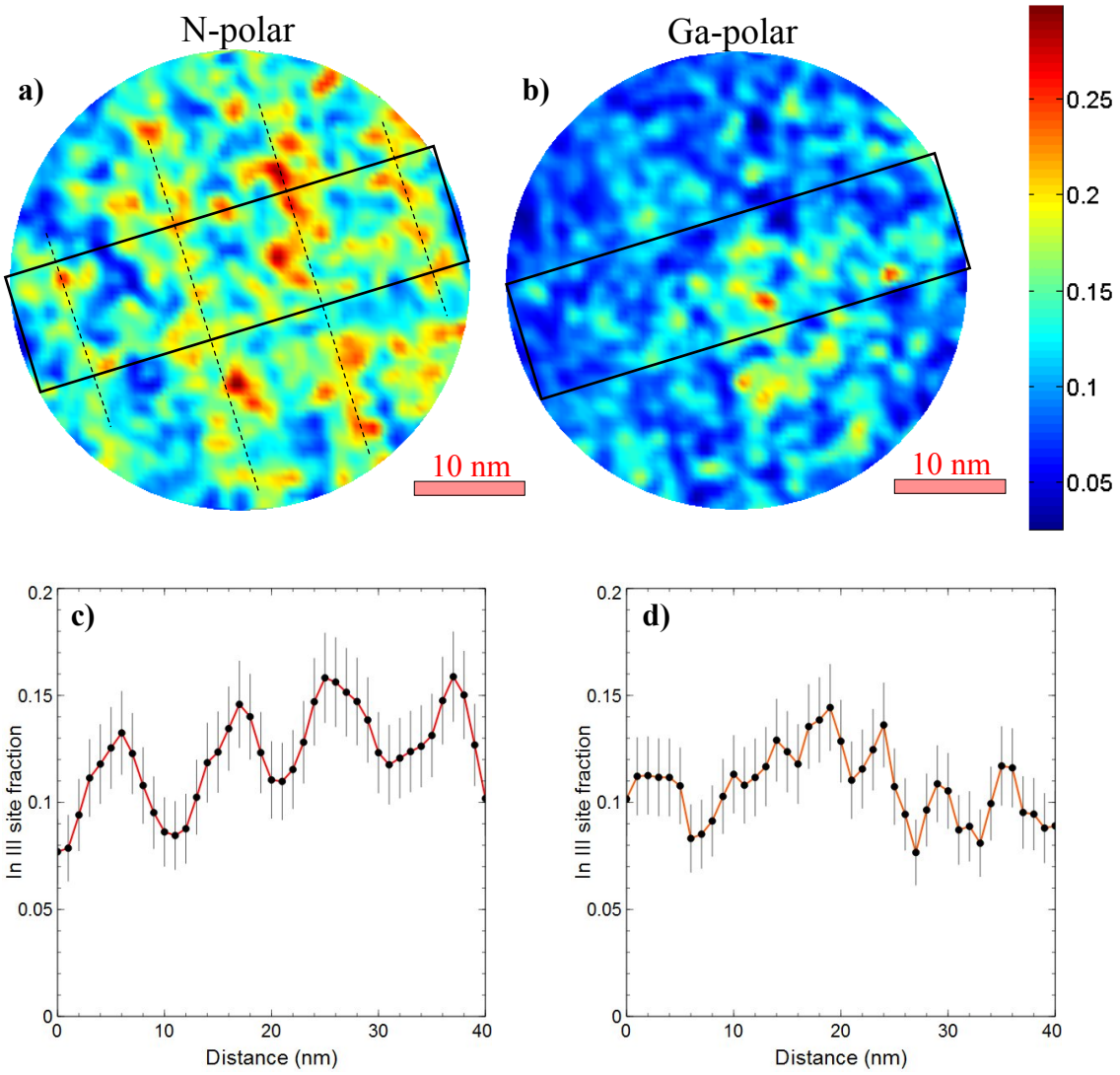

Figure 2.15. a) 2D distribution of In inside the sampling volume "II" in Fig. 2.14a, showing the segregation of In in a stripe-like structure (parallel to the dashed lines). b) 2D distribution of In inside the second Ga-polar well. c) N-polar lateral In fraction profile taken from the sampling volume indicated by the solid box in a). d) Ga-polar lateral In fraction profile taken from the sampling volume indicated by the solid box in b).

resulting in a low growth rate of type *B* steps and eventual step coalescence.[77,78] The increased presence of two monolayer high steps on the N-polar surface further increases the adsorption energy of indium atoms at the step edges, driving the formation of In-rich regions along the steps. It is likely that this is the primary cause of the non-homogeneity in the indium distribution observed in N-polar InGaN layers. Localized In-rich areas are also likely responsible for the increased emission wavelength of the N-polar samples relative to the Ga-polar samples in this chapter, as it is well known that the luminescence from InGaN layers can be dominated by In-rich regions where the bandgap is locally reduced and carrier confinement is increased.[79] These observations provide a way to rationalize the XRD and PL results, where the emission wavelengths of the N-polar samples were significantly higher despite containing similar or slightly lower average indium compositions and comparable layer thicknesses. Similar results were observed in a recent study on non-polar *m*- and *a*-plane quantum wells, where the *a*-plane wells had stronger compositional fluctuations which resulted in longer wavelength emission compared to the *m*-plane samples while containing the same average amount of indium.[80] The results in this section also help to understand the nature of the emission observed in the previous section of this chapter and in other studies on N-polar LEDs which emit at longer wavelengths than predicted from the average indium content in the well layers.

2.5 Tunnel diode growth and fabrication process

In order to assess the tunneling properties of the N-polar InGaN layers, tunnel diodes were grown and fabricated using the epitaxial structure in Figure 2.16. While highly doped n- and p-layers are necessary for band alignment near the junction, in thick layers very high doping can result in poor morphology so only 10 nm of n^+ and p^+-GaN were grown on either side of the InGaN layer. After the growth of the GaN template described above, a 500 nm thick n-GaN layer was grown at 1200 ºC with [Si]=$3x10^{18}$ cm^{-3} followed by a 10 nm n^+-GaN layer with [Si]=$2x10^{19}$ cm^{-3}. Next, a 3 nm thick InGaN layer was deposited at a temperature of 800 ºC with TEGa=1.4 µmol/min, TMIn=18.6 µmol/min, and NH_3=6 slm resulting in a composition of 0.35. After the well growth, 4 nm of unintentionally doped GaN was grown with N_2 carrier gas using the same growth temperature as the well, followed by a 10 nm thick p^+-GaN layer with [Mg]=$1x10^{20}$ cm^{-3} at a growth temperature of 900 ºC using H_2 carrier gas. Finally, 60 nm p-GaN with [Mg]=$3x10^{19}$ cm^{-3} was deposited and the structure was capped with a 10 nm thick p^+-GaN contact layer with [Mg]=$1x10^{20}$ cm^{-3}. The TEGa and NH_3 flows

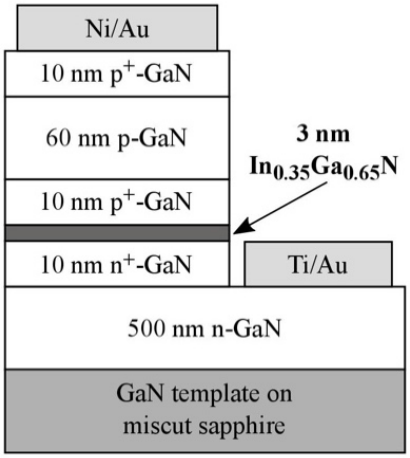

Figure 2.16. Full tunnel diode structure used for electrical characterization.

during p-GaN growth were 4.6 μmol/min and 6 slm, respectively. Capacitance-voltage measurements carried out on similar n-GaN/p-GaN homojunctions showed an average hole concentration in the p-GaN layer of $7x10^{17}$ cm^{-3}. The unintentional carbon and oxygen impurity concentrations in undoped GaN layers grown under the same conditions were around $4x10^{16}$ cm^{-3}.[44] After the growth of the sample Ni/Au (40/100 nm) p-contacts were deposited using electron beam evaporation, device mesas were formed via a Cl_2/BCl_3 reactive ion etch, and Ti/Au (25/250 nm) n-contacts were deposited. Current-voltage curves for 50x50 μm^2 devices were subsequently obtained using a semiconductor parameter analyzer. For further details on the fabrication procedure, refer to Appendix A.

2.6 Tunnel diode electrical performance

In order to achieve high tunneling current in a GaN/InGaN/GaN tunnel diode structure, the thickness and composition of the InGaN layer must be carefully chosen depending on the intended device operation.[45] For a given indium composition there is a critical thickness (t_{cr}) where the band bending due to the polarization dipole is equal to the band gap of InGaN, aligning the conduction and valence bands on either side of the InGaN layer. In order to optimize for tunneling under reverse bias the InGaN thickness should be equal to t_{cr}, resulting in a backward diode, while devices with $t_{InGaN}>t_{cr}$ form an Esaki diode, allowing for high tunneling current under forward bias.[46] For the device shown in Figure 2.16, the thickness of the $In_{0.35}Ga_{0.65}N$ tunneling layer was chosen to be equal to t_{cr} to achieve high tunneling current under reverse bias.

A comparison of the J-V characteristics between the GaN/$In_{0.35}Ga_{0.65}$N/GaN tunnel diode and a GaN p-n junction with the same doping but without an InGaN tunneling layer is

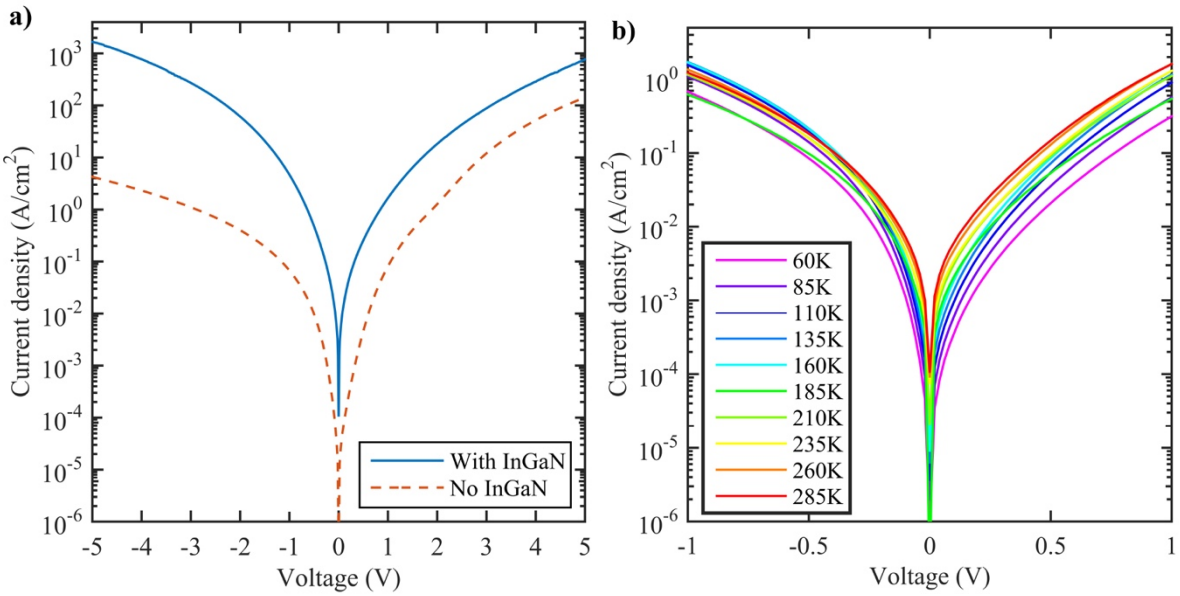

Figure 2.17. a) J-V measurement comparing two tunnel diodes with (blue curve) and without an InGaN tunneling layer (red curve), and b) temperature-dependent J-V measurements of a tunnel diode with the structure shown in Fig. 2.16.

displayed in Figure 2.17a. While the forward bias current of the sample with the InGaN tunneling layer is less than 10x higher compared to the homojunction sample at 5 V, the sample with the InGaN tunneling layer showed 400x higher current density under reverse bias (-5 V) where tunneling is the dominant conduction mechanism. For the sample containing the InGaN tunneling layer a maximum current density of 1.7 kA/cm^2 was achieved at 5 V reverse bias, comparable to previous demonstrations of InGaN/GaN tunnel junctions grown by MBE.[45,48] In contrast, for the sample with no InGaN layer the reverse current was over two orders of magnitude lower, as the distance which carriers had to tunnel through was significantly greater due to the increased depletion width of the p-n junction. Note that the reverse current was still higher than in typical p-n diodes due to the high doping in the n+ and p+ regions of the diode.[81]

The results of temperature-dependent J-V measurements for the structure containing the 3 nm thick $In_{0.35}Ga_{0.65}N$ tunneling layer are shown in Figure 2.17b. The forward bias current in a p-n junction primarily arises from thermionic emission of carriers over the barrier and exhibited an exponential dependence on temperature. In contrast, the current under reverse bias (where Zener tunneling occurs) showed significantly less variation with temperature. While a weak temperature dependence is expected for band to band tunneling processes, defect assisted tunneling may also contribute to the measured current. Additionally, some of the variation with temperature under reverse bias is due to non-ohmic p-contacts which demonstrated thermionic emission characteristics by temperature-dependent p-TLM measurements (not shown). In order to avoid thermal degradation of the high In composition tunneling layers, the p-GaN:Mg layers were grown at 900 ˚C, a temperature significantly lower than in previous studies.[82] Experiments to further optimize the growth and processing parameters of the p-layers for these devices are currently underway.

2.7 Conclusions

High quality N-polar InGaN films were grown using MOCVD, and their structural and tunneling properties have been presented herein. QWs containing up to 46% indium were achieved by tuning the growth temperature and gas flows for both the well and barrier layers, while STEM/EDX experiments showed high structural quality and confirmed the compositions locally within the well layers. APT measurements of N-polar and Ga-polar MQW samples revealed stronger lateral composition fluctuations in N-polar InGaN layers, rationalizing the long emission wavelengths up to 600 nm observed for samples containing less than 25% average indium content in the well layers. Finally, temperature-dependent J-V

measurements conducted on GaN/InGaN/GaN tunnel diode structures suggest tunneling under reverse bias. The presented results outline a growth window for growing high indium composition layers in the N-polar orientation, which is of interest particularly for polarization-engineered device designs including tunnel diodes and transistors.

III. N-polar InN Growth for Electronic Applications

With a bandgap of 0.7 eV, InN has the lowest effective mass,[83] highest electron mobility (14,000 cm^2/Vs, calculated),[84] and highest saturation velocity of the group III nitride alloy system. Furthermore, the robustness and resistance to radiation[85] that is typical of nitride materials combined with a high absorption coefficient makes InN attractive for use in solar cells.[86] However, the growth of high quality InN layers using metal-organic chemical vapor deposition (MOCVD) is complicated due to the material properties of InN. First, the optimum growth temperature of InN is significantly lower compared to GaN and must be kept well below 700 ºC to avoid InN decomposition, which begins already at temperatures around 450 ºC. Low growth temperatures result in a low cracking efficiency of the typical MOCVD N-precursor (NH_3) and lower adatom surface mobilities, increasing the probability of defect formation. In addition, the likelihood of unintentional incorporation of C and O atoms increases,[44] where C is a constituent of the metal organic precursor molecules and O can be present as an impurity in the precursors or process gasses. Many groups have addressed these issues by growing InN layers using plasma-assisted MBE since the active N species are more easily produced at low temperatures using a plasma and C incorporation is negligible when using pure metal sources compared to using carbon-containing precursors in MOCVD. Due to the above limitations, MOCVD-grown InN layers often cannot match the film properties of those deposited by MBE. Thus, electron mobility values as high as 3570 cm^2/Vs have been measured for 2.7 μm thick InN films grown by MBE[87] while the highest value reported for MOCVD-grown layers amounted to 1400 cm^2/Vs (layer thickness 0.8 μm).[88] Post growth thermal annealing of MOCVD-grown films led to an increase in the measured electron

mobilities and reduction in free carrier density due to removal of H atoms which are incorporated during growth and act as donors in InN.[89–91] While the electron mobilities increased, the values were however still lower than those of the MBE-grown films discussed above.

In addition to the growth of bulk-like InN films, efforts have been directed towards the deposition of GaN/InN/GaN heterostructures, which are not only of interest for long wavelength optical devices but also for implementation in tunnel junctions and other electronic devices.[92] The majority of experiments were again performed using MBE for the fabrication of single InN quantum wells (QWs) as well as MQWs. Due to the large lattice mismatch of 10% between InN and GaN, the reported QW thicknesses ranged between one and two monolayers.[17,93–95] More recent investigations have suggested that the nominal InN QWs are instead composed of $In_{0.33}Ga_{0.67}N$,[18] caused by a strain induced $\sqrt{3} \times \sqrt{3}$ surface reconstruction.[96,97] These investigations, however, were all performed on metal-polar heterostructures.

While the growth of bulk InN films of both In- and N-polarity has been reported by both MBE[98–101] and MOCVD,[91,102–105] less is known about the growth of N-polar InN/GaN heterostructures and InN QWs by MOCVD. The reverse direction of the internal electric field in $(000\bar{1})$ N-polar compared to (0001) metal-polar heterostructures[26] is of interest for application in tunnel devices[5,106] and transistors,[28–30] in addition to solar cells,[39] photodetectors,[37,38] and other optoelectronic devices.[32–36] Excellent results were recently reported in particular for N-polar (Al,Ga)N/GaN transistors.[31,107]

In this study, InN layers with thicknesses of 0.5-60 nm were deposited on GaN layers misoriented 4º towards the GaN *m*-direction in order to observe the structural evolution and electrical properties of the InN/GaN heterostructures. The use of vicinal substrates was previously shown to promote the growth of smooth and high quality N-polar (Al,Ga,In)N films by MOCVD.[40,41]

3.1 Growth and characterization of InN/GaN heterostructures

All samples were again deposited in an atmospheric pressure two-flow reactor using TMIn and NH_3 as precursors. In the first set of experiments the dependence of the InN growth rate on the deposition temperature between 450-700 ºC and the NH_3 flow between 1.2 and 9.0 slm was evaluated by growing InN layers directly on (111) Si substrates with a TMIn flow of 4.7 µmol/min for 400 seconds, resulting in 10-60 nm thick layers.

For all other samples, the substrates used were sapphire misoriented 4º towards the *a*-direction, resulting in a 4º misorientation towards the GaN *m*-direction.[40] After loading the substrates into the reactor, 1-2 µm thick semi-insulating GaN base layers were deposited at 1200 ºC using the process described elsewhere.[40,41] After GaN base layer deposition, the carrier gas was switched from hydrogen to nitrogen and the growth temperature was lowered to 550-640 ºC. The 0.5 to 60 nm thick InN layers were then deposited using trimethyl indium (0.21-0.79 µmol/min) and NH_3 (3.2 slm) as precursors. For each temperature, the TMIn flow rate was adjusted to achieve the desired InN growth rate.

Table 3.1. Growth parameters for single heterostructure InN/GaN samples.

	Temp. (ºC)	d(InN) (nm)	R_g (Å/s)
A1	640	1-40	0.22
A2	610	10-60	0.06
A3	550	10-60	0.11
B	580-640	20	0.22
C	610	20	0.06-0.22

Table 3.2. Growth parameters for double heterostructure InN/GaN samples.

	d(InN) (nm)	d(GaN) (nm)	Periods
D	1-20	4	1
E	0.5-1.0	3	3

For the single InN/GaN heterostructure samples in series A1-A3, the thickness of the InN layer was varied between 1 and 60 nm at three sets of temperatures and growth rates as detailed in Table 3.1. Series B consisted of 20 nm thick InN layers deposited with a growth rate of 0.22 Å/s at temperatures between 580-640 ºC. For series C, 20 nm thick InN layers were grown at 610 ºC with growth rates between 0.06-0.22 Å/s. The growth parameters for all single heterostructure samples are summarized in Table 3.1.

In addition, two sets of GaN/InN/GaN double heterostructure samples were deposited at 640 ºC with an InN growth rate of 0.22 Å/s. In series D, single quantum well structures were grown with 1-20 nm thick InN layers and 4 nm thick GaN barriers. Series E consisted of triple quantum well structures with 0.5-1.0 nm thick InN layers and 3 nm thick GaN barrier layers. For series D and E, the GaN barriers were deposited at the same temperature as the InN layers using a flow modulation epitaxy (FME) scheme wherein the NH_3 flow was kept constant at a flow of 3.2 slm while TEGa was pulsed with a flow rate of 1.1 µmol/min, resulting in ~1 ML GaN growth per 10-second-long cycle followed by a 10 sec pause. The structures for all double heterostructure samples are summarized in Table 3.2.

The thickness of the InN layers grown on Si was determined using a Woolam M2000DI Variable Angle Spectroscopic Ellipsometer in order to extract the growth rate at each temperature. The surface morphology of the samples was assessed using an Asylum MFP3D atomic force microscope (AFM). X-ray diffraction (XRD) was used to measure ω-2θ scans around the GaN (0002) reflection and reciprocal space maps (RSMs) were taken around the GaN $(11\bar{2}4)$ reflection using a PIXCEL 1-D line detector in order to measure the strain state of the InN layers. X-ray photoelectron spectroscopy (XPS) was used to determine atomic compositions of selected samples by calculating the ratio of the signal from the In 4s electrons with a binding energy of 123 eV and the Ga 3p electrons with a binding energy of 104 eV. To electrically characterize the samples, room temperature Hall effect measurements were collected using the van der Pauw technique with indium contacts. Cross-sectional TEM samples were prepared in a FEI Nova 200 dual-beam FIB/SEM by using the lift-out method. The TEM lamellas were prepared by cutting sections of the samples perpendicular to the $[11\bar{2}0]$ direction so that the observation direction was perpendicular to the steps that arose from the crystal misorientation. The atomic STEM-HAADF images were obtained in a JEOL ARM200F microscope equipped with a spherical aberration (Cs) corrector (CEOS GmbH, Heidelberg, Germany) and operated at 200 kV. The corrector was carefully tuned by the Zemlin-tableau method with Cs = 0.5 μm and the resolution was demonstrated to be around 1 Å.

3.2 Single heterostructure results

Figure 3.1 illustrates the dependence of the InN growth rate on deposition temperature and NH_3 flow for the InN films directly deposited on (111) Si. As reported previously, for low growth temperatures the growth rate was limited due to inefficient pyrolysis of precursor molecules while at high temperatures the InN layer decomposed, resulting in a metallic In surface layer with little InN growth. In the intermediate temperature range from around 620-675 ºC, the growth rate reached a maximum and was relatively stable with respect to temperature.[92] The growth rate was largely independent of the NH_3 flow (Fig. 3.1b), indicating minimal pre-decomposition of NH_3 in the gas phase.[59] The structural evolution of series A1 consisting of uncapped InN films with nominal thicknesses from 1-20 nm deposited at 640 ºC is shown in Figure 3.2a-3.2f presenting the AFM images of the samples. After the deposition of nominally 1 nm InN, quantum dot-like features formed with heights of 5-10 nm and diameters of 20-50 nm (Fig. 3.2a). The dot-like features were aligned along the steps on the

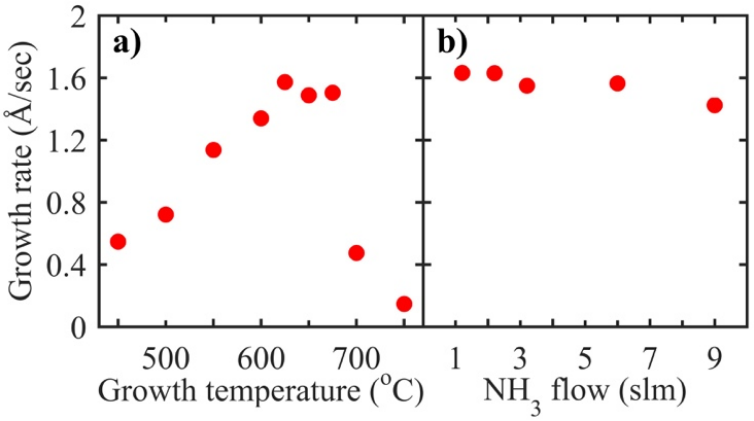

Figure 3.1. InN growth rate dependence on a) growth temperature with an NH_3 flow of 3.2 slm and b) NH_3 flow at a growth temperature of 640 ºC.

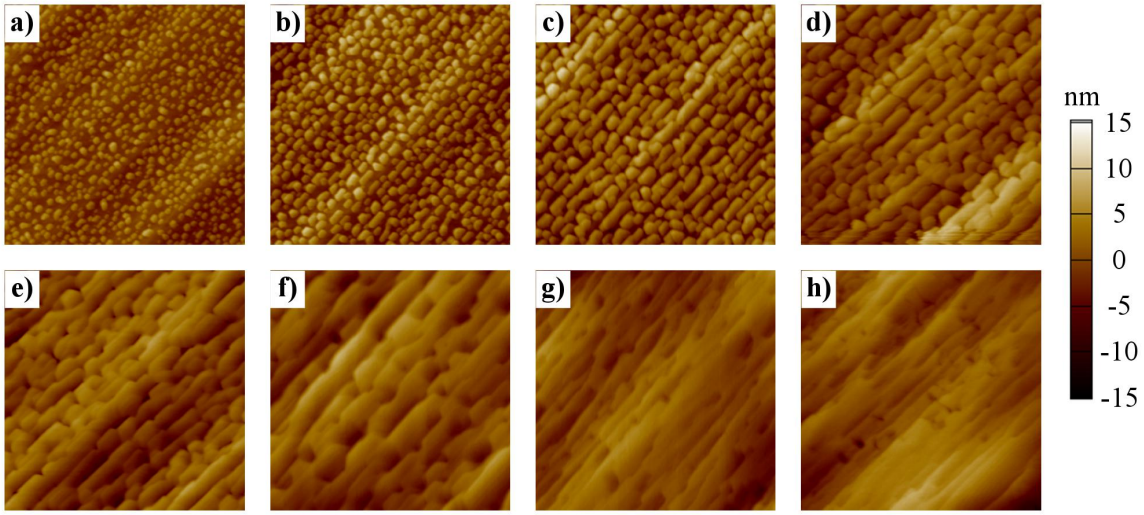

Figure 3.2. 1.5x1.5 μm^2 AFM height images of InN layers deposited on GaN at 640 ºC (series A1) with nominal thicknesses of a) 1 nm (RMS=1.2 nm), b) 2 nm (RMS=1.6 nm), c) 3 nm (RMS=2.1 nm), d) 5 nm (RMS=2.9 nm), e) 10 nm (RMS=2.6 nm), and f) 20 nm (RMS=2.5 nm), as well as images of 20 nm thick InN layers (series B) deposited at g) 610 ºC (RMS=2.5 nm) and h) 580 ºC (RMS=3.4 nm). The given height scale applies to all images besides a-c, where the height range is -7.5 to 7.5 nm.

vicinal GaN surface. As the deposition continued, the dots elongated along the step direction before coalescing and growing outward to form a closed film after the deposition of nominally 5-10 nm InN. To determine the extent of relaxation in the InN layers, XRD RSMs were recorded around the GaN $(11\bar{2}4)$ reflection for the series of uncapped InN films with nominal thicknesses from 1-20 nm. For all samples, the InN peak position corresponded to *a* and *c* lattice parameters around 10% larger than the GaN base layers (Table 3.3). The RSMs for the nominally 20 nm and 1 nm thick InN films are shown in Fig. 3.3a and 3.3b, respectively. These results indicated that the InN fully relaxed at the onset of dot formation,[108–110] even for the film with 1 nm nominal thickness that was comprised of 5-10 nm high quantum dot-like features with diameters of 20-50 nm shown in Fig. 3.2a. The peak on the left side adjacent to

Table 3.3. InN/GaN lattice mismatch for various nominal InN thicknesses (series A1) according to XRD reciprocal space maps.

d(InN) (nm)	Parallel mismatch (%)	Perpendicular mismatch (%)
20	10.0	10.5
10	9.9	10.6
5	10.2	10.5
3	10.0	10.5
2	10.1	10.5
1	9.9	10.2

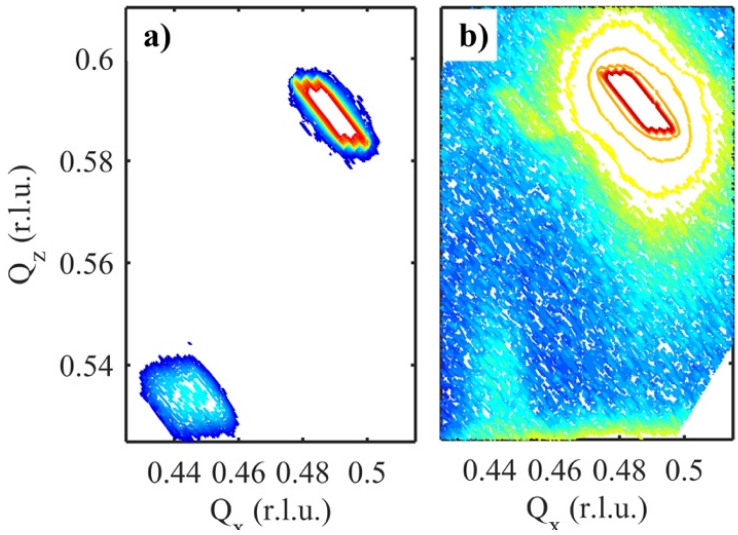

Figure 3.3. XRD RSMs around the GaN $(11\bar{2}4)$ reflection for a) a 20 nm thick continuous InN layer and b) a nominally 1 nm thick InN layer comprised of quantum dots (series A1).

the GaN peak in the RSM in Fig. 3.3b was attributed to an artifact from the XRD measurement and was accompanied by a similar peak to the right of the GaN peak. Additionally, the asymmetric GaN peak shape is attributed to the use of the 1-D array detector and is exaggerated by the intensity scaling which was chosen to highlight the InN peaks.

Figures 3.2f-3.2h illustrate the effect of the InN growth temperature on the terrace structure for 20 nm thick layers grown between 640 and 580 ºC (series B). As the growth

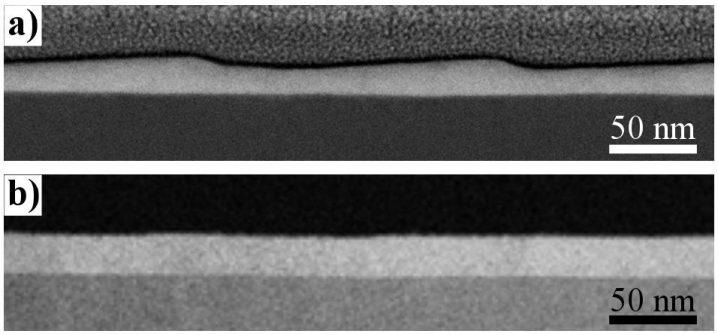

Figure 3.4. HAADF STEM images of 20 nm thick InN/GaN single heterostructures (series B) deposited at a) 640 ºC and b) 580 ºC.

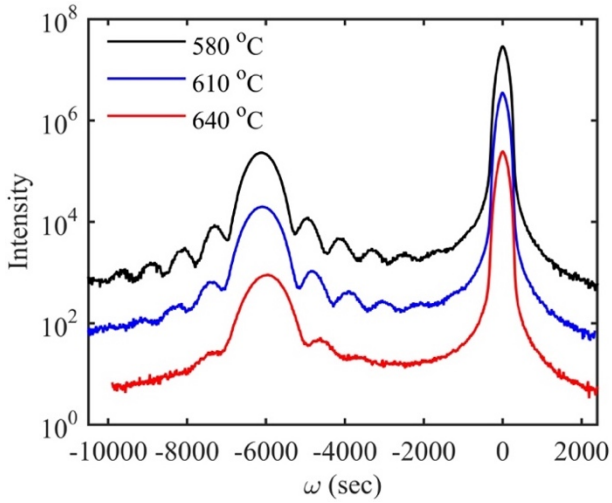

Figure 3.5. XRD ω-2θ scans around the GaN (0002) reflection for 20 nm thick InN layers (series B) grown at 580 ºC (top scan), 610 ºC (middle), and 640 ºC (bottom).

temperature was decreased, the terraces elongated along the direction parallel to the surface steps and the macrostep height was reduced. For the 20 nm thick layers grown at 640 and 580 ºC, the STEM images are shown in Figure 3.4. The surface of the sample grown at 640 ºC displays macrosteps around 3 nm in height with terrace lengths of around 100 nm, resulting in a layer thickness ranging from 16-19 nm. The terrace lengths were very uniform across the sample, as can be seen in the complimentary AFM image in Fig. 3.2f. For the sample grown at 580 ºC, the layer thickness was much more uniform and there were no steps visible on the

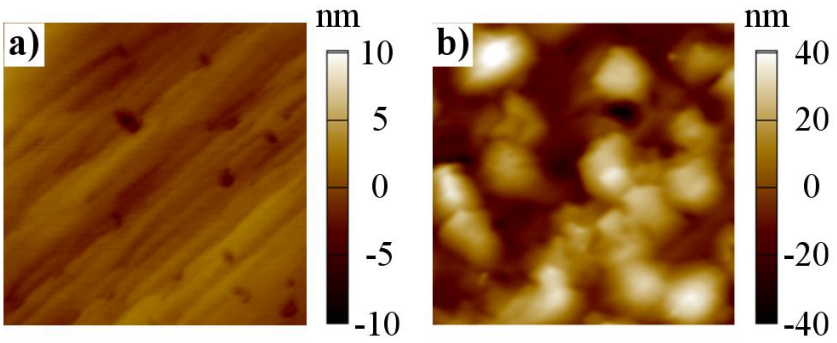

Figure 3.6. AFM height images of 60 nm thick InN layers grown at a) 550 ºC with at growth rate of 0.11 Å/s (1.5x1.5 μm^2, RMS=1.4 nm, series A3), and b) 610 ºC with at growth rate of 0.06 Å/s (5x5 μm^2, RMS=15 nm, series A2).

sample surface in the TEM image in Fig. 3.4b. Figure 3.5 shows the XRD ω-2θ scans around the GaN (0002) reflection for the 20 nm thick uncapped InN layers grown at temperatures between 640 and 580 ºC in series B. The lowest growth temperature resulted in the highest number of fringe peaks due to its more uniform terrace structure and layer thickness as seen in Fig. 3.4.

In addition to XRD measurements, the composition of the 20 nm thick layers grown at 580 and 640 ºC was verified using XPS. The sample grown at 580 ºC contained around 1.0% Ga, while the sample grown at 640 ºC contained around 1.4% Ga. Furthermore, the Ga peak contribution increased significantly as the photoelectron takeoff angle was changed from 0 to 60 degrees relative to the sample normal, indicating that the Ga atoms accumulated on the surface rather than incorporating into the InN layers (not shown).

Figure 3.6 shows the AFM images of 60 nm thick layers grown at 550 ºC with a growth rate of 0.11 Å/s (series A3) and at 610 ºC with a growth rate of 0.06 Å/s (series A2). The layer grown at 550 ºC displayed a smooth surface with a regular step structure similar to the

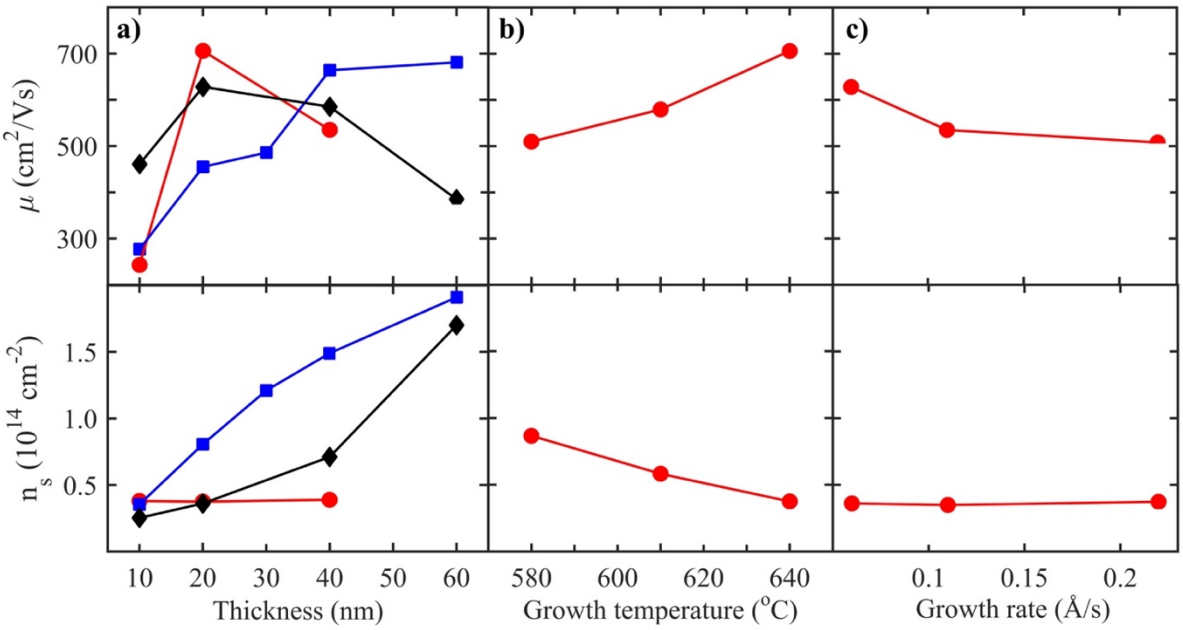

Figure 3.7. Electron mobility (top) and sheet carrier density (bottom) dependence on a) InN thickness for samples grown at 640 ºC with a growth rate of 0.22 Å/s (red circles, series A1), 610 ºC with a growth rate of 0.06 Å/s (black diamonds, series A2), and 550 ºC with a growth rate of 0.11 Å/s (blue squares, series A3), b) growth temperature for 20 nm thick samples deposited with a growth rate of 0.22 Å/s (series B), and c) growth rate for 20 nm thick samples grown at 610 ºC (series C).

observations for thinner layers, while the surface morphology of the sample grown at 610 ºC deteriorated and was decorated with large islands.

The results of the Hall effect measurements for series A1-A3 with different InN thicknesses are shown in Figure 3.7a. For series A1 grown at 640 ºC with a growth rate of 0.22 Å/s, the sheet charge density remained constant at around 4 x 10^{13} cm^{-2} for 10-40 nm thick layers. The electron mobility reached a maximum of 706 cm^2/Vs for an InN thickness of 20 nm then decreased to 535 cm^2/Vs as the thickness was increased to 40 nm. For series A2 grown at a temperature of 610 ºC with a growth rate of 0.06 Å/s, the sheet charge increased slightly from 2.5 x 10^{13} cm^{-2} to 3.6 x 10^{13} cm^{-2} as the InN thickness was increased from 10 to 20 nm, then further increased to 7.1 x 10^{13} cm^{-2} for the 40 nm thick layer. When the layer

thickness was increased to 60 nm, the measured sheet charge rose significantly to 1.7 x 10^{14} cm^{-2}. Similar to series A1, the mobility reached a maximum for the 20 nm thick InN layer then declined as the thickness was further increased. The maximum mobility of 628 cm^2/Vs, however, was somewhat lower compared to value of 706 cm^2/Vs measured for the 20 nm sample grown at 640 ºC. For series A3 grown at 550 ºC with a growth rate of 0.11 Å/s, the sheet charge steadily increased from 3.5 x 10^{13} cm^{-2} to 1.9 x 10^{14} cm^{-2} as the thickness was increased from 10 to 60 nm, accompanied by a steady increase of the electron mobility from 277 to 664 cm^2/Vs for 10-40 nm thick layers and a slight increase to 681 cm^2/Vs as the thickness was further increased to 60 nm.

Figure 3.7b shows the effect of growth temperature on the electron mobility and the sheet carrier density for 20 nm thick layers grown at 0.22 Å/s (series B). The sheet charge density decreased from 8.7 x 10^{13} cm^{-2} to 3.8 x 10^{13} cm^{-2} as the growth temperature was increased, while the electron mobility increased from 510 to 706 cm^2/Vs with increasing growth temperature. The mobility and carrier density for series C consisting of 20 nm thick InN layers grown at 610 ºC using different growth rates is shown in Figure 3.7c. Regardless of the growth rate, the charge remained constant at 3.5 x 10^{13} cm^{-2}. The electron mobility was around 520 cm^2/Vs for the samples grown with growth rates of 0.22 and 0.11 Å/s, but slightly increased to 628 cm^2/Vs as the growth rate was further reduced to 0.06 Å/s.

3.3 Double heterostructure results

To explore the impact of a GaN capping layer on the InN layer properties,[101] the InN layer thickness series grown at 640 ºC was repeated with the addition of a 4 nm thick GaN cap layer (series D). The AFM images of samples with InN thicknesses from 1 to 5 nm are displayed in Figure 3.8. For InN thicknesses from 1-2 nm shown in Figs. 3.8a-3.8b, the GaN cap resulted in a smoother surface compared to the uncapped samples with the same thickness shown in Figs. 3.2a-3.2b. For the 5 nm InN layer shown in Fig. 8c, the surface after deposition of the GaN cap appeared similar to the uncapped sample shown in Fig. 3.2d besides the presence of small islands which are likely In accumulation on the surface. The cross sectional TEM image of the sample with nominally 5 nm InN and a 4 nm GaN cap layer is displayed in Fig. 3.9a. Due to the step bunching occurring during InN layer deposition, about 100 nm wide InN "wedges" or macrosteps formed again consisting of an on-axis *–c* surface and an inclined *m*-plane sidewall with an angle close to the semi-polar $(20\bar{2}\bar{1})$ plane. Interestingly, the long surface terraces persisted during the deposition of the nominally 4 nm thick GaN cap layer,

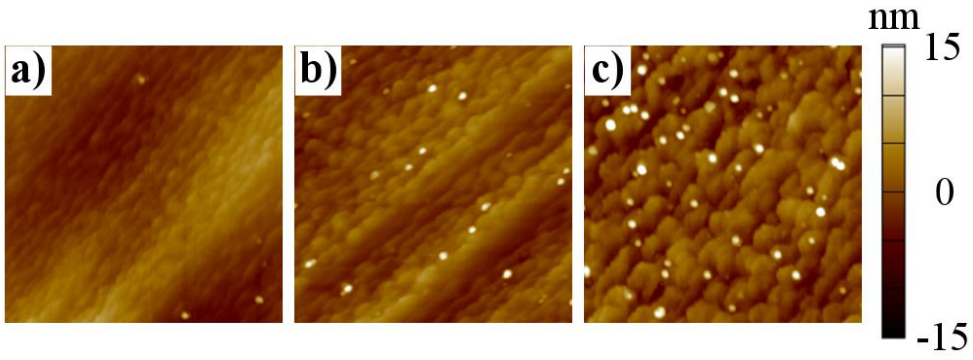

Figure 3.8. 1.5x1.5 μm^2 AFM height scans of double heterostructures (series D) with 4 nm GaN cap thickness and InN thicknesses of a) 1 nm (RMS=2.4 nm), b) 2 nm (RMS=2.2 nm), and c) 5 nm (RMS=2.9 nm).

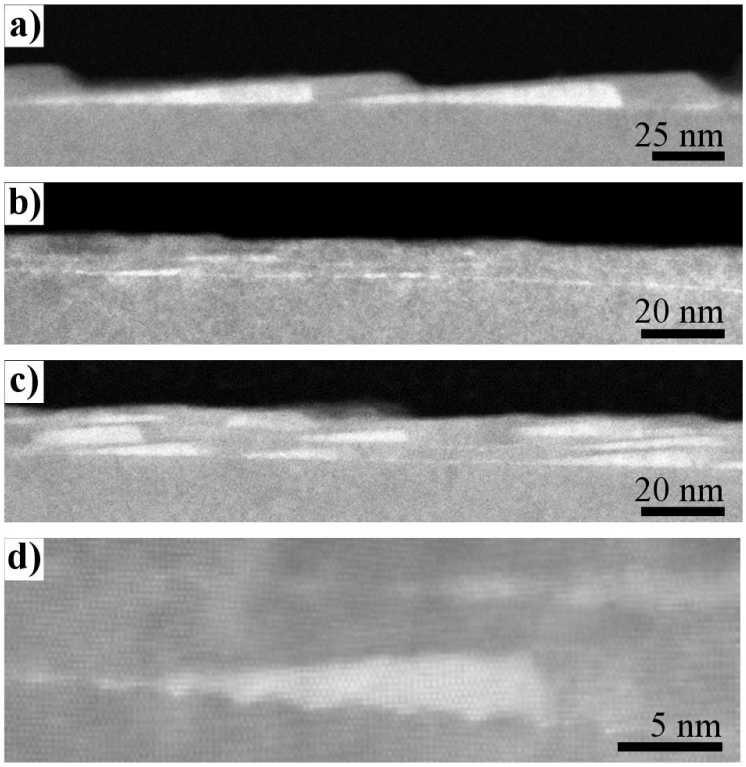

Figure 3.9. HAADF STEM images of a) a SQW structure consisting of nominally 5 nm InN/4 nm GaN from series D, and triple quantum well structures from series E with nominal InN thicknesses of b) 0.50 nm, and c) 1.0 nm, as well as d) a higher magnification image of the 1.0 nm thick MQW sample illustrating the step structure.

which grew with a significantly higher lateral growth rate compared to the growth rate in the –c direction. When coexisting with other surface orientations, the *–c* plane has often been observed to be the slowest growing plane.[111] The sample surfaces of the GaN capped samples with 10 and 20 nm thick InN layers were rough and the layer structure deteriorated during GaN cap layer deposition (not shown).

The cross-sectional STEM images for MQW samples from series E containing InN layers from 0.5-1.0 nm thick are shown in Figs. 3.9b-3.9d. The "well" of the 0.5 nm sample was extremely thin (~ 1 bilayer) with additional thicker islands (2–5 nm in height, Fig. 3.9b). Islands were also visible for the second InN "well" while the third "well" was difficult to

identify. Three layers with larger islands can be seen for the sample with a nominal well thickness of 1 nm (Fig. 3.9c), with island sizes similar to those observed in the AFM image of the uncapped 1 nm thick layer (Fig. 3.2a). The island formation is characterized by step bunching and formation of an extended top terrace. Interestingly, more regular smaller steps formed again during GaN barrier growth before InN islands with long surface terraces were created again during InN deposition (Figs. 3.9c-3.9d).

3.4 Morphological evolution of InN layers

The spontaneous formation of quantum dot-like features and the subsequent structural evolution of the InN layers was most likely driven by the 10% lattice mismatch between InN and GaN. As seen in the recorded RSMs, the formation of the quantum dot-like features allowed for efficient strain relaxation. In addition, the step bunching which occurred might have contributed to the relaxation of the InN lattice constant. Stress-induced step bunching has been observed in a variety of semiconductor systems when grown on vicinal substrates and was associated with strain relief, for example in SiGe layers grown on vicinal Si.[112] This process has been attributed to elastic relaxation at the step edges creating a long range attractive interaction between steps such that the step bunching behavior is driven by the surface energetics rather than the kinetics of step flow growth.[113] Step bunching was clearly visible also for the thicker 20 nm thick InN layer in Figs. 3.2f and 3.4a, where the surface displays macrosteps which run parallel to the steps on the vicinal GaN surface. In addition, as the growth temperature was reduced the macrostep height and terrace length decreased (Figs. 3.2f-3.2h) resulting in the highest number of InN (0002) fringe peaks in XRD ω-2θ scans (Fig.

3.5). Less pronounced step bunching at reduced temperatures was also observed in other material systems.[113–115]

For the MQW samples shown in Figs. 3.9b-3.9d, the macrosteps "dissociated" again during the growth of the conformal GaN barrier layers such that the bottom interface of each InN layer looked similar to the vicinal GaN surface beneath the first InN layer. Despite the smooth GaN surface beneath each InN layer, Fig. 3.9c shows that the InN dots/wires tended to align vertically along the *c*-axis due to local strain variations. Such a stacking of quantum dots and wires is also very well known in other semiconductor systems and driven by the differences in the in-plain lattice constant when comparing the regions above or beside the quantum dot/wire like features. Additionally, it is energetically favorable to form semipolar facets which have lower strain energy compared to the *c*-plane, with a minimum occurring around 60º inclination relative to the *c*-plane.[15] The lower strain on the semipolar facets also locally eases the In incorporation. When growing alloys, this effect is often called compositional pulling, thereby driving the formation of local regions with higher In content.[13,14] Such semipolar facets are visible in the 1.0 nm InN/GaN MQW depicted in Figs. 3.9c-3.9d and the 5 nm thick InN sample which was capped with GaN (Fig. 3.9a). Interestingly, the severe step bunching in the nominal 5 nm thick InN layer resulted in an enhancement of lateral growth of the GaN top layer with very little growth in the *–c* direction. This circumstance was most likely responsible for the degradation of the layer structure when capping thicker InN layers with GaN. In contrast, as discussed above the typical small steps were re-established during GaN layer deposition in case of the nominal 0.5 and 1 nm InN well layers in the MQW samples, where the InN step bunching was less pronounced due to the

reduced thickness and reduced density of the InN dot-like features. While the investigations showed that the InN dot-like features were composed of pure InN, the experimental set up did not allow determination of the composition of the very thin bilayer between the dot like features (Fig. 3.9).

3.5 Electronic properties of InN thin films

The electronic properties of the 5-60 nm thick InN layers, in particular the electron mobility, strongly depended on the InN layer thickness and growth temperature. For the 5 nm layer shown in Fig. 3.2d, the mobility was very low most likely since the layer was not fully coalesced at this point. For thicker layers from 10-20 nm, the mobility increased with thickness. As the electronic properties of these very thin layers were dominated by conduction in the surface accumulation layer,[116] this trend was most likely related to improved layer uniformity and increased distance from the GaN/InN heterojunction. Whether the electron mobility would further increase when the layer thickness was increased to 40 or 60 nm strongly depended on the deposition temperature. While the electron mobility continued to increase for the samples grown at 550 ºC, the electron mobility decreased for the samples grown at 610 ºC and this effect was even more pronounced for the series grown at 640 ºC. Nevertheless, the highest electron mobility of 706 cm^2/Vs among all samples was obtained for the 20 nm thick layer grown at the highest explored growth temperature of 640 ºC. The reduction in electron mobility with increasing thickness at higher growth temperature was associated with a degradation of the surface morphology as seen in Fig. 3.6, and most likely related to the low thermal stability of InN.[1]

The dependence of the measured sheet charge on the InN layer thickness was markedly affected by the growth temperature as well. While the charge was independent of the layer thickness for the InN layers grown at 640 ºC, it increased with increasing thickness when the growth temperature was lowered to 610 ºC, and increased even further at the lowest explored temperature of 550 ºC. Interestingly, for 10 nm thick films the sheet charge was unaffected by the growth temperature, indicating that the measured charge was dominated by the InN/GaN interface charge[117,118] and electron accumulation at the sample surface which is characteristic of InN layers due to surface band bending.[116,119–121] The measured sheet charge of 2.5 to 3.8 x 10^{13} cm^{-3} compared well to previously reported values.[100,116,122] For the samples grown at 640 ºC, the bulk InN carrier density was obviously too low to contribute to the overall charge. At a lower growth temperature of 610 ºC, the sheet charge increased when the layer thickness was increased to 40 nm, and increased even more significantly for a thickness of 60 nm. From the increase in sheet charge from 20 to 40 nm, a bulk carrier concentration of 1.8 x 10^{19} cm^{-3} can be extracted, 3.3 x 10^{19} cm^{-3} using the sheet charge value measured for the 60 nm thick layer. At the lowest investigated growth temperature of 550 ºC, the increase in sheet charge with layer thickness was even more pronounced. While the slope was not exactly linear, from the sheet charge value measured for the 40 nm thick layer a bulk carrier concentration of 3.4 x 10^{19} cm^{-3} can be derived. The increase in bulk carrier concentration with decreasing growth temperature was most likely related to an increase in the oxygen impurity incorporation, as oxide incorporation is well known to increase with decreasing deposition temperatures.[44] In InN oxygen forms a shallow donor just like in GaN.[123] In addition, more N-vacancies could form at lower temperatures due to the lower NH_3 decomposition efficiency at reduced

temperatures.[10] Due to enhanced scattering, the higher electron concentrations were accompanied by a reduction in electron mobility from 706 to 510 cm^2/Vs (Fig. 3.7b). The maximum mobility value in this study of 706 cm^2/Vs was higher than most reports for layers of this thickness grown by either MBE or MOCVD which were around 300-400 cm^2/Vs.[91,100,116] This value, however, compares well with the electron mobility extracted for the surface accumulation layer for 1 μm and 2 μm thick N-polar InN layers grown by MBE,[122] where a higher mobility of the surface electrons in N-polar compared to In-polar samples was noted as well. While the electron mobility increased with decreasing growth rate, the effect was moderate and most likely related to a slightly higher measured layer thickness (23 nm) for the layer with the lowest growth rate as extracted from XRD ω-2θ fringe peak spacing. The sheet carrier density was unaffected by the growth rate most likely due to the generally very large V/III ratio during growth.

3.6 Conclusions

In summary, InN films between 0.5-60 nm were deposited on GaN base layers using MOCVD at temperatures from 550-640 ºC. After the deposition of a nominally 0.5 nm thick layer, the InN relaxed by forming quantum dot-like features which were aligned with the surface steps on the vicinal GaN. The surface steps drove the growth process, eventually resulting in thicker layers with large macrosteps and terraces when deposited at higher temperatures. While smoother surfaces were achieved at low growth temperatures, the best electrical performance was obtained at the highest growth temperature of 640 ºC, resulting in a maximum measured electron mobility of 706 cm^2/Vs for a 20 nm thick InN layer. While the sheet carrier density of 10 nm thick layers was independent of the specific growth conditions

and remained constant for thicker InN films deposited at 640 ºC, the sheet charge increased with layer thickness at lower growth temperatures due to an increase in the bulk carrier concentration. Additionally, 0.5-5 nm thick InN layers were capped with GaN barriers to form SQW and MQW heterostructures.

IV. Patterned Ga-polar Substrates for 1-D Relaxation

The fabrication of (In,Ga)N based devices with high In content in the active region would greatly benefit from reducing the lattice mismatch between the active region and adjacent layers, by replacing GaN with InGaN as the base material.[124–126] While several attempts to fabricate relaxed bulk InGaN layers have been made using hydride vapor phase epitaxy (HVPE), MOCVD,[127,128] and also molecular beam epitaxy (MBE),[129–131] no InGaN substrates are currently commercially available. Note that thin high quality p-$In_xGa_{1-x}N$ films with $x < 0.2$ have been demonstrated by MOCVD on GaN in the past.[132] Thicker and/or higher In composition MOCVD-grown InGaN films, however, exhibit poor structural properties, due to their relaxation via V-defect formation.[11,133,134] Improved properties have also been observed from MQWs on top of locally relaxed regions of InGaN grown on GaN stripes with triangular cross sections.[135,136]

In this chapter, we explore the possibility of utilizing the elastic relaxation in (In,Ga)N nanostructures for the fabrication of relaxed planar (In,Ga)N films. Previously, nanopillars composed of (In,Ga)N/GaN MQW stacks, which were fabricated through patterning of coherently strained planar MQW samples, were observed to relax after pattern formation, adopting an *a*-lattice constant corresponding to the average indium composition in the MQW stack.[137–139] Similarly, in (In,Ga)N MQW nanostripe arrays, relaxation was observed perpendicular to the stripe direction (the MQW stacks maintained their coherence with the GaN base layer parallel to the stripes).[137,138] Similar observations have been made in other material systems.[140,141]

Here, we investigated the growth and properties of planar $In_xGa_{1-x}N$ layers fabricated via coalescence of (In,Ga)N nanostripe arrays, with emphasis on the impact of the nanostripe geometry on the relaxation behavior and properties of the coalesced planar $In_xGa_{1-x}N$ top layers. Providing a height to width aspect ratio of about 1 or higher was essential for preventing defect formation and achieving planar $In_xGa_{1-x}N$ layers with $a_{\perp}(In_xGa_{1-x}N) > a_{\perp}(GaN)$ perpendicular to the stripes, leading to strong light emission.

4.1 Growth and fabrication of nanostripe arrays

All samples in this chapter were grown by MOCVD using the precursors TMGa (trimethylgallium), TEGa (triethylgallium), TMIn (trimethylindium) and NH_3 on sapphire substrates.

Nanostripe arrays with 100 nm stripe height and 180 nm width, resulting in an aspect ratio, A, of about 0.5 were fabricated from 7 period (5 nm $In_{0.2}Ga_{0.8}N$/6 nm GaN) MQW samples. Arrays with 200 nm high and 180–200 nm wide stripes (A~1) were processed from 23 period (1.9 nm $In_{0.25}Ga_{0.75}N$/6.8 nm GaN) MQW samples. All samples with A~0.5 were grown and processed as part of previous studies,[137,138] while samples with A~1 were grown and fabricated in this work. The planar MQW stacks were grown following the procedures described in reference [137] and [142], respectively. MQW stacks instead of InGaN bulk layers were chosen because the MQW stacks could be grown thicker with fewer defects compared to bulk InGaN layers. Slight variations between samples resulted from non-uniformities over the as-grown MQW wafers.

For the nanostripe arrays, a layout with a narrow spacing of 20 to 40 nm between the individual stripes was chosen to aid the coalescence process. The stripe direction was parallel

to $\langle 1\bar{1}00 \rangle$. SiO_2 and Si_3N_4 mask layers were first deposited via plasma-enhanced chemical vapor deposition (PECVD) onto the planar MQW samples, and then an anti-reflective coating and photoresist were spun on. Using holographic lithography, a stripe pattern was defined with a pitch of 200 nm. After development, a series of dry etches was performed in order to transfer the stripe pattern onto the SiO_2 and Si_3N_4 mask layers. An HF undercut etch was used to define the fill factor of the stripe pattern, and then a nickel hard mask was deposited to protect the GaN surface where the stripes would be. After removal of the SiO_2 and Si_3N_4 masks, a final dry etch was performed to etch the stripe pattern into the InGaN/GaN MQWs and the nickel mask was removed (Figure 4.1).

The patterned samples were re-loaded into the MOCVD chamber, and 7 to 40 nm thick GaN layers and 100 to 250 nm thick $In_xGa_{1-x}N$ layers were deposited on top of the stripe arrays at temperatures between 800 and 980 °C under similar conditions to those used during

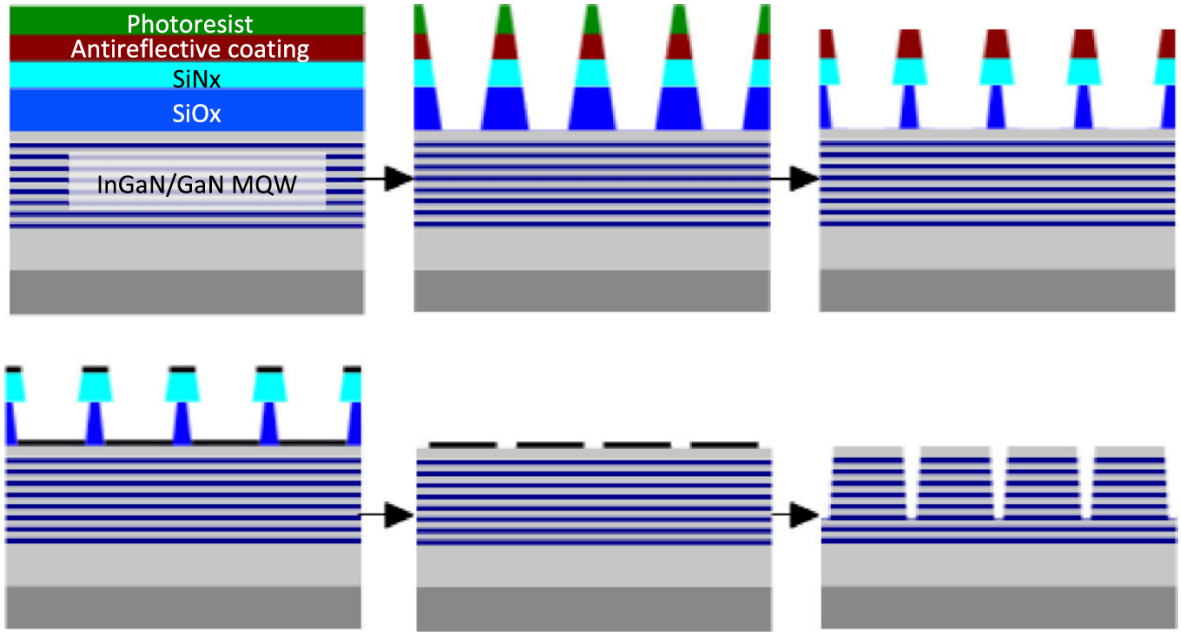

Figure 4.1. Schematic process flow for nanostripe array fabrication.

well and barrier growth of the planar MQW samples. In selected experiments the growth process was stopped after GaN coalescence layer deposition to facilitate monitoring of the optical properties of the MQW stripe arrays after regrowth.

Room temperature (RT) photoluminescence (PL) spectra were recorded using the 325 nm line of a He–Cd laser with an excitation density of 220 W cm^{-2}. The structural properties of the samples in the various process stages were monitored by high resolution x-ray diffraction (XRD). To investigate the properties perpendicular to the stripe direction, reciprocal space maps (RSMs) were recorded around the asymmetric $(11\bar{2}4)$ reflection with the x-ray scattering plane perpendicular to the stripes. RSMs were also taken around the asymmetric $(10\bar{1}5)$ reflection with the x-ray scattering plane parallel to the stripes. Field emission scanning electron microscopy (SEM) was carried out using a JEOL 7600F, and combined cathodoluminescence (CL) and SEM were performed using an FEI Inspect S. Selected samples were also evaluated by transmission electron microscopy (TEM) using an FEI T20. The sample surface was characterized by atomic force microscopy using an Asylum MFP3D.

4.2 Relaxation behavior of stripe arrays

4.2.1 Stripe arrays with an aspect ratio of 0.5

Figures 4.2a-4.2b depict the SEM cross section and top view, respectively, of a 7 period MQW sample after processing. The pits on the sample surface were already present on the planar MQW sample and correspond to the typical V-defects observed for MOCVD (In,Ga)N films. The $(11\bar{2}4)$ RSM of the MQW sample after stripe array processing (Figure 4.3a) showed that all superlattice peaks were shifted towards the left side of the GaN base layer

peak, as the MQW stack adopted an in-plane lattice constant perpendicular to the stripe direction, $a_{\perp}$, larger than that of the GaN base layer. The low intensity signal at the Q_x value of GaN originated most likely from the unpatterned area at the sample edge. Note that the MQW stack was still coherent with the GaN base layer parallel to the stripes (not shown), as observed previously.[137]

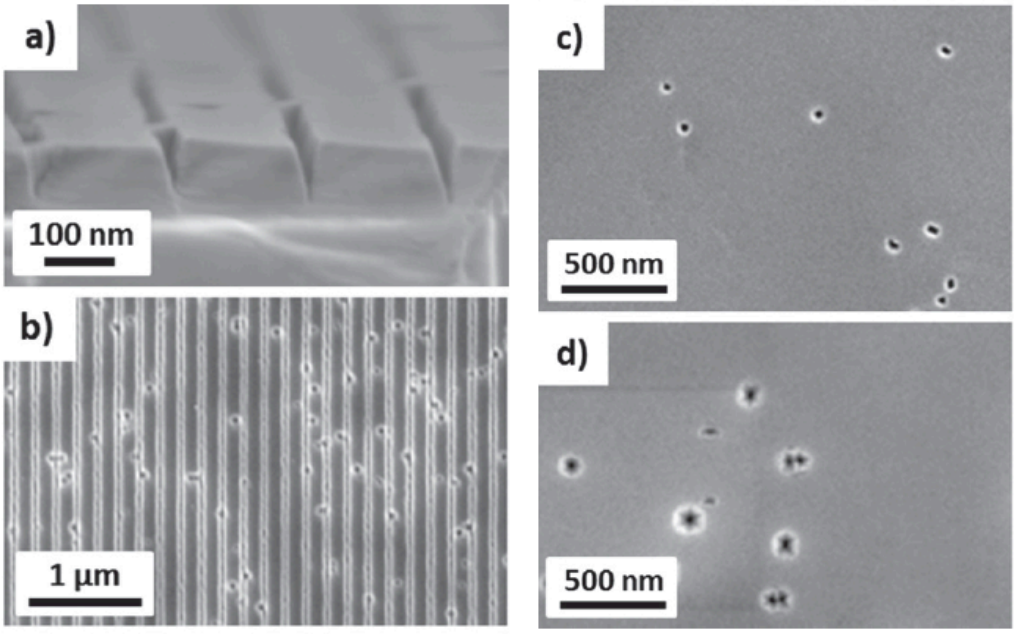

Figure 4.2. Scanning electron microscopy images of (a) cross section and (b) top view of patterned 7 period (5 nm $In_{0.2}Ga_{0.8}N$/6 nm GaN) MQW sample; sample surface after deposition of (c) 7 nm GaN and (d) additional 100 nm $In_{0.1}Ga_{0.9}N$.

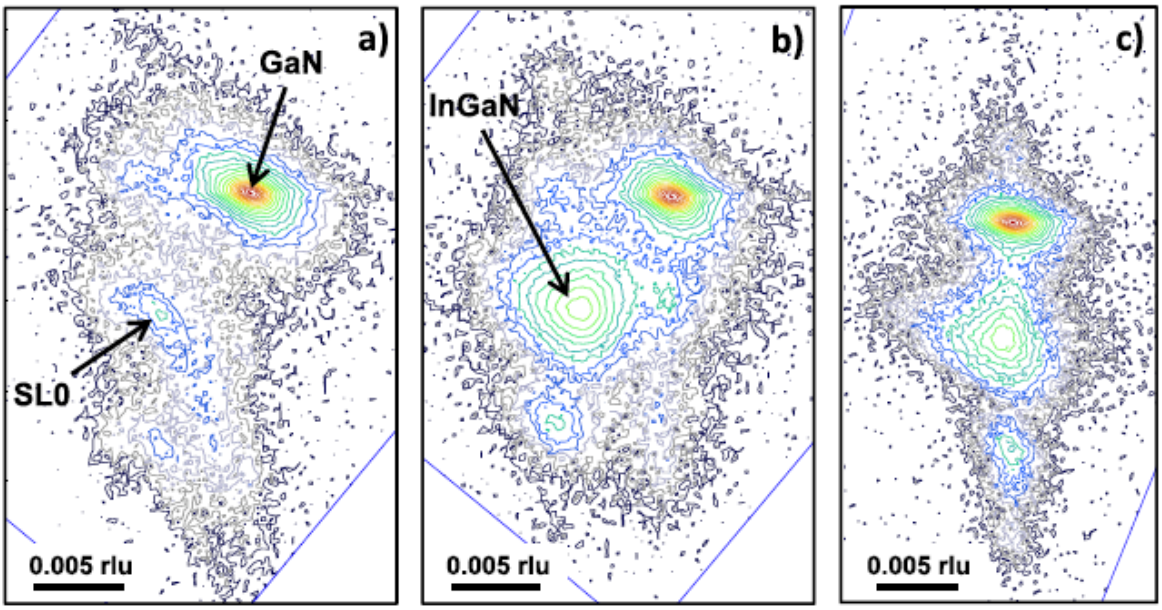

Figure 4.3. Reciprocal space maps taken around the asymmetric $(11\bar{2}4)$ reflection with x-ray scattering plane perpendicular to the stripe direction of (a) patterned 7 period MQW sample with height to width aspect ratio of 0.5 and (b) the same sample after deposition of 7 nm GaN and 250 nm $In_{0.1}Ga_{0.9}N$. (c) Reciprocal space map of the latter sample taken around the asymmetric $(10\bar{1}5)$ reflection with x-ray scattering plane parallel to the stripes.

Figures 4.2c and 4.2d depict SEM images of samples after deposition of 7 nm of GaN and an additional 100 nm of $In_{0.1}Ga_{0.9}N$, respectively, showing fully coalesced films. An AFM image of the sample with a 100 nm thick $In_{0.1}Ga_{0.9}N$ top layer is depicted in Fgure 4.4. While some of the V-defects were already present on the surface of the planar sample, additional defects formed during the coalescence process, as will be discussed in more detail later. All $(11\bar{2}4)$ RSMs recorded from samples with $In_{0.1}Ga_{0.9}N$ cap layers exhibited an additional peak,

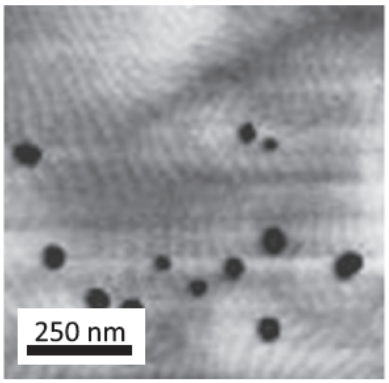

Figure 4.4. Atomic force microscopy image of the sample surface after deposition of 7 nm GaN and 100 nm $In_{0.1}Ga_{0.9}N$ on top of a patterned 7 period MQW sample (greyscale = 5 nm).

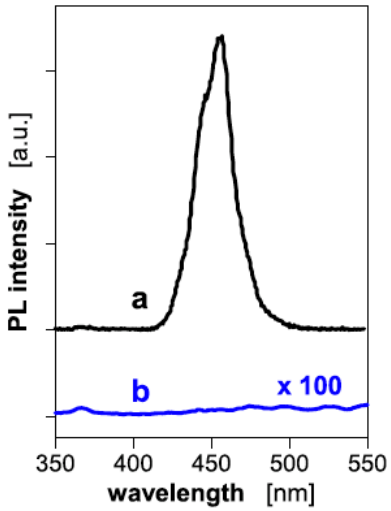

Figure 4.5. Photoluminescence spectra of (a) patterned 7 period (5 nm $In_{0.2}Ga_{0.8}N$/6 nm GaN) MQW sample with height to width aspect ratio of 0.5, and (b) the same sample after deposition of 7 nm GaN.

which was positioned at the side of the MQW peaks, indicating that the $In_{0.1}Ga_{0.9}N$ cap layer adopted an $a_{\perp}$ lattice constant close to the MQW stack in the nanostripes beneath. The $(11\bar{2}4)$ RSM of a sample with a 250 nm thick $In_{0.1}Ga_{0.9}N$ cap layer is depicted in Figure 4.3b. As discussed earlier, all peaks maintained their coherence with the GaN base layer parallel to the stripes, as observed in the $(10\bar{1}5)$ RSM of the same sample (Figure 4.3c).

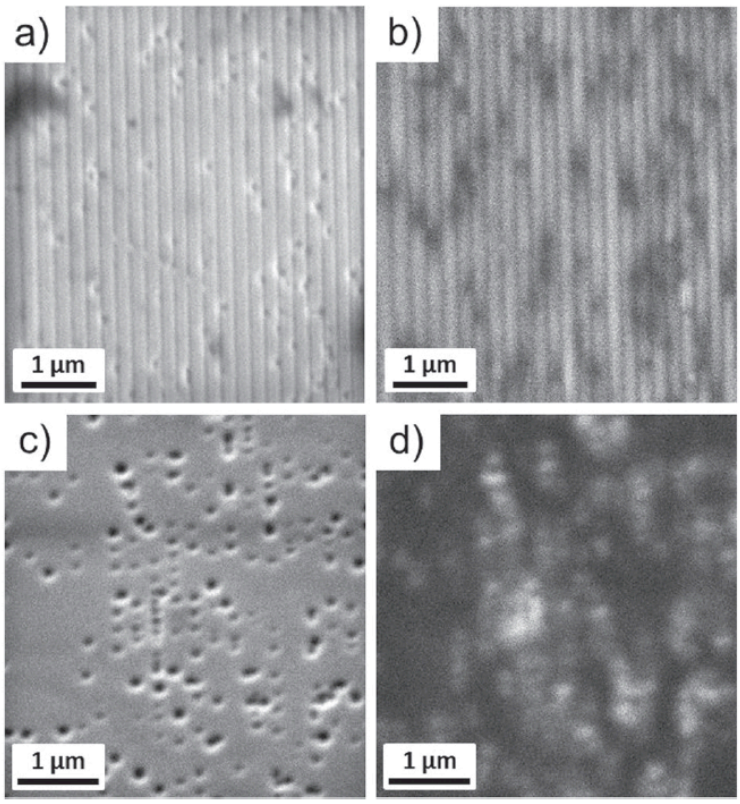

Figure 4.6. Complementary (a) SEM and (b) CL images of patterned 7 period (5 nm $In_{0.2}Ga_{0.8}N$/6 nm GaN) MQW sample with height to width aspect ratio of 0.5; (c) SEM and (d) CL images of the same sample after deposition of 7 nm GaN and 100 nm $In_{0.1}Ga_{0.9}N$.

The as-processed stripe arrays exhibited PL and CL around 450 nm (Figures 4.5 and 4.6b). After deposition of a just 7 nm thick GaN coalescence layer, however, the MQW related luminescence vanished (Figure 4.5). No light emission was observed also from the $In_{0.1}Ga_{0.9}N$ cap layers (Figure 4.6d). TEM investigations of the samples with 100 nm thick $In_{0.1}Ga_{0.9}N$ cap layers revealed that a high number of misfit dislocations formed at the bottom of the MQW stack after the growth of the GaN and $In_{0.1}Ga_{0.9}N$ cap layers (Figures 4.7c and 4.7d). Additional threading dislocations were visible in the coalescence region between the stripes. No misfit dislocations were observed prior to GaN and InGaN cap layer deposition (Figures 4.7a and 4.7b), as reported previously.[137]

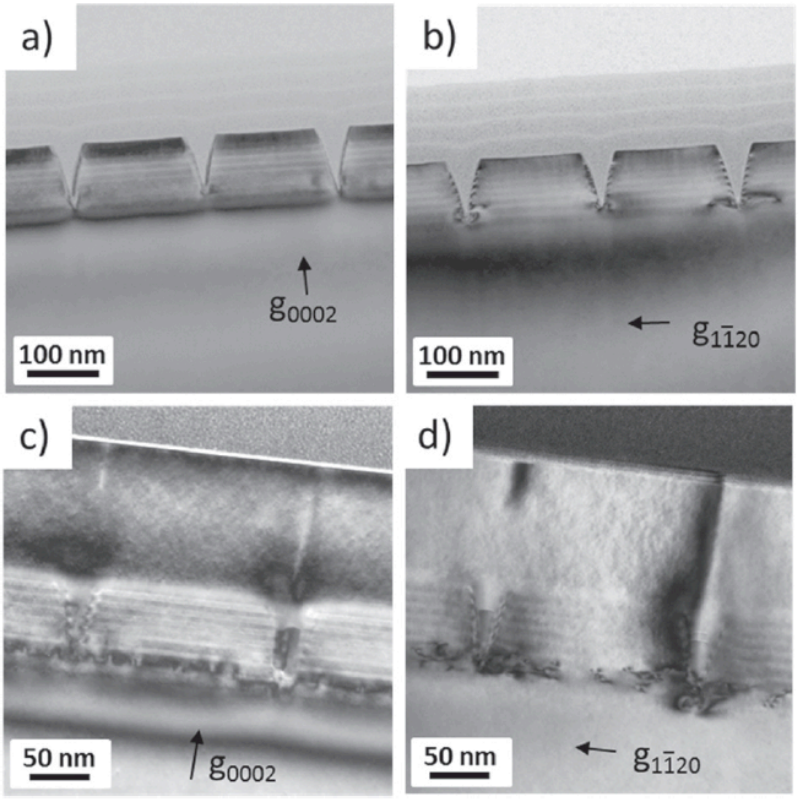

Figure 4.7. Transmission electron microscopy images from patterned 7 period (5 nm $In_{0.2}Ga_{0.8}N$/6 nm GaN) MQW sample with height to width aspect ratio of 0.5 taken in (a) g = 0002 and (b) $g = 11\bar{2}0$ conditions close to the $[1\bar{1}00]$ zone axis, and images of the same sample after deposition of 7 nm GaN and 100 nm $In_{0.1}Ga_{0.9}N$ taken in (c) g = 0002 and (d) $g = 11\bar{2}0$ conditions.

4.2.2 Stripe arrays with an aspect ratio of 1

Previous studies suggested that nanostructures fully relax when the aspect ratio reaches values of 1 or higher.[143,144] As the stripe pitch in the holographic lithography process using a 325 nm He–Cd laser was limited to 200 nm, 23 period (1.9 nm $In_{0.25}Ga_{0.75}N$/6.8 nm GaN) MQW samples were grown and processed into stripe arrays, as illustrated in Figure 4.8a. Initially, GaN coalescence layers were again grown on top of the stripe arrays. Comparing the $(11\bar{2}4)$ RSMs of as-processed and GaN capped samples, now a shift of the $a_{\perp}$ lattice constants of the MQW stack back towards GaN is observed after GaN cap layer growth (figures 4.9 and

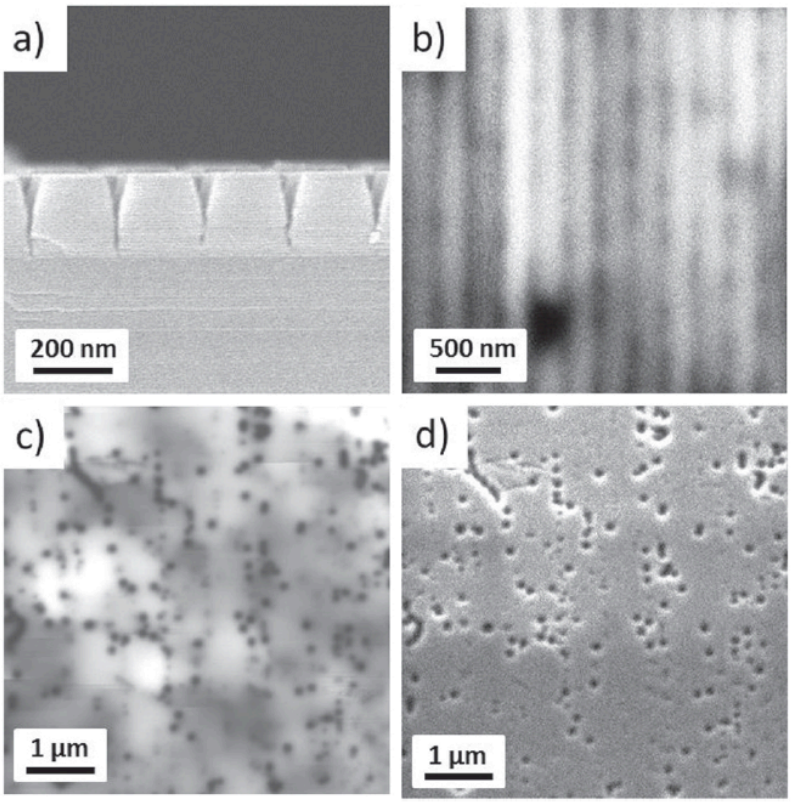

Figure 4.8. (a) Cross-sectional SEM image of patterned 23 period (1.9 nm $In_{0.25}Ga_{0.75}N$/6.8 nm GaN) MQW sample with height to width aspect ratio of 1, CL images of sample (b) after deposition of 14 nm GaN and (c) after deposition of additional 80 nm InGaN. (d) Complementary SEM image of the latter sample.

4.10). The effect was independent of the GaN cap layer thickness, which was varied between 7 and 84 nm. The stripe MQW peaks maintained their position when an additional 80 nm thick $In_xGa_{1-x}N$ layer was deposited after GaN cap layer growth. As observed for the samples with an aspect ratio of 0.5 (Figure 4.3b), the $a_\perp$ lattice constants of the MQWs in the stripes and the $In_xGa_{1-x}N$ cap layers were similar.

In contrast to the samples with an aspect ratio of 0.5, however, the samples with a stripe aspect ratio of 1 exhibited strong luminescence after GaN regrowth, as observed in both CL (Figure 4.8b) and PL measurements. The luminescence from the MQW stripes even increased

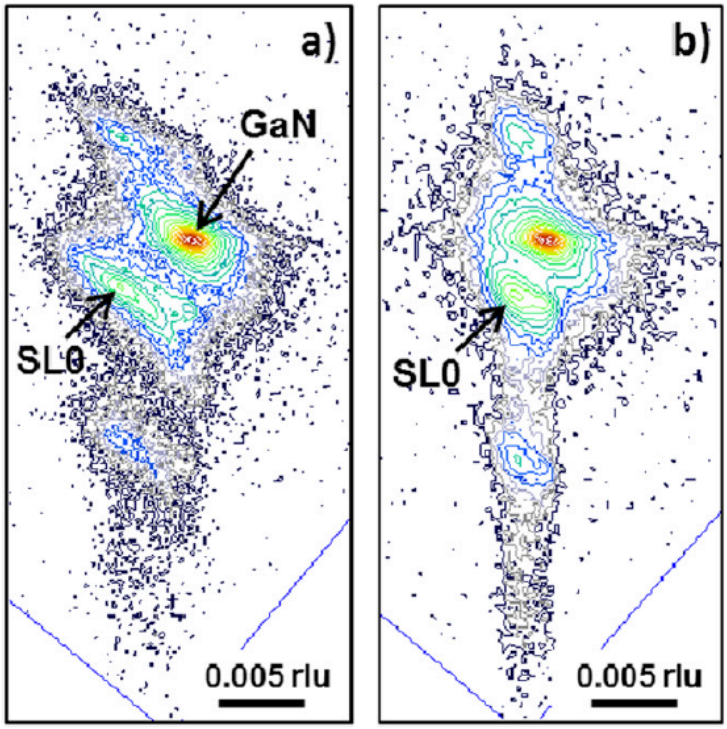

Figure 4.9. Reciprocal space maps taken around the asymmetric $(11\bar{2}4)$ reflection with x-rays perpendicular to the stripe direction of (a) patterned 23 period MQW sample with height to width aspect ratio of 1, and (b) of the same sample after deposition of 14 nm GaN.

after GaN cap layer growth, most likely due to the healing of etch damage during sample heat-up in ammonia and GaN deposition (Figure 4.11). A similar increase in luminescence after annealing of etched nanostripe arrays in ammonia was observed previously.[137] In addition, bright PL and CL was recorded from $In_xGa_{1-x}N$ cap layers, as illustrated in Figure 4.8c for a sample with an 80 nm thick $In_{0.06}Ga_{0.94}N$ top layer in which a 5 period (2.5 nm $In_{0.15}Ga_{0.85}N$/8 nm $In_{0.06}Ga_{0.94}N$) MQW was embedded. The CL and SEM images (Figures 4.8c and 4.8d) again showed the formation of defects at the stripe coalescence fronts.

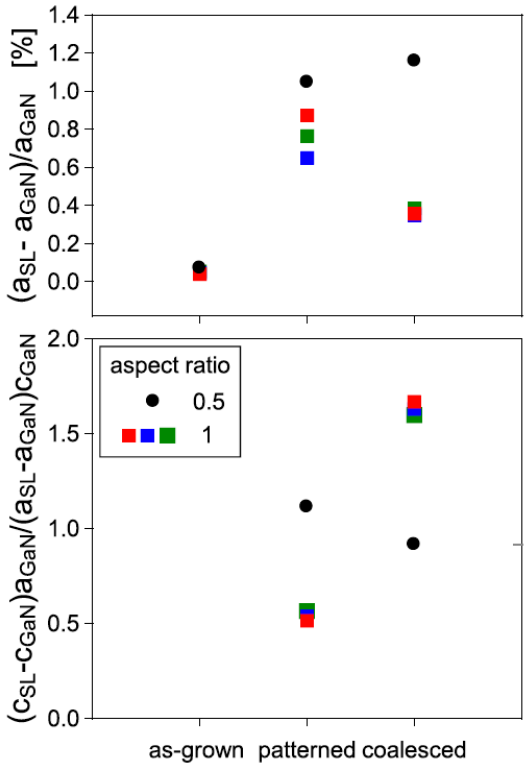

Figure 4.10. In-plane lattice mismatch perpendicular to the stripes (top) and ratio between out of plane and in-plane lattice mismatch perpendicular to the stripes (bottom) for as-grown, patterned, and coalesced samples after GaN and InGaN cap layer deposition with aspect ratios of 0.5 (circles) and 1 (squares). The colors represent different samples. The slight variations between samples originated from non-uniformities over the as-grown MQW wafers.

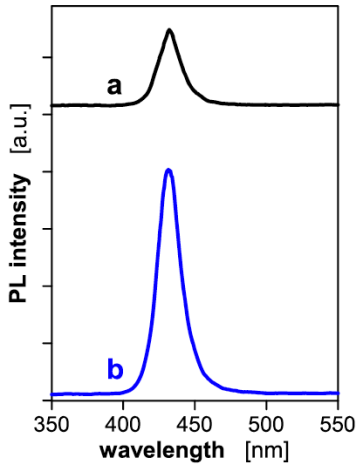

Figure 4.11. Photoluminescence spectra of (a) patterned 23 period (1.9 nm $In_{0.25}Ga_{0.75}N$/6.8 nm GaN) sample with height to width aspect ratio of 1, and (b) the sample after deposition of 14 nm GaN.

4.3 Discussion

Independent of the stripe aspect ratio, all samples exhibited relaxation perpendicular to the stripe direction after processing, combined with strong stripe MQW-related luminescence. As reported previously,[137] no defect formation was observed by TEM, even in the samples with a relatively low aspect ratio of 0.5. Upon sample heat-up and regrowth, however, distinct differences in the behavior of the nanostripe arrays with aspect ratios of 0.5 and 1 were observed. In the case of MQW nanostripe arrays with a stripe aspect ratio of 0.5, misfit dislocations formed at the bottom of the MQW stripes (Figure 4.7). Obviously, during sample heat- up and layer growth, sufficient energy was provided to enable dislocation formation. Due to the absence of an effective primary slip system in *c*-plane (In,Ga)N,[145] MOCVD-grown planar (In,Ga)N films typically relax via V-defect formation, assisted either by threading dislocations and/or stacking faults,[11] and typically no misfit dislocations are found. In the case of patterned samples, however, the locally high shear stresses on the basal plane in the vicinity of the groove edges appear to enable the injection of misfit dislocations.[146] While leading to strong luminescence quenching (Figures 4.5 and 4.6), the misfit dislocation formation only resulted in a very small increase of the $a_{\perp}$ lattice constants of the stripe MQWs. The ratio between the lattice mismatch of the c and a lattice constants ($\Delta c/c$ and $\Delta a_{\perp}/a$), $\Delta c * a/\Delta a * c = (c_{MQW} - c_{GaN}) * a_{GaN}/(a_{\perp MQW} - a_{GaN}) * c_{GaN}$, was determined from the position of the main stripe MQW superlattice peaks to be approximately 0.9, as expected for fully relaxed films ($(c_{InN} - c_{GaN}) * a_{GaN}/(a_{InN} - a_{GaN}) * c_{GaN} = 0.91$) (Figure 4.10).

In contrast to the findings for stripes with A ~ 0.5, the optical properties of the stripe arrays with A ~ 1 did not degrade after regrowth of the (In,Ga)N cap layers (Figure 4.8b). Previous

theoretical studies on the critical dimensions for plastic relaxation of strained nanostructures showed a strong correlation between aspect ratio and relative strain energy. A significant reduction in the relative strain energy of cylindrical structures was observed even for an aspect ratio of 0.5, for which the relative strain energy amounted to only about 10% compared to a planar structure (A = 0). The relative strain energy was less than 5% for A ~ 1. While these calculations were performed for cylindrical structures, similar trends were observed for quantum wires/stripes.[147,148] The absence of defects in the as-processed nanostripe arrays with A ~ 0.5 in this study confirmed that the relative strain energy in the MQW stripes was significantly reduced even at this aspect ratio. The remaining strain energy, however, led to plastic relaxation via misfit dislocation formation during heat-up and cap layer growth, resulting in luminescence quenching. The stripe arrays with A ~ 1, however, maintained their luminescence after cap layer growth, indicating that the lower remaining strain energy in the stripes was insufficient to cause any plastic deformation. In addition, the a⊥ lattice constants measured for the MQW stripes with A ~ 1 decreased after cap layer growth (Figure 4.10). Restraining effects in elastically relaxed InGaAsP surface gratings after burying with thick InP layers were reported previously.[141,149,150] In the case of the stripe arrays/gratings with *A* ~ 1 investigated in this study, the $a_{\perp}$ lattice constant decreased after capping with only 7 nm of GaN. More detailed TEM and cross-sectional CL investigations of samples with an aspect ratio of ~1 are under way and will be presented in a forthcoming report.

As with the $a_{\perp}$ lattice constant, for stripes with A ~ 1, the ratio between the lattice mismatch of the *c* and *a* lattice constants, $\Delta c/c$ and $\Delta a_{\perp}/a$, $\Delta c * a/\Delta a * c$ determined from

the position of the main stripe MQW superlattice peak also changed in the various processing steps, from values of around 0.6 in the as-patterned stage to 1.6–1.8 after cap layer deposition (Figure 4.10). For comparison, the lattice mismatch ratio $(c_{InN} — c_{GaN}) * a_{GaN} / (a_{InN} — a_{GaN}) * c_{GaN}$ for InN with respect to GaN amounts to 0.91. The measured $(c_{MQW} — c_{GaN}) * a_{GaN} / (a_{\perp MQW} — a_{GaN}) * c_{GaN}$ ratios < 0.91 indicated that in the as-processed samples with A ~ 1, most of the lattice mismatch between the stripe MQW stack and the GaN base layer was accommodated by an increase in $a_{\perp MQW}$. For the samples with A ~ 0.5, the same ratio amounted to 1.2 for the patterned and 0.9 for the coalesced sample, with the latter value corresponding to that expected for a fully relaxed layer. Note that no relaxation was seen parallel to the stripe direction for all samples (Figure 4.3c).

Despite the restraining of the (In,Ga)N stripes after cap layer deposition, the $a_{\perp}$ lattice constants of the planar $In_xGa_{1-x}N$ layers grown on top of the stripe arrays were still larger than a_{GaN}, allowing full or partial relaxation of the $In_xGa_{1-x}N$ cap layers perpendicular to the stripe direction. Thereby the final $a_{\perp}(In_xGa_{1-x}N)$ lattice constant can be tuned by the average indium composition of the (In,Ga)N MQWs in the stripe array. As mentioned before, the MQW stacks could also be replaced by thick InGaN layers. The indium composition and/or thickness of the layer prior to patterning are only limited by the onset of defect formation. As the layer thickness needs to be equal or larger than the stripe width to allow elastic relaxation, the required thickness decreases with the pattern width. Hypothetically, full relaxation of the $In_xGa_{1-x}N$ layers could be achieved if the stripe pattern is replaced by a square or rhombohedral pattern. Alternatively, the stripe patterning process could be repeated after the deposition of a thin coalescence layer, by choosing an appropriate angle between the stripes

in the first and second array. In addition, the *a* lattice constant could be further increased in subsequent patterning and cap layer fabrication steps. Prerequisites for successful application of this method for the fabrication of relaxed InGaN layers which could serve as pseudo-substrates are to either mitigate the threading dislocation formation during pattern coalescence (Figures 4.7 and 4.8) or to find methods leading to their annihilation during (In,Ga)N cap layer deposition. Previously, no net increase in threading dislocation density was observed after growth of GaN over Si_3N_4 nanostripe arrays.[151,152] Possibly, the number of threading dislocations observed after coalescence in the samples in this study can be reduced with further optimization of the patterning and coalescence process.

4.4 Conclusions

(In,Ga)N layer deposition on InGaN/GaN MQW nanostripe arrays enabled the tuning of the (In,Ga)N $a_\perp$ lattice constant perpendicular to the stripe direction to values larger than that of GaN. Bright luminescence was recorded from the planar, partially relaxed (In,Ga)N layers grown on top of stripe arrays with a stripe aspect ratio of 1. A stripe aspect ratio of 1 was required to prevent plastic relaxation of the MQW stripes after (In,Ga)N regrowth which resulted in luminescence quenching. While stripe arrays with an aspect ratio of 0.5 plastically relaxed after (In,Ga)N cap layer growth, a slight restraining of the stripe MQWs occurred for samples with A = 1, indicative of elastic behavior.

V. MBE-grown Pseudo-substrates for Reduced Lattice Mismatch

As discussed in Chapter IV, one approach to mitigate the strain in InGaN/GaN heterostructures is to reduce the strain by using a base layer with an in-plane lattice constant larger than that of GaN, enabling higher indium composition layers and improved device efficiencies.[9,125,126,153,154] Several attempts have been made to produce lattice-engineered base layers using patterned substrates,[135,136,155] including the work in Chapter IV, however the fabrication process can be complex often resulting in low yields and throughput. Another approach towards the fabrication of lattice-matched substrates is to directly grow a relaxed InGaN layer to use as a base layer for subsequent growths. While the direct growth of thick InGaN base layers has been investigated using metal-organic chemical vapor deposition (MOCVD),[127,128] it remains difficult to produce high quality relaxed InGaN layers without forming defects. In the case of MOCVD-grown films in the typical Ga-polar orientation, thick InGaN layers tend to relax via the formation of large V-pits which increase in size as the layer thickness is increased.[11,133] Using molecular beam epitaxy (MBE), it is possible to grow thick InGaN layers in a metal-rich environment without forming large defects.[129,130] Additionally, the growth of thick compositionally graded InGaN films with relaxed InGaN top layers has been previously demonstrated for both Ga-polar[131,156,157] and N-polar[158] orientations using plasma-assisted molecular beam epitaxy (PAMBE).

In this chapter, PAMBE-grown N-polar pseudo-substrates (PSs) with a relaxed $In_{0.11}Ga_{0.89}N$ top layer as detailed in reference [158] were explored as templates for the regrowth of thick InGaN layers and InGaN quantum wells (QWs) by MOCVD. The properties of regrown films will be compared to those of co-loaded films grown on N-polar GaN base

layers. The thick N-polar InGaN layers were deposited using a novel digital growth scheme, preventing the formation of hexagonal surface defects which were previously observed when growing thick InGaN films on GaN base layers misoriented towards the GaN $[1\bar{1}00]$ *m*-direction.[41]

5.1 Surface preparation for low temperature regrowths

Prior to beginning regrowth experiments on the InGaN PSs, a brief investigation was conducted to determine the effect of the surface cleanliness on the morphology of regrown layers. When a sample is removed from the MOCVD chamber after growth, the surface begins to oxidize and contaminants in the air accumulate on the sample surface. If the sample is then loaded back into the reactor for subsequent growth, the presence of oxides and contaminants at the regrowth interface can affect the step-flow growth process and result in rough morphology.[159] Furthermore, the interfacial region typically suffers from increased oxygen content which can degrade device performance as will be discussed in Chapter VI. In order to mitigate these issues, the sample surface can be cleaned before regrowth either by chemical cleaning prior to loading in the MOCVD chamber or by heating the sample in the growth chamber to bake off the oxide layer prior to regrowth.

To test the effects of the regrowth surface cleaning procedure, a series of samples were regrown on Ga-polar GaN templates using flow modulation epitaxy (FME) at 610 ºC with N_2 carrier gas. FME has been used in the growth of many semiconductor material systems, and typically consists of pulsing the group III source while the group V source is injected at a constant flow rate, as opposed to atomic layer epitaxy where both precursors are alternated.[160]

The use of FME is particularly useful at low temperatures, mitigating the low decomposition efficiency of NH_3.[92,161] In this study, the TEGa flow was ramped on and off rather than abruptly switched for each cycle. Since this process consists of many cycles, the ramping of the TEGa mass flow controller is less demanding of the reactor hardware than opening and closing pneumatic valves repeatedly which can lead to premature failure of the valves. In each flow modulation cycle, the TEGa flow is ramped from 0 to 1.1 μmol/min over 5 seconds, then held constant at 1.1 μmol/min for 5 seconds, then ramped back down to 0 μmol/min over 5 seconds and held at 0 μmol/min for 9 seconds. The NH_3 flow during the FME process is held constant at 1.5 slm. Each cycle results in around 3.5 Å of GaN growth, and in these samples the process was repeated for 50 cycles for a total of around 17.5 nm GaN growth. A schematic representation of the first two periods of the FME process is shown in Figure 5.1.

Prior to the regrowth of the FME layer at 610 ºC, each sample underwent different surface cleaning procedures. For the first sample, the reactor was heated to 1200 ºC for 2 min, then 50 nm GaN was deposited at 1200 ºC using the typical GaN template growth conditions with TMGa, then the temperature was reduced to 610 ºC and the 50 period FME layer was deposited. The 5x5 μm^2 AFM image of the sample surface is shown in Figure 5.2a. The next

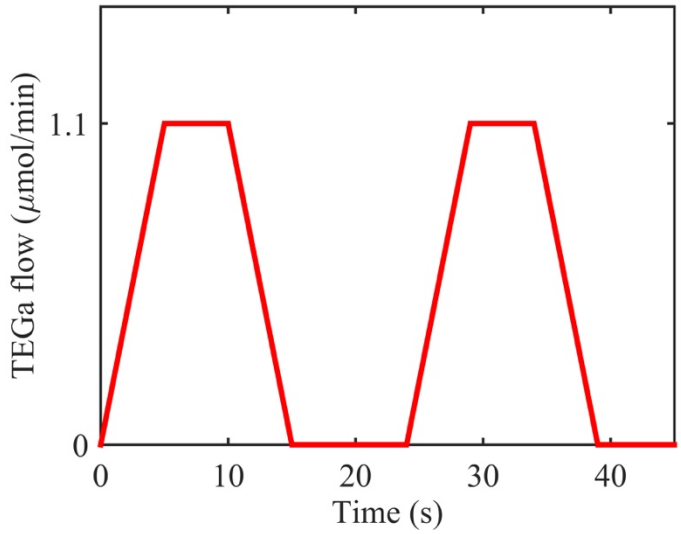

Figure 5.1. Schematic representation of the first two cycles of the flow modulation epitaxy process. The NH_3 flow was held constant at 1.5 slm throughout.

three samples were heated to 1200, 850, or 780 ºC for two minutes (without any growth), then the temperature was decreased to 610 ºC and the FME layers were deposited (Figures 5.2b-5.2d). For the next sample, prior to loading in the MOCVD reactor the surface was chemically cleaned using three cycles of a 15 min UV ozone exposure followed by a 5 min dip in 48% HF. The sample was then loaded into the MOCVD reactor and heated to 780 ºC for 2 min prior to FME layer deposition at 610 ºC (Figure 5.2e). The last sample was chemically cleaned using the same process then loaded into the MOCVD chamber and heated directly to 610 ºC for FME layer growth (Figure 5.2f).

The surface of the regrown FME layer was smoothest for the sample that was heated to 1200 ºC followed by HT GaN deposition, resulting in a surface RMS roughness of 0.22 nm. By regrowing a high temperature layer, the GaN template morphology was completely restored and the surface looks the same as if it was continuously grown (no regrowth). When the sample was only heated to 1200 ºC with no HT GaN deposition, the resulting surface was

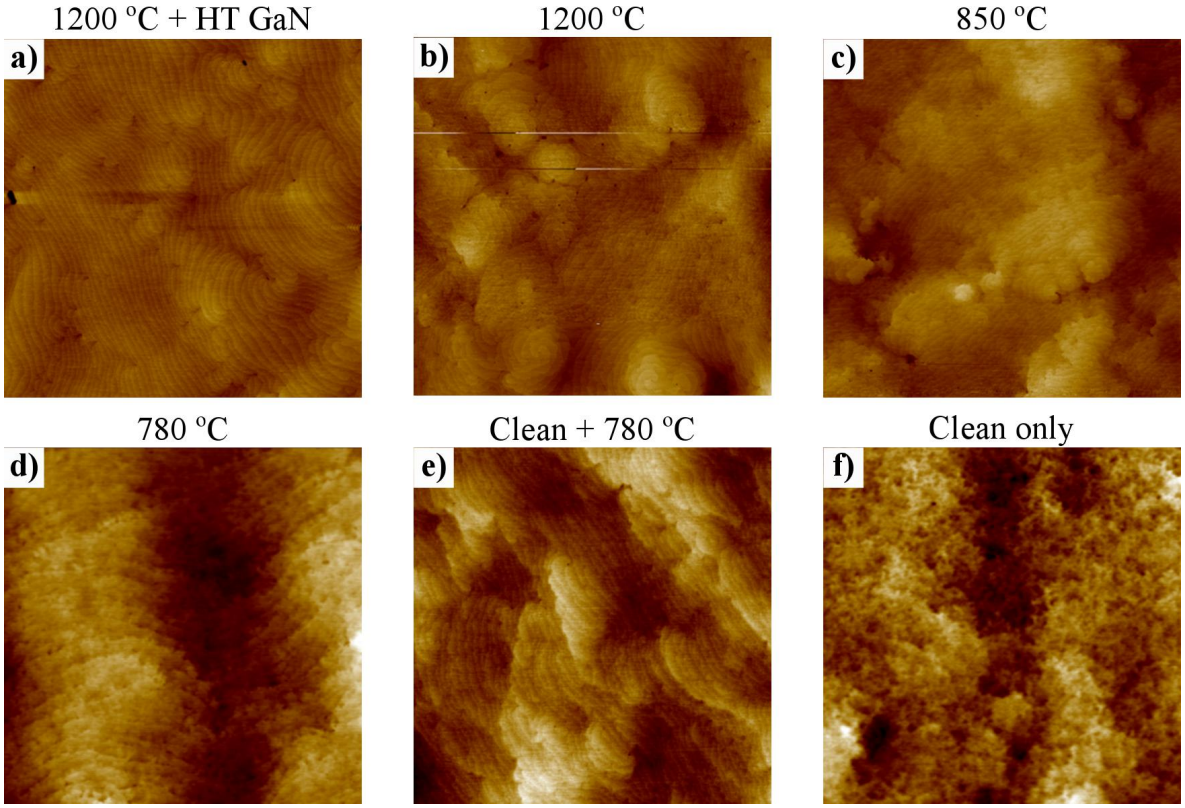

Figure 5.2. 5x5 μm^2 AFM images of 17.5 nm FME GaN regrowth at 610 ºC after a) a 2 min bake at 1200 ºC in the MOCVD chamber followed by HT GaN deposition (RMS=0.22 nm), b) a 2 min bake at 1200 ºC (RMS=0.63 nm), c) a 2 min bake at 850 ºC (RMS=0.80 nm), d) a 2 min bake at 780 ºC (RMS=0.95 nm), e) chemical cleaning plus a 2 min bake at 780 ºC (RMS=0.56 nm), and f) chemical cleaning only (RMS=0.57 nm).

similarly smooth with a slightly higher RMS value of 0.63 nm. Even for the sample which was only heated to 850 ºC, smooth step-flow growth was maintained and the RMS roughness was 0.80 nm. When the temperature was further decreased to 780 ºC, however, the morphology of the layer degraded and the step edges became rough, resulting in a higher surface roughness of 0.95 nm. For the same temperature of 780 ºC, when the surface was chemically cleaned before regrowth the smooth step-flow morphology was restored, resulting in a RMS roughness of 0.56 nm which was lower than the sample grown at 850 ºC without chemical cleaning. Finally, for the sample which was only chemically cleaned and heated

directly to 610 ºC the surface was again very rough with no atomic steps visible in the AFM image. These results indicate that for layers which are regrown above around 850 ºC, surface preparation may not be necessary before regrowth. For samples regrown between around 780-850 ºC, chemically cleaning the surface before regrowth is sufficient to achieve smooth surface morphologies. However, if the regrowth temperature is lower than 780 ºC, even a chemical treatment of the surface may not ensure smooth layer growth, so the resulting morphology may still be influenced by the regrowth interface. In the case of applying these results to the regrowth process on the MBE InGaN PS which will be discussed for the remainder of this chapter, high temperature treatments are not desirable as they would thermally degrade the InGaN PS. For this reason, the chemical cleaning procedure described in this section was used for all regrowths in this chapter, and the regrowth temperature was kept above 800 ºC to minimize the effect of the regrowth interface on the surface morphology.

5.2 MOCVD regrowth of thick InGaN layers using PSs

The PAMBE growth of the graded, relaxed N-polar InGaN PS films on N-polar GaN-on-sapphire templates is detailed in reference [158]. The original sapphire substrate was miscut 4º in the sapphire *a*-direction, resulting in a 4º miscut in the (In,Ga)N $[1\bar{1}00]$ *m*-direction.[40] In all experiments, a standard miscut N-polar GaN-on-sapphire template was co-loaded alongside the PS in order to compare the regrown InGaN layers. The GaN template growth is described elsewhere.[40,41] The InGaN PSs were cleaned using 15 min UV-ozone exposure followed by a 5 min HF dip and loaded into an atmospheric pressure two-flow MOCVD reactor for regrowth. Table 5.1 summarizes the growth parameters for all InGaN regrowth experiments,

performed at temperatures between 800 and 830 ºC using triethyl gallium (TEGa), trimethyl indium (TMIn), and NH_3 as precursors. For all samples besides C, initially a 3-10 nm thick GaN layer was grown with a TEGa flow of 1.4 µmol/min at 800 ºC in N_2 ambient in order to restore the surface step structure typically observed for N-polar films grown by MOCVD on miscut substrates.[40,41] All GaN layers were deposited using an NH_3 flow of 3.2 slm and a TEGa flow of 1.4 µmol/min, while InGaN layers were deposited with a TEGa flow of 2.8 µmol/min and a NH_3 flow of 6 slm to suppress C and O impurity incorporation.[44] For all layers, N_2 carrier gas was flown through the MO precursor bubblers. In layers where H_2 was present in the growth chamber, a mixture of H_2 and N_2 carrier gases was injected separately from the MO precursor lines. In sample A, after the initial 10 nm of GaN growth in N_2, 20 nm GaN was deposited in a H_2/N_2 mixture with a H_2 partial pressure of 170 torr at 800 ºC. For samples B1-B3, 50 nm thick InGaN layers were grown using different carrier gas mixtures and the TMIn flow was adjusted to achieve around 5-10% indium content in each sample. Sample B1 was grown using only N_2 carrier gas, B2 using a mixture of H_2/N_2 ($P_{H_2} = 45$ torr), and B3 using a novel "digital" approach wherein TMIn was injected throughout and the carrier

Table 5.1. MOCVD regrowth parameters for all samples.

Sample	GaN (nm)	(In,Ga)N (nm)	P_{H_2} (torr)	TMIn flow (µmol/min)	Temp. (˚C)
A	10	20	170	0	800
B1	10	50	0	1.4	830
B2	10	50	45	33	830
B3	10	50	0/85	14	820
C	0	50	0/85	14	820
D	3	200	0/85	14	820

gas was alternated between 2 nm in N_2 and 2 nm in H_2/N_2 ($P_{H_2} = 85$ torr), taking advantage of the hydrogen surfactant effect observed previously.[23,41] Sample C contained a 50 nm InGaN layer deposited directly on the InGaN PS using the same digital approach as sample B3. Finally, sample D consisted of only 3 nm GaN in N_2 followed by 200 nm of digital InGaN.

The samples were characterized using an Asylum MFP-3D atomic force microscope (AFM). High resolution x-ray diffraction (XRD) (ω-2θ)-ω reciprocal space maps (RSMs) around the GaN $(11\bar{2}4)$ reflection and ω-2θ scans around the GaN (0002) reflection were measured on a triple-axis Philips/Panalytical Materials Research Diffractometer. Room-temperature photoluminescence was obtained using the 325 nm line of a He-Cd laser with an excitation density of 220 Wcm^{-2}.

5.3 Properties of thick regrown InGaN layers

The surfaces of the relaxed InGaN PSs grown by MBE were comprised of interlacing stripe or fingerlike features about 50 nm wide and separated by about 10 nm wide valleys (Fig. 5.3a, RMS=12 nm). The fingers were elongated along the $[1\bar{1}00]$ direction, perpendicular

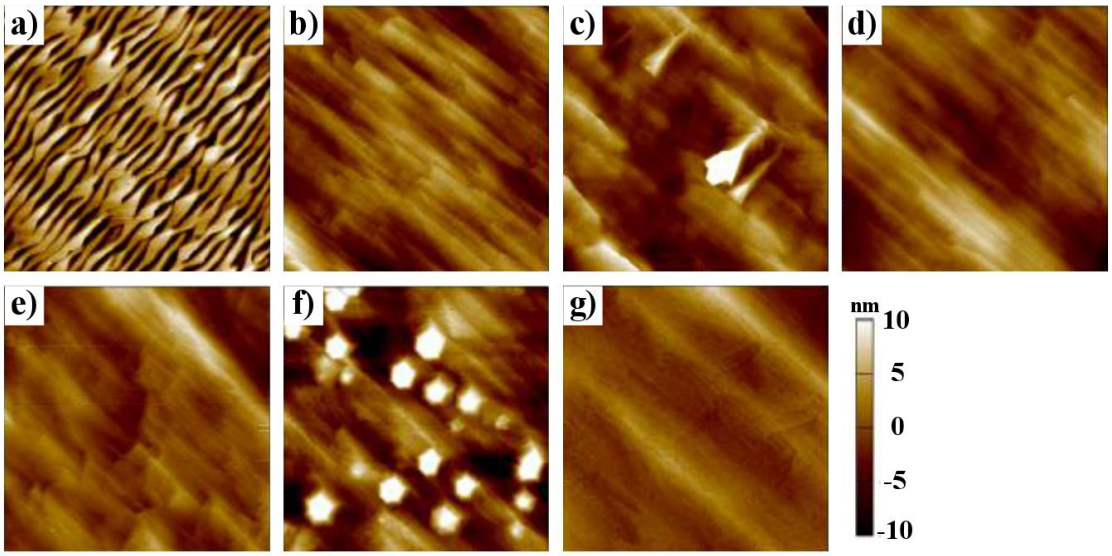

Figure 5.3. 2x2 μm^2 AFM scans of a) the $In_{0.11}Ga_{0.89}N$ PS as grown by PAMBE (RMS=12 nm), b) sample A containing 30 nm GaN (RMS=2.6 nm), c) sample B1 containing 50 nm InGaN grown using N_2 carrier gas (RMS=6.4 nm), d) sample B2 containing 50 nm InGaN grown using H_2 (RMS=2.8 nm), e) sample B3 containing 50 nm digital InGaN (RMS=2.3 nm), f) sample C containing 50 nm digital InGaN grown directly on the PS (RMS=5.6 nm), and g) sample D containing 200 nm digital InGaN (RMS=1.8 nm). The indicated height scale applies to all images besides 1a, where the scale is twice as high.

to the surface steps which resulted from the vicinal substrate. The surface morphology was discussed in detail in reference [158]. To coalesce the surface fingers on the InGaN PSs, a GaN layer was initially deposited at 800 ˚C for sample A. After the growth of 30 nm GaN, the fingerlike features were fully coalesced and the original surface step structure typically observed for MOCVD-grown N-polar GaN layers on misoriented substrates was restored (Fig. 5.3b, RMS=2.6 nm).

For samples B1-B3, 10 nm thick GaN coalescence layers were deposited in N_2 followed by 50 nm thick InGaN layers grown using three different carrier gas injection schemes. Note that the InGaN layers were too thin to assess their composition when deposited on the PSs. Sample B1 was grown using only N_2 carrier gas, resulting in a mostly smooth surface,

however the onset of hillock formation was observed (Fig. 5.3c, RMS=6.4 nm). The indium composition of the InGaN layer on the co-loaded GaN-on-sapphire reference sample was 7.5% extracted from an XRD ω-2θ scan around the GaN (0002) reflection. Since sample B2 was deposited using a H_2/N_2 carrier gas mixture a significantly higher gas phase In composition was used to accommodate for the lower In incorporation in the presence of H_2.[58] In this case, the morphology of the InGaN layer was very smooth (Fig. 5.3d, RMS=2.8 nm) but the indium composition of the InGaN layer on the GaN reference sample was only 3.0%, despite the very high indium mole fraction in the gas phase.[58]

To achieve an InGaN layer with higher indium composition while maintaining a smooth surface, a novel "digital" approach was developed wherein the TMIn flow was kept constant and the carrier gas was alternated between 2 nm grown in N_2 and 2 nm grown in H_2/N_2, effectively creating a short period InGaN/GaN superlattice. In this case, the layer stack behaves like a continuous layer with a composition equal to the average In composition in the superlattice. Sample B3, containing 50 nm digital InGaN, had a smooth surface with no hexagonal hillocks (Fig. 5.3e, RMS=2.3 nm) and the average composition of the InGaN layer on the GaN reference sample was 8.7%.

For sample C, a 50 nm thick digital InGaN layer was deposited directly on the PS surface. Without a GaN layer, the surface after InGaN growth exhibited a high density of hexagonal hillocks (Fig. 5.3f, RMS=5.6 nm).

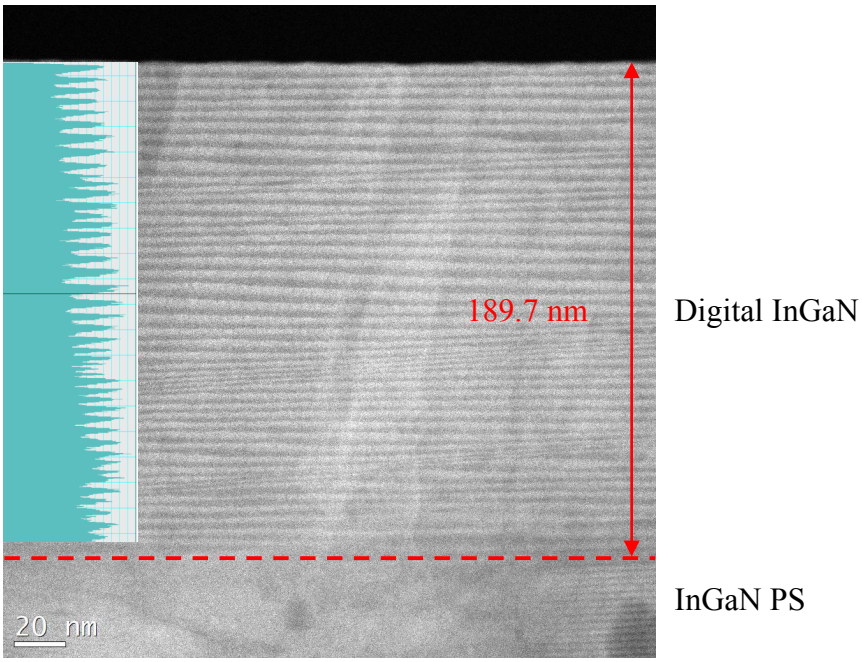

Figure 5.4. Cross-sectional STEM (HAADF) image of digital InGaN layer in sample D (inset: STEM/EDX linescan illustrating indium composition variation throughout the layer).

Finally, sample D consisted of a 3 nm thick GaN coalescence layer grown in N_2 followed by 200 nm digital InGaN. The surface of the layer was again smooth without hexagonal defects (Fig. 5.3g, RMS=1.8 nm). In addition, the alternating layers of the digital superlattice were resolvable using STEM imaging and in EDX linescans taken within the STEM, as shown in Figure 5.4. To observe the strain state of the regrown InGaN layers on the relaxed PSs, XRD reciprocal space maps (RSMs) were measured around the GaN $(11\bar{2}4)$ reflection. In Figure 5.5, the solid black vertical and slanted lines indicate full strain and full strain-relaxation, respectively, while dashed lines indicate contours of constant indium composition. For the original MBE InGaN PS, the compositional grade can be seen in the RSM in Figure 5.5a with the InGaN layer initially strained to GaN and relaxing as the composition increases.

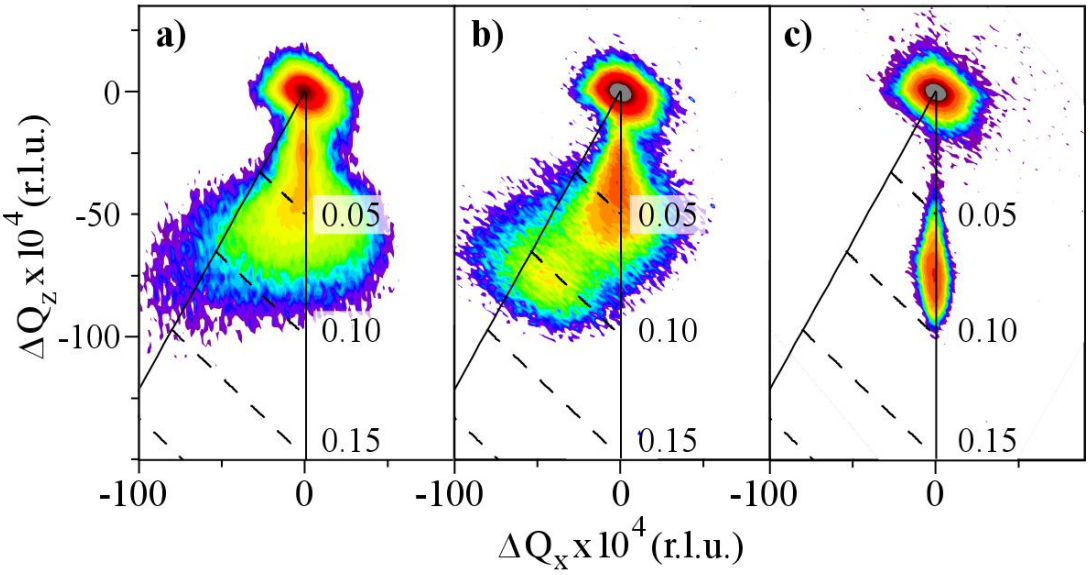

Figure 5.5. XRD reciprocal space maps around the GaN $(11\bar{2}4)$ reflection for a) the $In_{0.11}Ga_{0.89}N$ PS as grown by PAMBE, b) sample D grown on the InGaN PS, and c) sample D grown on the co-loaded GaN template.

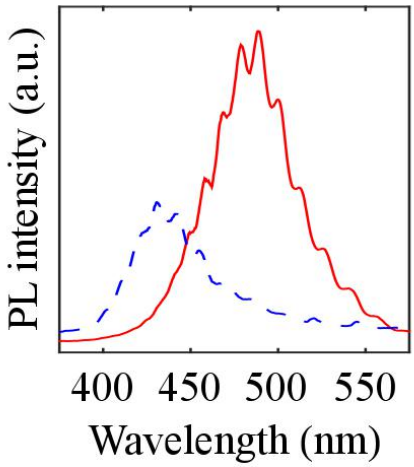

Figure 5.6. Room temperature PL spectra of sample D grown on the InGaN PS (solid line) and on the co-loaded GaN-on-sapphire template (dashed line).

The top layer of the PS is fully relaxed, with an In composition of around 11%. After 200 nm digital InGaN growth, sample D showed an additional InGaN peak near the line of full-relaxation at the same position as the top layer of the PS, indicating that the regrown layer was lattice-matched to the substrate with an In composition of around 11% (Fig. 5.5b). The InGaN

layer regrown on the co-loaded GaN template was fully strained to the GaN base layer and contained less indium at 7.5% (Fig. 5.5c). The room temperature PL spectrum of sample D along with that of the co-loaded GaN reference wafer are displayed in Fig. 5.6. The InGaN layer deposited on the InGaN PS exhibited bright emission at 490 nm, which was twice as intense compared to the luminescence at 430 nm recorded for the layer on the GaN reference sample.

5.4 Discussion

The use of a GaN layer to smoothen the PS surface before InGaN growth proved to be advantageous in mitigating the formation of a high density of large hexagonal surface hillocks during InGaN regrowth. While samples B3, C and D contained the same InGaN layer, sample C, where the InGaN layer was deposited directly on the PS, exhibited a high density of hexagonal surface hillocks, whereas the surface of samples B3 and D remained hillock free and smooth (Figs. 5.3e, 5.3f, 5.3g). While it was beneficial to initiate the regrowth with a GaN layer, the thickness of this layer was kept to a minimum to avoid re-straining of the relaxed InGaN PS.[155] The thinnest GaN coalescence layer used was 3 nm thick in sample D, which proved to be sufficient to suppress the formation of InGaN surface hillocks (Fig. 5.3g). Thin GaN layers were shown to aid the coalescence of nanostripe arrays in past investigations.[155]

In the case of samples B1-B3, with the InGaN layers deposited using different carrier gasses, the composition of the InGaN layers could only be determined for the InGaN layers deposited on the co-loaded GaN templates. Since the regrown InGaN layers were only 50 nm thick and contained similar amounts of indium as the graded PSs, the XRD signal of samples B1-B3 on PSs was dominated by that of the much thicker pseudo-substrate layer.

Of all the carrier gas injection schemes investigated, only the digital InGaN process enabled the deposition of thick InGaN layers with In compositions around 10% while maintaining smooth surfaces. Although the indium composition of sample B1 grown in N_2 was higher, the surface displayed the beginning of hillock formation (Fig. 5.3c). In contrast, the presence of H_2 resulted in significantly smoother surfaces (Fig. 5.3d) due to the hydrogen surfactant effect,[23,41] however reduced the indium incorporation efficiency resulting in very low indium composition layers.[58] Despite the significantly higher TMIn flow during growth compared to samples B1 and B3, the indium composition of the co-loaded GaN reference sample was the lowest at only 3%. While slightly higher indium contents may be achieved in the presence of H_2 at lower growth temperatures, the unintentional C and O impurity incorporation increases at low temperatures[44] and additional defects can form due to the decreased adatom surface mobility.[10] It is worth noting that our previous studies showed that the C and O impurity concentrations were independent of the carrier gas injection scheme and only depended on the growth temperature and precursor flow rates.[41,44] Carbon and oxygen incorporate predominantly on the N-site in GaN, forming deep acceptor and shallow donor states, respectively,[70–72] and can also exist in complexes with Ga-vacancies resulting in the formation of additional states within the bandgap which degrade device performance.[73,74] With the digital InGaN scheme used in sample B3, the resulting surface was smooth despite containing the highest composition of samples B1-B3 (Fig. 5.3e).

When the thickness of the digital InGaN layer was increased in sample D, the InGaN PS allowed for a higher composition as well as superior quality of the regrown layer compared to a conventional GaN template. As predicted, the InGaN layer deposited on the PS assumed

the in-plane lattice constant of the underlying PS, corresponding to $In_{0.11}Ga_{0.89}N$ (Fig. 5.5). The indium composition of the regrown digital layer on the InGaN PS was 50% higher than that grown on GaN, confirming the reduction in the compositional pulling effect with reduced lattice mismatch.[13–15] Furthermore, the luminescence of the InGaN layer on the InGaN PS at 490 nm was twice as bright as that of the layer grown on the GaN base layer at 430 nm (Fig. 5.6), confirming the increase in the indium composition and also indicating an increase in the quantum efficiency. While the latter was predicted previously and associated with the reduction in strain, more detailed optical investigations are needed to verify the mechanism leading to the higher quantum efficiency of the InGaN layers grown on the PSs in this study.[126,153] Similar to earlier observations, the emission wavelengths of both the samples grown on the PSs and on the GaN-on-sapphire templates were longer than expected from the composition of the layers determined by XRD, as the emission in N-polar InGaN layers can be dominated by regions with locally high indium content, resulting in a redshift compared to Ga-polar samples with similar compositions.[36,162] Overall the results confirm the benefits of using a lattice-matched substrate to increase the quality of thick InGaN films while improving indium incorporation efficiency. While thick InGaN layers with relatively low compositions were used in this study, the advantages of using a lattice-matched substrate extend to other heterostructures and to layers containing higher indium compositions as well.

5.5 N-polar multiple quantum well regrowths on InGaN PSs

In addition to the growth of thick InGaN layers, the regrowth of InGaN MQW structures on InGaN PSs was briefly investigated. As with the previous experiments, a thin GaN layer was first deposited on the PS surface at 800 ºC prior to MQW deposition. Three period MQW

stacks consisting of 1.2 nm thick InGaN well layers and 9.5 nm thick GaN barriers were deposited at 760 ºC with a TEGa flow of 1.4 µmol/min and TMIn flows of 1.1 and 1.9 µmol/min with a total of three samples grown (two samples were grown with a TMIn flow of 1.1 µmol/min with slightly different GaN layers deposited before MQW growth). Each sample was co-loaded with a N-polar GaN template to compare the properties of the regrown MQWs.

Room temperature PL emission wavelengths for the three MQW samples are shown in Figure 5.7. Due to the reduction of the compositional pulling effect when using the InGaN PSs, the emission wavelength was around 20 nm longer for all samples grown on the InGaN PSs compared to those grown on co-loaded GaN base layers. It is worth mentioning that since the XRD signal of the InGaN MQWs is much weaker than that of the underlying InGaN PSs, the composition of the InGaN wells could not be determined using XRD. These results

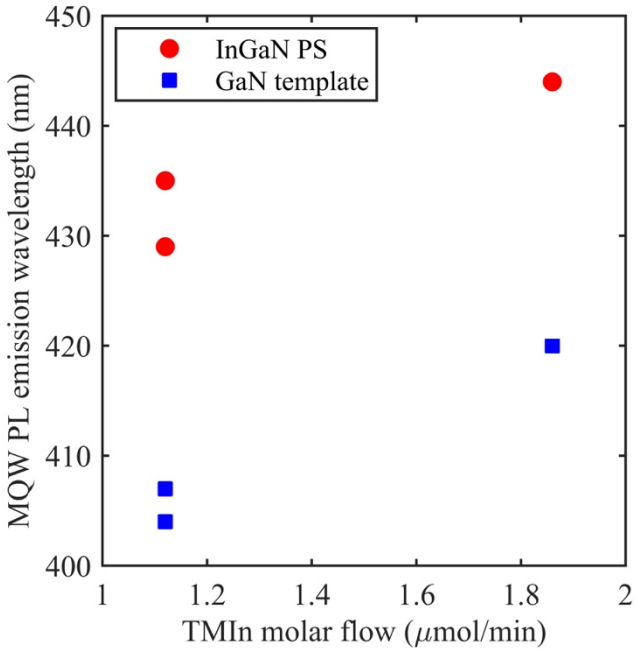

Figure 5.7. Room temperature PL emission wavelengths of N-polar InGaN/GaN triple quantum wells deposited on N-polar InGaN pseudo-substrates (red circles) and on co-loaded GaN base layers (blue squares).

confirm the benefits of using a lattice-matched substrate for quantum well structures such as LEDs, enabling longer emission wavelengths by reducing the strain in InGaN active regions. The low composition InGaN layers in this study were used as a proof of concept, however the benefits will become even more significant if the composition of the InGaN wells is further increased.

5.6 Ga-polar multiple quantum well regrowths on InGaN PSs

While the focus of this chapter has been on N-polar InGaN PSs, Ga-polar PSs were also grown at UCSB using PAMBE. The growth of the Ga-polar PSs is detailed in references [156] and [157]. The $In_{0.10}Ga_{0.90}N$ PSs and Ga-polar GaN base layers were again co-loaded in the MOCVD reactor for regrowth, and 5 nm GaN was deposited using TEGa (2.2 μmol/min) and NH_3 (3.2 slm) in N_2 carrier gas. Three period MQW stacks were deposited, this time using InGaN barriers. The well layers were grown with a TEGa flow of 2.2 μmol/min and a TMIn flow of 0.73 μmol/min, and the barriers were grown using the same TEGa flow with a TMIn flow of 0.33 μmol/min. The use of InGaN barrier layers, while somewhat complicating the growth process, is optimal for lattice-matched growths so that no layers with lattice constants smaller than that of the substrate are introduced. For each sample grown between 780-850 ºC, the growth temperature was kept constant for the entire regrowth process. When multiple samples were grown at the same temperature, only the sample cleaning before growth and the regrowth heating procedure were varied, and will not be discussed in detail.

The room temperature PL emission wavelengths for all Ga-polar samples grown on InGaN PSs and on GaN base layers are shown in Figure 5.8. Similar to the N-polar MQWs, the Ga-polar MQWs grown on the InGaN PSs resulted in PL emission at significantly longer

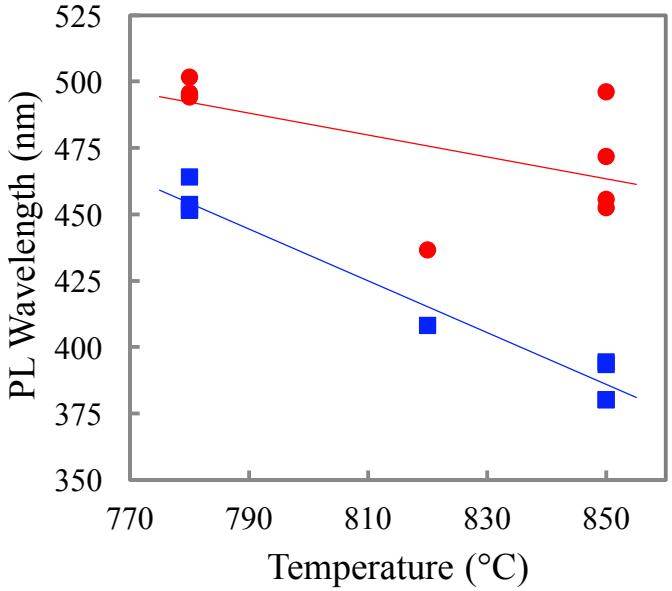

Figure 5.8. Room temperature PL emission wavelengths of Ga-polar InGaN/GaN triple quantum wells deposited on Ga-polar InGaN pseudo-substrates (red circles) and on co-loaded GaN base layers (blue squares).

wavelengths than those grown on GaN base layers due to a reduction in the compositional pulling effect. Interestingly, the redshift of the samples grown on the InGaN PSs was more pronounced for higher growth temperatures. This observation is consistent with both theoretical and experimental reports on the compositional pulling effect, where higher growth temperatures result in stronger compositional pulling.[14] These results serve to demonstrate the effectiveness of using a lattice-matched substrate to increase indium incorporation efficiency in any crystallographic orientation, as the compositional pulling effect is driven by lattice mismatch which does not depend on orientation.

5.7 Conclusions

In summary, the MOCVD regrowth of thick InGaN films on relaxed N-polar InGaN pseudo-substrates was investigated. A novel digital InGaN growth scheme alternating the use of N_2 and H_2 as carrier gas was developed and allowed the deposition of 200 nm thick relaxed N-polar $In_{0.11}Ga_{0.89}N$ films with smooth surfaces and superior properties compared to films grown using traditional carrier gas injection schemes. The InGaN layers regrown on the InGaN PSs assumed the in plane lattice constant of the relaxed PSs and contained higher amounts of indium compared to InGaN layers deposited on GaN reference samples due to a reduction of the lattice mismatch and the associated compositional pulling effect. In addition, the InGaN layers deposited on the relaxed PSs displayed room temperature photoluminescence twice as intense as the InGaN films deposited on the GaN reference samples with a redshift of 60 nm. Additionally, N-polar MQW samples deposited on the InGaN PSs resulted in a redshift of around 15 nm compared to GaN reference samples, while Ga-polar MQW samples resulted in a redshift of similar magnitude which increased for higher growth temperatures. These results indicate that the digital epitaxy scheme combined with the use of relaxed InGaN substrates is a promising approach for the fabrication of thick InGaN films and quantum wells with superior optical properties in the green region and beyond, regardless of the crystallographic orientation.

VI. Impurity Incorporation in N-polar Films at Low Temperature

6.1 Introduction to unintentional impurities in (In,Ga)N

For devices which contain high indium contents, the active regions and subsequent layers must be deposited at low temperatures where additional care must be taken to prevent unintentional impurity incorporation. In the past N-polar layers have been shown to have increased oxygen incorporation compared to Ga-polar films.[42] More recently, N-polar films with residual oxygen contents as low as 2×10^{16} cm^{-3} have been reported for smooth GaN films grown on miscut substrates at high growth temperatures under optimized conditions.[27] At reduced growth temperatures, however, increased oxygen content had again been observed in addition to elevated carbon impurity incorporation in layers grown with trimethyl gallium as precursor, due to incomplete removal of methyl groups from the growing surface.[43] The carbon incorporation could be suppressed when using triethyl gallium as precursor,[27] due to the easier removal of ethyl groups via β-elimination.[76]

Both oxygen and carbon incorporate predominantly on the nitrogen sites in GaN, forming shallow donor and deep acceptor states respectively.[70,71,74] While oxygen itself is a shallow donor, it can also exist in complexes with Ga-vacancies. In the case of carbon, both isolated carbon and C-V_{Ga} complexes form deeper states in the band gap. Since these impurity states can significantly impact device performance, it is important to be able to understand and control the levels of these unintentional dopants.

Here we present a comprehensive study on the interplay of precursor selection and growth conditions on impurity incorporation over a wide range of growth parameters compatible to the (In,Ga)N growth regime.

6.2 Growth of SIMS stacks

While the focus of this chapter is to study impurity incorporation in the low temperature (In,Ga)N growth regime, it is difficult to grow thick InGaN layers for SIMS analysis since in the N-polar orientation hexagonal hillocks tend to form during the growth of thick layers in nitrogen ambient, even when grown on misoriented substrates.[27] These irregular surface features will affect the impurity incorporation, due to step bunching and the presence of multiple crystallographic facets. In order to avoid morphological degradation and to maintain step-flow growth, all (In,Ga)N layers in the SIMS stacks in this study were grown in the presence of 1 slm hydrogen. As the presence of hydrogen suppresses indium incorporation, the indium content in layers grown in the presence of TMIn was below 4% for all layers studied. Using this technique, thick layer stacks up to around 2 μm could be grown while maintaining morphologies similar to the original templates used (Figs. 6.1a and 6.1b). While the RMS roughness of the stacks increased from 1.3 to 12.3 nm for a 5×5 μm^2 area due to the thick layer growth, no additional crystallographic features such as hillocks were formed. A similar approach was pursued in previous studies, which also showed that the C and O impurity incorporation was independent of the carrier gas used (H_2/N_2). In addition the investigations confirmed that the impurity concentration in InGaN/GaN MQW stacks, where

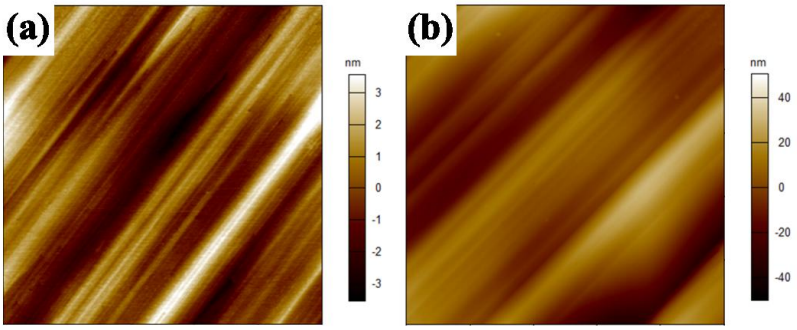

Figure 6.1. 5×5 μm^2 AFM scans showing the sample surface after (a) GaN template growth and (b) growth of a 2 μm thick SIMS stack.

the $In_{0.2}Ga_{0.8}N$ wells were grown in pure N_2 was similar to the impurity levels in such MQW stacks where H_2 was added during InGaN well deposition, resulting in a negligible indium content in the wells, similar to the growth conditions in this study.[27] For these reasons it is assumed that the impurity incorporation discussed herein will apply to all layers grown in the presence of TMIn in the gas phase, regardless of the indium content in the layers.

The substrates used in this study were c-sapphire miscut 4 degrees towards the a-direction, resulting in a GaN layer miscut toward the GaN m-direction. Substrates were loaded into an atmospheric pressure two-flow MOCVD reactor (equipped with a load-lock) and template growth was initiated with a high temperature nitridation step, followed by nucleation layer growth and deposition of a thick 1 μm GaN layer at 1200 ˚C. Fig. 6.1a shows the surface morphology of the resulting template, with a RMS roughness of 1.3 nm for a 5×5 μm^2 image. Further details of the template growth and their properties been presented elsewhere.[27,40] Next, layer stacks were grown at different temperatures (750-950 ˚C), trimethyl gallium (TMGa, 0-9.0 μmol/min), triethyl gallium (TEGa, 0-6.5 μmol/min), trimethyl indium (TMIn, 0-56 μmol/min), bis-cyclopentadienyl magnesium (Cp_2Mg, 0-0.69 μmol/min), and NH_3 flows (1 to 6 slm). A variety of different combinations of precursors were used, and when not otherwise

mentioned the standard flows were 3.2 slm NH_3, 4.6 μmol/min TEGa, 6.5 μmol/min TMGa, 0.12 μmol/min Cp_2Mg, and 37 μmol/min TMIn with only one parameter varied for each series of layers presented. For a TEGa flow of 4.6 μmol/min and a TMGa flow of 6.5 μmol/min, the corresponding growth rates were 0.7 Å/s and 0.8 Å/s respectively and the growth rate was only dependent on the Ga source molar flow in the range studied, independent of all other growth parameters. The around 200-nm-thick layers of interest were separated by at least 100-nm-thick Si-doped spacer layers so that each layer could be easily identified. High purity precursors and gasses were used to minimize impurity incorporation. Secondary ion mass spectroscopy (SIMS) analysis was performed on all samples by Evans Analytical Group. The detection limits for each species were as follows: carbon, 1×10^{16} cm^{-3}; oxygen, 1×10^{16} cm^{-3}.

6.3 Oxygen incorporation

Fig. 6.2 illustrates the oxygen concentration determined by SIMS for GaN layers grown under a variety of conditions. As expected from the higher stability of Ga_2O_3 at reduced temperatures, the O content slightly increased from 3 to 4 × 10^{16} cm^{-3} to 6 × 10^{16} cm^{-3} when the growth temperature was decreased from 950 to 750 °C for layers grown with a V/III ratio of 28,000, as shown in Fig. 6.2a. For layers grown using only TEGa or TMGa with a NH_3 flow of 3.2 slm the oxygen concentration was largely independent of the Ga precursor flow,

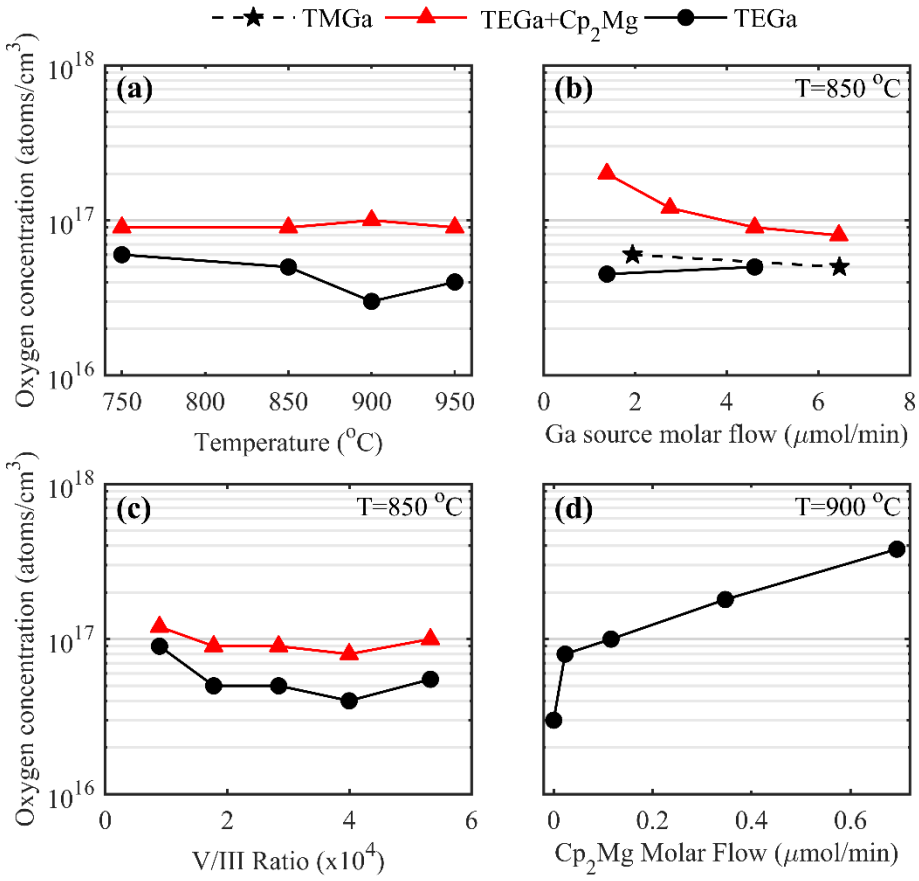

Figure 6.2. Oxygen concentration determined by SIMS as a function of (a) temperature, (b) Ga source flow at 850 ˚C, (c) V/III ratio by changing the NH_3 flow at 850 ˚C, and (d) Cp_2Mg flow at 900 ˚C. Unless specifically noted, the precursor flows used were 3.2 slm NH_3, 4.6 µmol/min TEGa, 6.5 µmol/min TMGa, 0.12 µmol/min Cp_2Mg, and 37 µmol/min TMIn with only one parameter varied for each series of layers presented.

ranging between 4 and 6×10^{16} cm^{-3} (Fig. 6.2b). Since O occupies the N site in GaN, the oxygen content in the layers decreased from to 9×10^{16} cm^{-3} for films grown with a V/III ratio of 9,000 to values between 4 and 6×10^{16} cm^{-3} at higher V/III ratios above 18,000 (higher NH_3 flows) due to the higher N overpressure in the gas phase (Fig. 6.2c). When TMIn was added to the gas phase no marked change in the oxygen incorporation was observed.

In p-type GaN:Mg films, the O content in the layers increased sharply upon the addition of 0.02 μmol/min Cp_2Mg into the gas phase, and increased further for higher Cp_2Mg flows (Fig. 6.2d). The additional O incorporation in the presence of Mg can be explained by the higher bond strength of 394 kJ/mol between Mg and O compared to 285 kJ/mol for the Ga-O bond. At a constant Mg flow, the O incorporation was largely independent of growth temperature and V/III ratio in the investigated regime, ranging from 8×10^{16} cm^{-3} to 1×10^{17} cm^{-3} (Figs. 6.2a and 6.2c). Finally, as the TEGa flow was increased in the presence of Cp_2Mg the O level decreased for higher TEGa flows. Since the Cp_2Mg flow was kept constant as the TEGa flow was increased, this led to a lower fraction of Mg in the gas and solid phases and thus a lower fraction of Mg-O bonds formed compared to Ga-O bonds, which dissociate more readily (Fig. 6.2b). These results indicate that while films with low oxygen content can be grown under a variety of growth conditions, oxygen levels are weakly dependent on the growth temperature and V/III ratio and can be most effectively controlled by using a low Mg:Ga ratio.

6.4 Carbon incorporation

The dependence of carbon incorporation on all growth parameters studied is shown in Fig. 6.3. The C content in layers grown using only TEGa did not depend on the growth temperature in the explored range (Fig. 6.3a), and only showed a very weak dependence on TEGa flow and V/III ratio, ranging from 2 to 5 × 10^{16} cm^{-3}, decreasing with increasing V/III ratio (Figs. 6.3b and 6.3c). On the contrary, films grown using TMGa showed a strong dependence on TMGa flow and V/III ratio (Figs. 6.3b and 6.3c). When the flow of TMGa was increased from 1.9 to 9 µmol/min the C incorporation increased from 3 × 10^{17} to 2 × 10^{18} cm^{-3} as more methyl

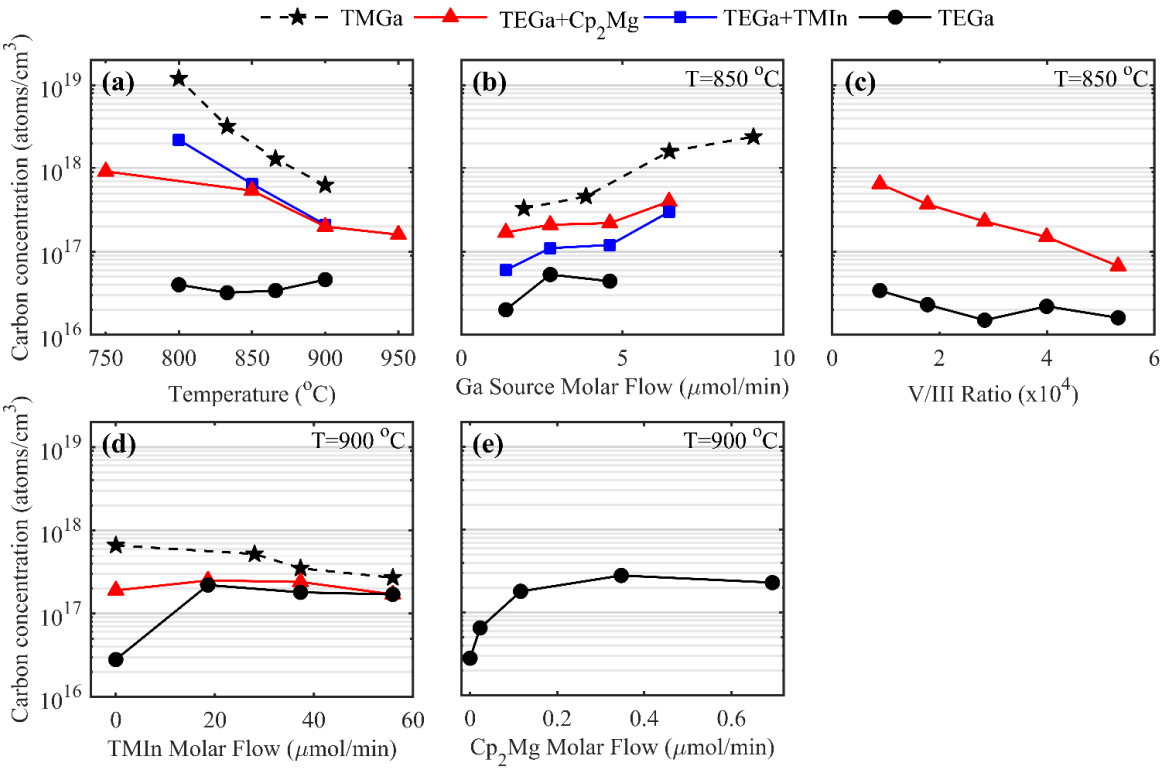

Figure 6.3. Carbon concentration determined by SIMS as a function of (a) temperature, (b) Ga source flow at 850 ˚C, (c) V/III ratio by changing the NH_3 flow at 850 ˚C, (d) TMIn flow at 900 ˚C, and (e) Cp_2Mg flow at 900 ˚C. Unless specifically noted, the precursor flows used were 3.2 slm NH_3, 4.6 µmol/min TEGa, 6.5 µmol/min TMGa, 0.12 µmol/min Cp_2Mg, and 37 µmol/min TMIn with only one parameter varied for each series of layers presented.

species were provided in the gas phase. The C content decreased from 6×10^{17} to 7×10^{16} cm^{-3} with increasing V/III ratio (NH_3 flow) during growth. Similar to oxygen, C and N occupy the same lattice site and the C incorporation decreases as more N species are present.

The strong impact on the C incorporation into films grown with TMGa as precursor was also observed when changing the growth temperature. As the temperature was increased from 800 to 900 °C, the carbon content was reduced from above 1×10^{19} to 6×10^{17} cm^{-3}. At higher growth temperatures the TMGa and NH_3 precursor molecules are more completely pyrolized, leading to lower incorporation of methyl species.[163] More complete NH_3 pyrolysis increases the concentration of hydrogen species present which aid in the removal of methyl ligands from Ga molecules. The formation of methane from methyl radicals is also enhanced due to the more efficient cleavage of Ga-CH_3 bonds in the gas phase and on the surface at elevated temperatures. In contrast to the growth with TMGa, the ethyl groups from TEGa are removed via β-elimination[164] and the activation energy for the ethyl removal process is significantly lower. In addition, a C-C double bond is formed and no methyl radicals are present during growth. Therefore, the C content in the layers grown with TEGa did not show a strong temperature dependence in the investigated regime, and a much weaker dependence on TEGa flow and V/III ratio.

For (In,Ga)N layers grown with TMIn and TEGa, the C incorporation was significantly higher than in the absence of TMIn (Fig. 6.3d). As mentioned previously, 1 slm of H_2 was added to the N_2 carrier gas for all layers grown in the presence of TMIn in order to achieve smooth surfaces so that the impurity incorporation was not affected by the presence of step bunching or additional surface facets. While the In-C bond (47 kcal/mol) is weaker compared

to the Ga-C bond (60 kcal/mol),[76] upon the dissociation of TMIn, reactive methyl radicals are formed which can bond with Ga species resulting in an increased C incorporation. This ligand exchange process can occur either in the gas phase[165] or on the surface. For this reason, C incorporation occurred even for layers grown in hydrogen carrier gas when only negligible amounts of indium atoms were incorporated into the solid phase. Similar methyl exchange reactions have been observed for traditional III-V semiconductors previously.[76] For high TMIn flows the carbon concentration did not further increase, most likely because the lowest TMIn flow used in this study (19 μmol/min) already provided a higher molar amount of methyl radicals than there were Ga species (4.6 μmol/min TEGa) to exchange with. In addition, in the case of (In,Ga)N films grown with the TMGa precursor, a decrease in C incorporation was observed with increasing TMIn flow (Fig. 6.3d). While less pronounced in this compared to an earlier study,[27] the C content in the layers dropped from 6 to 3×10^{17} cm^{-3} with increasing TMIn flow. Previously this effect was associated with an indium catalyzed desorption of methyl radicals from the surface, as indium atoms are known to accumulate on the surface and act as surfactants even when not incorporated into the crystal lattice.[61] This circumstance could have also contributed to the weak dependence of the C incorporation on the TMIn flow at higher flows for films grown with TEGa (Fig. 6.3d).

Similar to GaN films grown with the TMGa precursor, films deposited in the presence of TMIn showed a distinct decrease in C content from 2×10^{18} to 2×10^{17} cm^{-3} as the growth temperature was increased from 800 to 900 °C due to the more efficient pyrolysis of CH_3-metal bonds and formation of methane (Fig. 6.3a). A significant increase in the C content from 6×10^{16} to 3×10^{17} cm^{-3} was again observed as the TEGa flow was increased from 1.4 to 6.5

μmol/min in the presence of TMIn, due to the higher availability of Ga atoms with which ligand exchange could occur (Fig. 6.3b).

In GaN:Mg layers grown using TEGa and Cp_2Mg, the C incorporation was significantly higher than in films grown with TEGa alone (Fig. 6.3e), as observed for layers grown with TEGa and TMIn. When the Cp_2Mg flow was increased, the C level initially increased sharply and then leveled out at around 2 to 3 × 10^{17} cm^{-3} for Cp_2Mg flows above 0.1 μmol/min. In the absence of methyl radicals, it is likely that the C incorporation resulted from the decomposition of cyclopentadienyl groups within the investigated MOCVD growth temperature regime. At these elevated temperatures there are numerous pathways by which Cp groups could decompose forming methyl radicals and resulting in an increased C content.[166] In addition, when TMIn was present in the gas phase along with TEGa and Cp_2Mg, the C incorporation did not further increase even for very high TMIn concentrations, despite the addition of methyl species (Fig. 6.3d). This is most likely again related to the circumstance that methyl groups were supplied in excess of Ga and Mg species and the potential catalytic effect of adsorbed indium species as discussed above. When the growth temperature of the GaN:Mg layers was increased from 750 to 950 °C, a decrease in C content from 9 to 1.5 × 10^{17} cm^{-3} was observed similar to films deposited with TMIn or TMGa (Fig. 6.3a). This is again most likely due to the more efficient cleavage of metal-C bonds and NH_3 decomposition providing H species to react with methyl radicals to form methane. Finally, for these GaN:Mg layers the C concentration could again be reduced significantly from 6 × 10^{17} to 6 × 10^{16} cm^{-3} by increasing the V/III ratio from 9,000 to 53,000 (increasing the NH_3 flow from 1 slm to 6 slm). Similar results were observed when the V/III ratio was increased by either increasing

the NH_3 flow (Fig. 6.3c) or decreasing the TEGa flow (Fig. 6.3b). As discussed before, since C incorporates on N site, the increased N overpressure suppresses the C incorporation. In addition, increasing the V/III ratio leads to a higher concentration of hydrogen radicals from NH_3 decomposition available to remove methyl species from the surface. These results indicate that in order to minimize C content in p-type GaN:Mg films, it is best to use a high V/III ratio with low Mg and TEGa flows, at a as high of a temperature as possible without degrading underlying layers.

6.5 Conclusions

The dependence of unintentional oxygen and carbon incorporation on precursor selection and growth conditions has been studied using SIMS under conditions relevant to low temperature (In,Ga)N growth. Oxygen concentrations as low as 3×10^{16} cm^{-3} were achieved for films grown using TEGa or TMGa irrespective of the Ga source flow. Increasing the growth temperature or the V/III ratio (NH_3 flow) resulted in slightly lower oxygen incorporation for these layers. In layers grown in the presence of Cp_2Mg the oxygen content increased with increasing Mg:Ga ratio in the gas phase. The residual carbon incorporation was the lowest in GaN films grown with TEGa alone. A higher carbon content was found in films deposited in the presence of Cp_2Mg, TMGa, or TMIn, but could be decreased again significantly by increasing the growth temperature. In addition, higher V/III ratios, either by increasing the NH_3 flow or decreasing the Ga precursor flow, resulted in reduced carbon incorporation. With careful tuning of the growth conditions, carbon concentrations as low as 2×10^{16} cm^{-3} were achieved.

VII. Low Temperature p-GaN Growth for Tunnel Devices

For the TFET and tunnel diode structures discussed in Chapter II, low resistance p-GaN layers and p-contacts are imperative for achieving steep device turn on at low reverse biases. The fabrication of high quality p-GaN layers with high hole concentrations is challenging due to several factors including limited dopant solubility,[167] high acceptor activation energy, and self-compensation effects related to the presence of donor-like native defects or complexes involving native defects.[74] For optimal band alignment in a tunnel junction device, high electron and hole concentrations are desirable near the p-n junction. In the case of n-doped GaN:Si films, electron concentrations above 10^{19} cm^{-3} are readily achievable, while higher concentrations over 10^{20} cm^{-3} can be achieved with optimized growth processes. On the other hand, maximum hole concentrations around 2-5 x 10^{17} cm^{-3} are typically observed for p-doped GaN:Mg layers when [Mg] is around 2 x 10^{19} cm^{-3}, with a decrease in hole concentration for higher Mg concentrations due to acceptor self-compensation.[168] In addition, heavily Mg-doped layers suffer from morphological degradation due to Mg clustering and the formation of polarity inversion domains. In the context of tunneling devices, these issues can lead to low tunneling probability due to improper band alignment as well as highly resistive p-layers and poor p-contact performance.

While much previous work has focused on the growth optimization of Ga-polar p-GaN layers using MOCVD, there are far fewer reports on the fabrication of N-polar p-GaN layers. At UCSB the basic electrical properties of N-polar p-GaN layers were explored for layers grown at high temperature.[82] That report revealed that for layers grown at 1080 ºC, the resistivity, specific contact resistance, hole concentration, mobility, and activation energy of

N-polar samples were comparable with those of Ga-polar samples. The primary difference observed was the increased robustness of the morphology of N-polar layers with high Mg doping compared to the rough morphology that resulted from polarity inversion from Ga- to N-polarity in Ga-polar layers with high Mg doping. While other groups have reported on the growth of N-polar devices with p-layers such as LEDs, to the best of our knowledge there are no other reports on the electrical properties of N-polar p-layers in the literature.

When depositing p-GaN films on top of active regions with high In contents such as those needed for polarization-engineered N-polar tunnel devices, the growth temperature must be reduced compared to the typical growth of p-layers for LEDs in order to minimize the thermal load on the InGaN active regions. If the p-layer growth temperature is too high the InGaN layers can degrade structurally, causing fluctuations in the local In content ultimately leading to the formation of voids and In-rich clusters which significantly degrade device performance.[169] However, at low growth temperatures unintentional impurity incorporation can increase, resulting in further compensation of Mg acceptors and therefore even lower hole concentrations.[42,43] This problem is even more significant in the N-polar orientation, where additional care must be taken to avoid impurity incorporation.

In conventional III-V systems, delta (∂-) doping has been investigated as an alternative to continuous doping in order to carefully tune doping profiles[170] and to investigate novel band structure engineering through the introduction of localized sheets of charge.[171] In addition, ∂-doping has been shown to improve material quality and increase hole concentrations in wide-bandgap II-VI semiconductors such as ZnSe where p-doping is difficult to achieve.[172] There are also previous reports of Mg ∂-doping for p-type GaN[173–176] and AlGaN[177,178] films,

resulting in increased dopant densities and hole concentrations as well as superior crystalline quality compared to continuously-doped layers. These improvements have been attributed to a number of different factors, including a reduction in Mg activation energy, a reduction in Mg self-compensation,[175] and a reduction in surface defects (polarity inversion domains)[179] and dislocation densities.[173,177] These studies on GaN:Mg ∂-doping have all utilized the Ga-polar orientation, with no reports available on the properties of ∂-doped N-polar p-GaN films.

The rest of this chapter will focus on the growth of N-polar p-GaN layers using continuous and ∂-doping schemes towards maximizing the hole concentration and minimizing the p-layer resistivity and p-contact resistance. Additionally, the thermal activation of Mg acceptors after growth and the processing parameters for achieving low p-contact resistance will be discussed in detail.

7.1 Sample structure and processing for p-layer characterization

While the p-layers investigated in this work are designed for implementation into devices with InGaN active regions with high In contents, the samples discussed in this chapter did not contain InGaN tunneling layers so that the properties of the p-layers could be extracted without convolution from the InGaN layers. The p-layer stack in these samples consisted of a 10 nm thick p+ layer with [Mg]=1x10^{20} cm^{-3} adjacent to the n-GaN layer, followed by 350 nm p-GaN with lower doping (either continuous or ∂-doping), followed by a p+ cap layer for low contact resistance (Figure 7.1). While the devices presented in Chapter II utilized 60 nm thick p-layers, in this section the p-layer thickness was increased to 350 nm in order to ensure that parameters extracted were not influenced by the region near the p-n junction. Unless otherwise mentioned, NH_3 and TEGa flows of 6 slm and 4.6 μmol/min (corresponding R_g=0.73 Å/s),

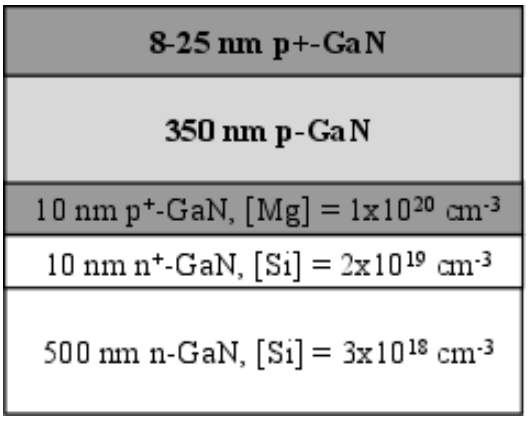

Figure 7.1. Layer structure used for p-layer characterization. Only the growth of the bulk p-layer and the p+ cap were varied, while the layers near the junction were kept constant throughout all samples.

respectively, were used throughout p-layer growth and a 12 nm thick p+ cap was used with a Mg flow of 33 nmol/min. High NH_3 flows aid in suppressing O and C incorporation during p-layer growth, as discussed in Chapter VI.

While specific variations in the fabrication parameters will be discussed later in this chapter, the standard process used is as follows: after growth, a 100 nm thick SiO_2 protection layer was deposited using PECVD then samples were annealed in a RTA in N_2 ambient at 800 °C for 5 min for Mg acceptor activation. Next, the SiO_2 was removed in buffered HF then p-TLM patterns were defined using conventional optical lithography techniques on a GCA 6300 stepper and 40/100 nm Ni/Au contacts were evaporated in an E-beam deposition chamber. After liftoff, samples were placed in the RTA at 400 °C for 5 min to anneal the p-contacts. TLM I-V measurements were then carried out using a semiconductor parameter analyzer.

7.2 Dynamic contact resistance for characterization of non-ohmic contacts

For all samples discussed in this section, the p-contacts were slightly non-ohmic at best, making it difficult to directly compare numerical results from p-TLM measurements. To account for this, a dynamic contact resistance extraction was performed for each sample after TLM measurements. This method was outlined in detail in Peter Kozodoy's thesis[180] and was used in all previous reports on N-polar p-GaN from UCSB,[82] allowing for a more direct comparison of the properties of samples in this chapter to previous results. This method begins by measuring I-V curves for each TLM pad spacing by sweeping the current from -1 to 1 μA. While traditional TLM analysis uses the resistance at 0 V to extract sheet and contact resistances, the dynamic extraction fits the resistance vs. TLM pad spacing for each current value measured. For contacts which are not ohmic, the contact resistance is higher at low voltages (low currents) and decreases for higher voltages (currents) where the I-V curves become more linear. For most samples, the dynamic contact resistance reaches a steady value above around 100 μA current, so in this work (and the previous work from UCSB) the reported contact resistances are measured at a current of 200 μA in a regime where the TLM I-V curves are close to linear. The sheet resistance of the p-layer is also extracted for each current value, but does not change significantly with respect to the current. For this reason, the sheet resistance (bulk resistivity) values reported herein are an average of the sheet resistances measured across the full current range. For many of the initial samples grown in this study prior to p-GaN optimization the dynamic TLM extractions were not well-behaved, resulting in widely varying results such that even in the linear region above 100 μA current it was not possible to extract meaningful parameters. These samples will not be discussed- rather, the

rest of this chapter will focus on samples which are already in a regime which is relatively well-behaved.

7.3 p-GaN fabrication process optimization

While many of the parameters involved in the post-growth processing of p-contacts were investigated, this section will focus on the three aspects which most strongly affected the electrical performance of the p-layers: Mg acceptor activation conditions, choice of contact metal scheme, and p-contact annealing. First, the effect of a SiO_2 protection layer during p-GaN activation was tested for four different annealing temperatures between 700-950 °C. All samples were processed from the same starting wafer, and all other processing parameters were kept constant. The electrical results for samples with and without the SiO_2 protective layer are shown in Figure 7.2.

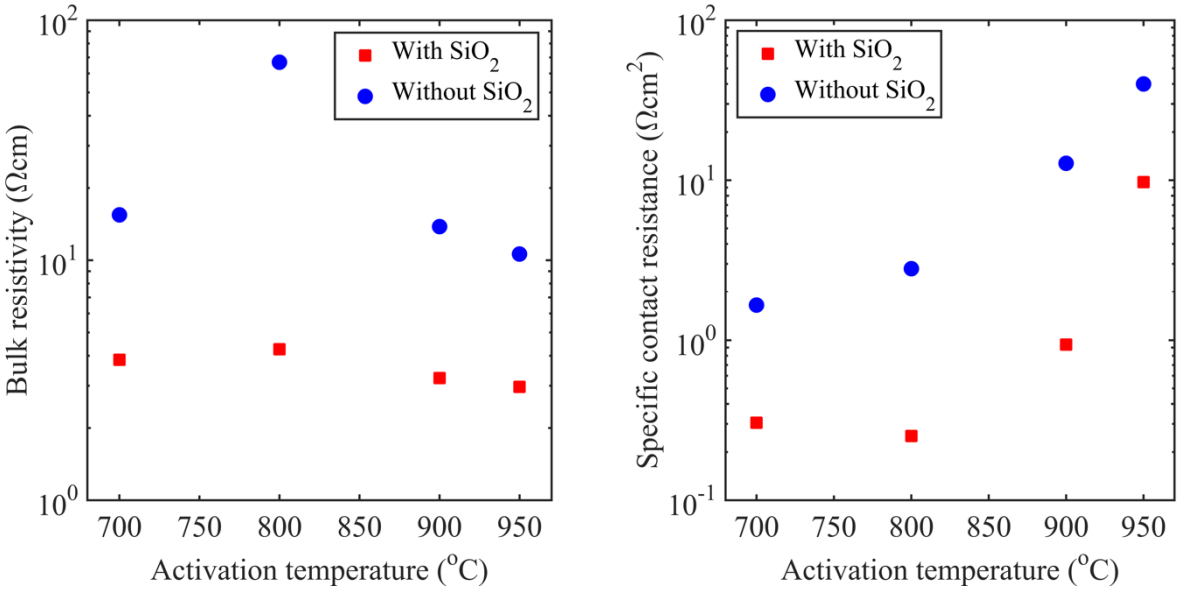

Figure 7.2. Effect of SiO_2 cap and p-GaN activation temperature on the bulk resistivity (left) and specific contact resistance (right) extracted from p-TLM measurements.

For all annealing temperatures, the samples with SiO_2 protective layers resulted in reduced resistivities and contact resistances around an order of magnitude lower than samples without SiO_2 layers. During the annealing process, it is possible that N-vacancies are formed at the surface of the p-layer, resulting in degradation of the electrical properties. When the SiO_2 protective layer is used, the formation of these vacancies is likely reduced or prevented entirely. In addition, when a full tunnel diode structure was fabricated which contained a 1.8 nm $In_{0.30}Ga_{0.70}N$ tunneling layer, the use of a SiO_2 layer during p-GaN activation resulted in an increase in the diode current of around an order of magnitude under both forward and reverse biases (not shown). While higher activation temperatures led to a slight reduction in the bulk resistivity, activation temperatures above 800 °C resulted in higher contact resistances. For these reasons, a temperature of 800 °C was used as the standard activation temperature and all samples were capped with SiO_2 prior to activation.

Most contacts to p-GaN layers consist of either Ni/Au or Pd/Au metal stacks which are often annealed after deposition to achieve lower contact resistances. While Pd/Au contacts are currently favored in general at UCSB and were used in the previous reports on N-polar p-GaN,[82] in this work Ni contacts resulted in lower contact resistances under all conditions tested. In multiple series of samples, 20/200 nm Pd/Au contacts were investigated along with 40/100 nm Ni/Au contacts, and as-deposited the two contact metals behaved similarly in p-TLM measurements and in full diode I-V measurements. Annealing experiments were performed at temperatures between 400-700 °C for 1-5 min on both Ni and Pd contacts, and in all cases the electrical properties of the Pd contacts degraded after annealing. The Ni contacts, however, were significantly improved after annealing at 400 °C for 5 min. For longer

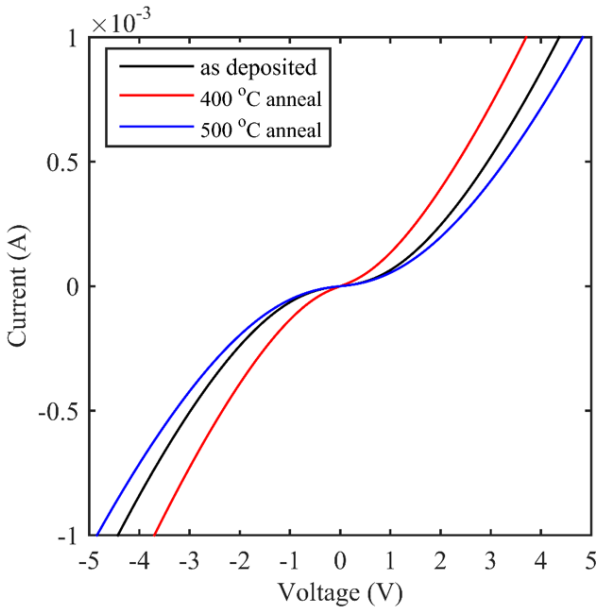

Figure 7.3. I-V curves for p-TLM pads separated by 2 μm before and after 5 min RTA annealing.

annealing times and higher temperatures, the contacts became less ohmic in nature and the resistance increased. Figure 7.3 shows the measured TLM I-V curve for a pad spacing of 1 μm for the Ni/Au contacts as deposited and after annealing at 400 and 500 °C. Overall, the most ohmic p-contacts were achieved using Ni/Au contacts annealed at 400 °C, though Pd contacts could potentially outperform Ni contacts if the Pd thickness or particularly the annealing conditions are further explored.

7.4 Mg doping experiments and injection schemes

Two different doping schemes were investigated for the bulk p-layer, including continuous doping and ∂-doping where each period consisted of Cp_2Mg injection in the absence of TEGa to saturate the surface with Mg, followed by the growth of 5-22 nm GaN using TEGa in the

absence of Cp_2Mg injection. In order to compare samples with different injection schemes, the total quantity of Mg injected (n_{Mg}) was defined as

$$n_{Mg} = F_{Mg} \times N \times t$$

where F_{Mg} is the Cp_2Mg molar flow in nmol/min, N is the number of ∂-doping periods, and t is the duration of Mg injection for each period in minutes. In the case of continuously doped samples (no ∂-doping), N=1 period and t=79.5 min, the time required for the deposition of 350 nm GaN at R_g=0.73 Å/s.

First, the effect of the ∂-doping period was investigated for four samples with the same n_{Mg} consisting of 1 minute Mg injection before each period. For layers with a smaller period thickness (higher N), F_{Mg} was reduced to achieve a constant n_{Mg}=1000 nmol for all samples (Table 7.1). The resulting bulk resitivities and specific contact resistances (ρ_c) are shown in Figure 7.4. Both the resistivity and contact resistance decreased as the ∂-doping period was reduced, despite the layers containing similar Mg doping levels according to SIMS (2.8-3.4x10^{19} cm^{-3}). If the unintentional carbon incorporation is simply proportional to the Mg flow used, it is possible that the layer with the thickest period which used the highest Mg flow resulted in somewhat higher carbon incorporation. Additionally, the use of a longer period may result in less uniform doping throughout the p-layer if the majority of Mg is incorporated

Table 7.1. ∂-doping parameters for period thickness series with constant n_{Mg}=1000 nmol.

Period thickness (nm)	***N***	***t* (min)**	***F_{Mg}* (nmol/min)**
5	70	1	14
10	35	1	30
15	23	1	45
22	16	1	65

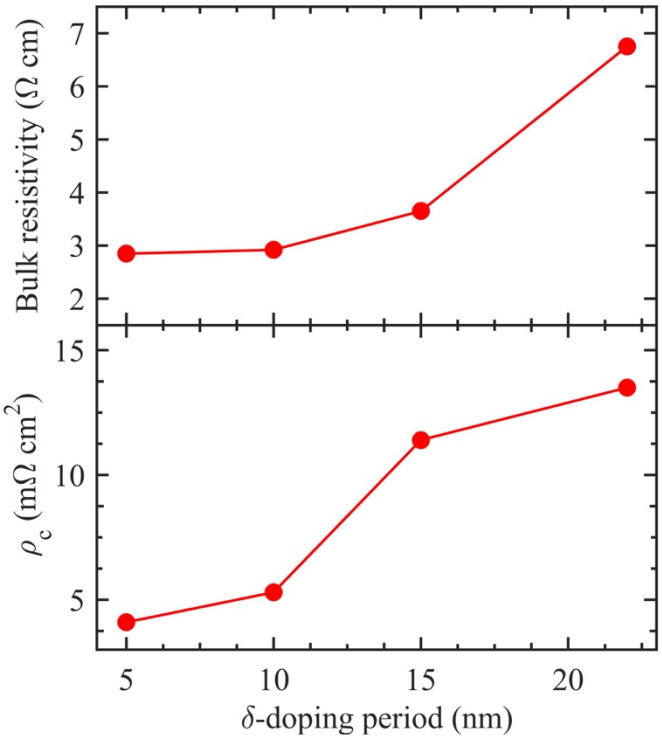

Figure 7.4. Effect of delta doping period on the bulk resistivity (top) and specific contact resistance (bottom) extracted from p-TLM measurements for samples with the same n_{Mg}=1000 nmol

.

at the beginning of each period, leading to decreasing Mg content for the duration of each period. In this case, the total Mg content could be similar in the layers but the local Mg content may vary more significantly as the period thickness is increased. While the Mg content was measured using SIMS for each sample in this series, the resolution of the SIMS tool (at UCSB) was not sufficient to resolve any fluctuation in the Mg doping even in the sample with a 22 nm period. Furthermore, the C and O levels have not been assessed using SIMS due to the high baseline above $1x10^{17}$ cm^{-3} in the UCSB SIMS system.

In addition to the ∂-doping period, the effect of varying F_{Mg} along with t was investigated in a series of three samples with the same n_{Mg}. Using a ∂-doping period of 15 nm, the Mg

Table 7.2. ∂-doping parameters for Mg injection time series with constant n_{Mg}.

Period thickness (nm)	***N***	***t* (min)**	F_{Mg} **(nmol/min)**
15	23	1	42
15	23	1.67	25
15	23	2.5	17

injection time for each period, t, was varied from 1 to 2.5 min and the Mg flow was correspondingly reduced for longer times such that n_{Mg}=960 nmol for all samples (Table 7.2). The electronic properties of these samples are presented in Figure 7.5. While the effect of varying the Mg injection time was less significant than varying the period thickness, the bulk resistivity decreased slightly as the Mg injection time was reduced. The Mg concentration measured in SIMS was around 1.5x10^{19} cm^{-3} for the sample with t=1 min, and increased to

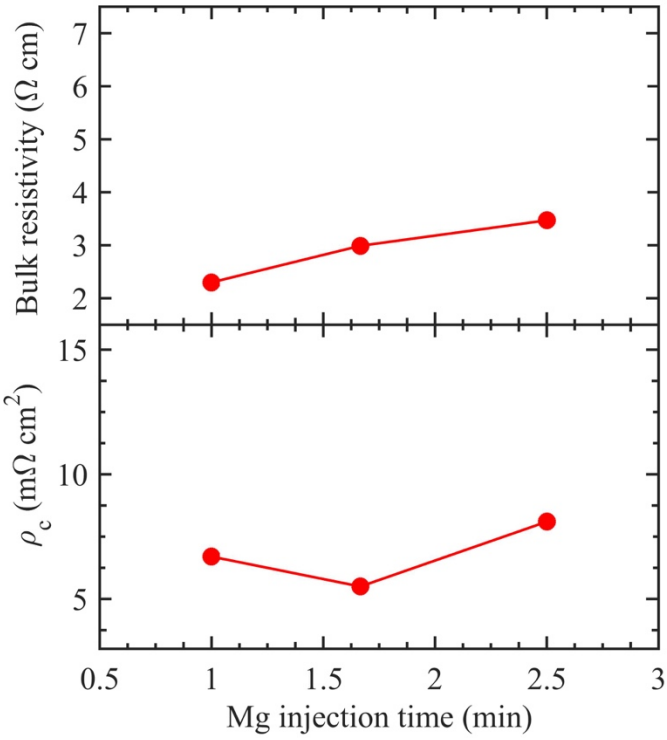

Figure 7.5. Effect of Mg injection time on the bulk resistivity (top) and specific contact resistance (bottom) extracted from p-TLM measurements.

$2.5x10^{19}$ cm^{-3} for the sample with t=2.5 min, which is likely the dominant factor affecting the bulk resistivity. The contact resistance decreased from around 8.5 to 5.5 $m\Omega cm^2$ when the Mg injection time was decreased from 2.5 to 1.67 min and increased slightly as the time was further reduced.

Finally, the effect of the p^+ contact layer doping and thickness were investigated in two series of samples. All samples contained a ∂-doped p-layer with a 5 nm period, t=1 min, and n_{Mg}=700 nmol with varying p^+-GaN caps. Figure 7.6 shows the dependence of the electrical properties on the p^+-cap growth parameters. As expected, the bulk resistivity did not vary

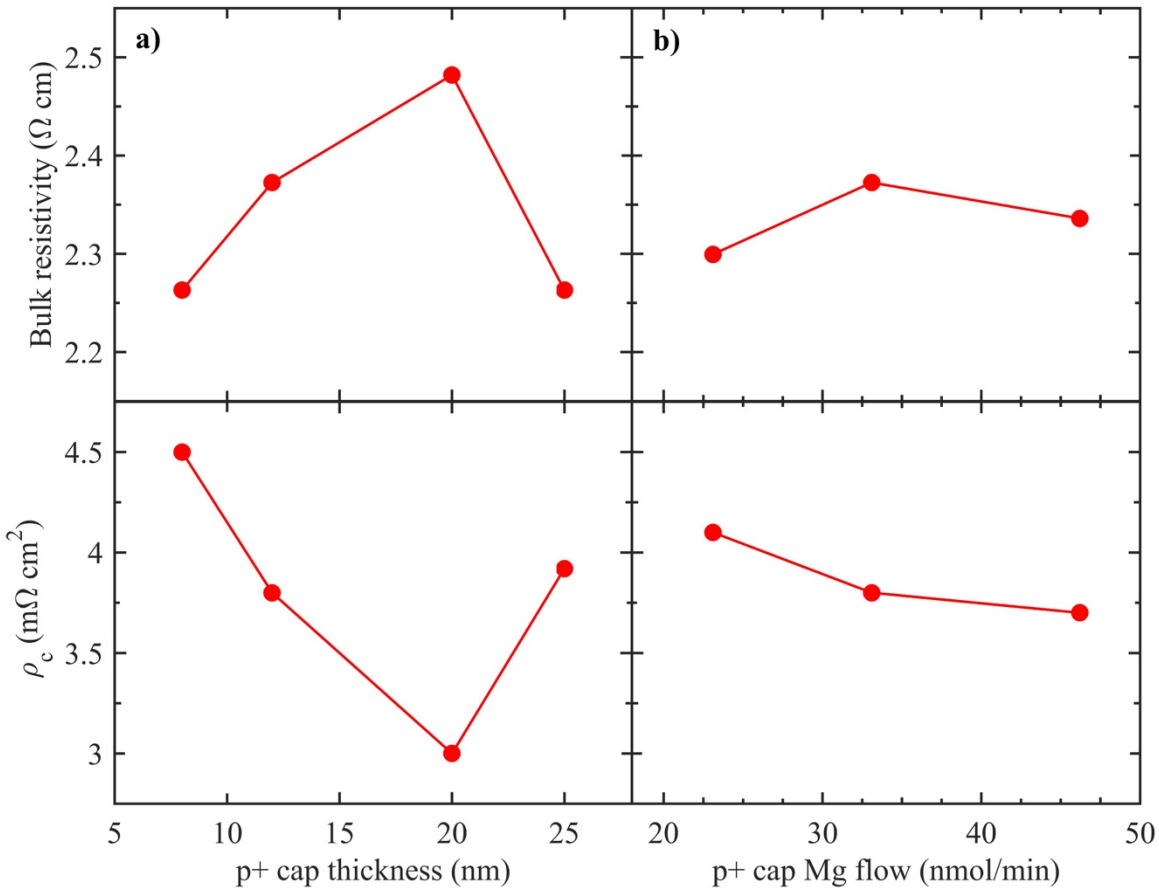

Figure 7.6. Effect of a) p+ cap thickness with a Mg flow of 23 nmol/min and b) p+ Mg flow with a thickness of 12 nm on the bulk resistivity (top) and specific contact resistance (bottom) extracted from p-TLM measurements.

strongly with either the p+ thickness or the Mg doping level in the p+ layer, ranging from 2.26 to 2.48 Ωcm. The specific contact resistance, however, was significantly affected by the p+ cap, decreasing from 4.5 to 3.0 mΩcm^2 as the thickness of the cap was increased from 8 to 20 nm, and increasing to 4.0 mΩcm^2 for a 25 nm cap. The contact resistance decreased slightly from 4.1 to 3.7 mΩcm^2 as the Mg flow in the cap layer was increased from 23 to 46 nmol/min. From these results, it became apparent that for p+ caps thinner than 20 nm the contacts were more strongly affected by the bulk p-layer properties, while the use of a 20 nm cap resulted in the lowest contact resistance. Once the cap thickness was increased to 20 nm, the contact resistance in each subsequent series of samples decreased and depended less strongly on the growth parameters used in the bulk p-layer.

7.5 Summary of electrical properties for ∂-doped and continuously doped layers

A summary of the electrical properties extracted for layers with different n_{Mg} using various doping schemes is presented in Figure 7.7. For each set of growth conditions discussed in the previous sections, the bulk resistivity decreased as n_{Mg} was decreased. This is in agreement with previous studies, where p-doping above around 2x10^{19} cm^{-3} typically leads to a reduction in hole concentration due to Mg acceptor self-compensation.[168] In addition, for each n_{Mg} where a continuously doped layer was grown, the resulting resistivity was lower than for any of the ∂-doping schemes (black triangles, Figure 7.7). The overall lowest bulk resistivity measured in this study was 1.83 Ωcm, achieved using a ∂-doped layer with a 5 nm period and a total Mg content of 470 nmol. The lowest reported resistivity value in the literature for N-polar p-GaN was 1.57 Ωcm,[82] only slightly lower than that achieved in this work. This is most likely due to the fact that in that study, the p-layer was grown at 1080 ºC, where unintentional impurity

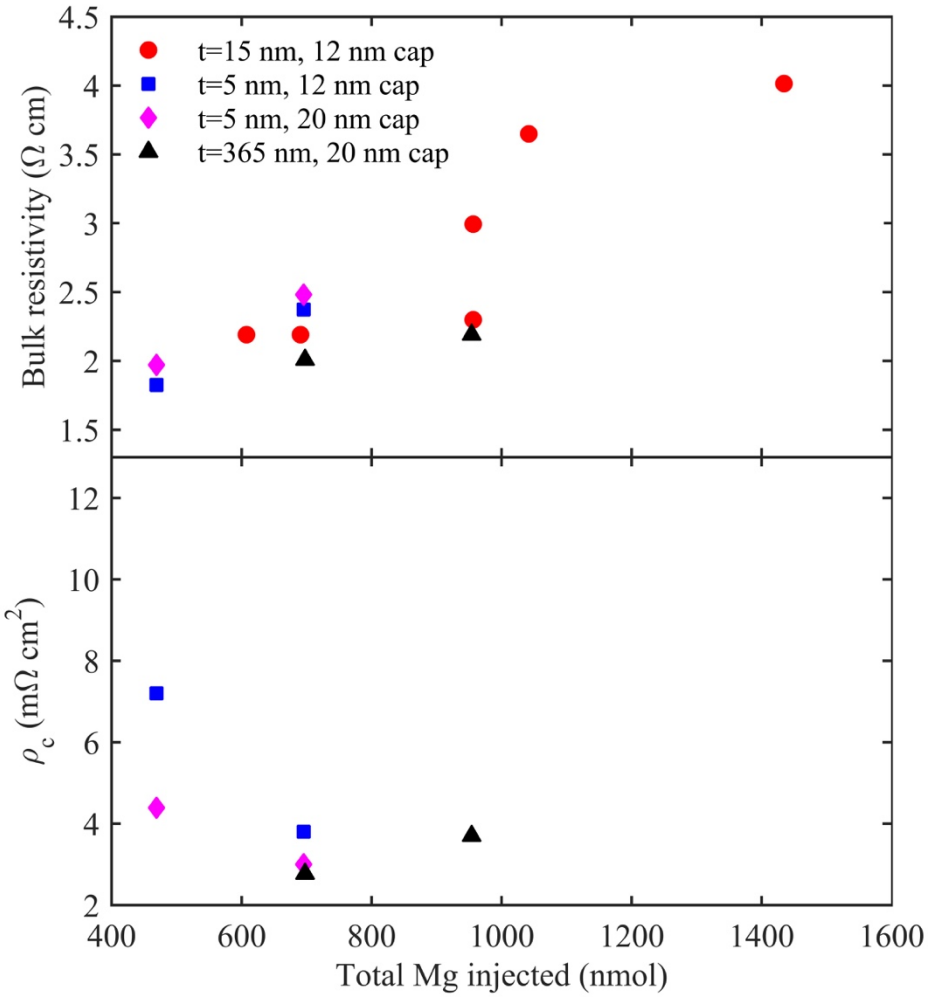

Figure 7.7. Dependence of the bulk resistivity (top) and specific contact resistance (bottom) on the total Mg injected for both ∂-doped and continuously doped samples.

incorporation is significantly reduced compared to growth at lower temperatures. It is likely that despite careful tuning of the growth parameters, the carbon and oxygen contents in this work were around 0.5-1x10^{17} cm^{-3}, resulting in partial compensation and ultimately leading to lower hole concentrations. However, as mentioned previously, the growth temperature in this study was limited to 900 ºC for applications in devices with high indium contents.

Although the p+ cap layer did not significantly affect the bulk resistivity, the thickness of the p+ cap was critical to achieving low contact resistances. When comparing the samples

with 5 nm ∂-doping periods (blue squares and magenta diamonds in Figure 7.7), the samples with the thicker cap layers resulted in the lowest contact resistances. For each Mg doping level tested, the lowest contact resistance was achieved using continuous doping rather than ∂-doping, with a minimum value of 2.77 mΩcm^2 for a continuously doped layer with n_{Mg}=700 nmol. To the best of our knowledge, this is the lowest reported contact resistance to N-polar p-GaN, where the lowest literature value was 10.3 mΩcm^2.[82] While layers with lower n_{Mg} resulted in lower bulk resistivities, the specific contact resistance increased as n_{Mg} was decreased from 700 to 470 nmol for ∂-doped samples with 5 nm periods with either 12 or 20 nm p+ caps. Overall, the optimum n_{Mg} was around 700 nmol to achieve a compromise between resistivity and contact resistance.

7.6 Conclusions

To summarize this chapter, ∂-doped and continuously doped N-polar p-GaN layers were deposited at low temperature to study the electrical properties of such layers. Numerous ∂-doping schemes were explored, including varying the period, Mg injection time, and total amount of Mg injected. Lower amounts of Mg and smaller ∂-doping periods resulted in the lowest bulk p-layer resistivities, while slightly higher Mg contents improved the specific contact resistance. The growth of p+ contact layers was also investigated, revealing that a cap thickness of 20 nm was critical for minimizing contact resistance. The post-growth activation of Mg acceptors also had a strong impact on the observed electrical properties, and a SiO_2 layer was beneficial in protecting the p-GaN surface during activation. Annealed Ni/Au contacts outperformed Pd/Au contacts, however it was not possible to achieve fully ohmic p-contacts. Despite the challenges involved, the bulk resistivities achieved in this study were

comparable to those in the literature and the contact resistance in this study was significantly lower than reports in the literature with a minimum value of 2.77 $m\Omega cm^2$ for a continuously doped layer.

VIII. Summary and Outlook

8.1 N-polar InGaN growth

The work presented in this thesis was designed to expand the toolbox of growth techniques which are available for the fabrication of any device which contains high indium mole fractions, with a focus on layers with indium compositions above 0.30. Chapter II provided a pathway towards growing N-polar InGaN heterostructures with indium compositions up to 0.46 by thoroughly investigating many aspects of the InGaN growth process as well as the subsequent GaN barrier growth process. In addition, the first demonstration of a MOCVD-grown N-polar tunnel diode containing a $In_{0.35}Ga_{0.65}N$ layer was presented along with the electrical properties of this device. While the composition of the InGaN well layers was most strongly affected by the deposition temperature and the gas phase indium content, there were many more subtle aspects which enabled the growth of layers with high indium contents. For example, the growth parameters used during the two-step barrier growth process was crucial for protecting InGaN well layers at low temperatures prior to growing smooth GaN barriers at elevated temperatures.

The InGaN films presented in Chapter II displayed room temperature photoluminescence with emission wavelengths up to 600 nm, a regime where nitride devices typically suffer from low quantum efficiency due to poor material quality. The area of N-polar optoelectronic devices is an exciting field for future research. As discussed in Section 2.4, the emission wavelengths for N-polar layers grown on vicinal substrates was significantly longer than for co-loaded Ga-polar layers despite containing similar amounts of indium. While it is highly

unlikely that N-polar devices will outperform Ga-polar devices in the blue region of the spectrum, in part due to the years of research that have gone into optimizing Ga-polar InGaN growth, the N-polar orientation may be advantageous for green-yellow emission where Ga-polar devices suffer from poor efficiency. In addition, the polarization fields in the N-polar orientation lead to a more favorable band structure for both emitters and solar cells compared to the Ga-polar orientation. Figure 8.1 shows the calculated energy band diagrams of a typical LED structure in both the Ga-polar and N-polar orientations. The electric field in the N-polar orientation reduces the junction depletion width, resulting in reduced barriers for carrier injection into the wells. In addition, under forward bias the electric field in the well layers is reduced, while in the Ga-polar orientation the electric field increases with forward bias, leading to carrier separation and reduced electron-hole wavefunction overlap.

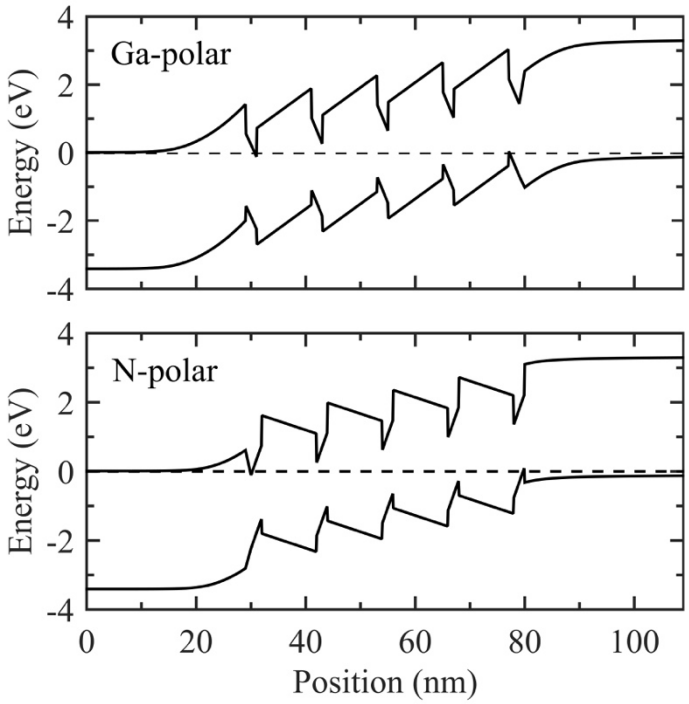

Figure 8.1. Calculated energy band diagrams for Ga-polar (top) and N-polar (bottom) LED structures consisting of 2 nm $In_{0.3}Ga_{0.7}N$ wells and 10 nm GaN barriers.

To optimize the performance of N-polar optoelectronic devices, additional investigations into the effects of local composition fluctuations on the emission properties of N-polar InGaN layers should be performed. If the formation of In-rich regions is assisted by two monolayer high surface steps, it would be interesting to investigate growth conditions which favor the formation of double surface steps, potentially using different miscut orientations as well. While higher miscut angles typically lead to a lower average indium composition, the surface step structure and local compositional fluctuations discussed in Chapter II will likely depend on which miscut angle and direction (towards GaN *a*- or *m*-direction) is used. The In-rich regions in such layers could result in efficient green or yellow emission, while also benefiting from increased confinement in these regions. The luminescence intensity from N-polar InGaN layers would also benefit from further reducing the carbon and oxygen impurity incorporation into these layers, possibly by using an alternative indium precursor such as triethyl indium (TEIn) for quantum well growth. These experiments have been planned for some time, but have been delayed due to issues with the precursor production.

8.2 N-polar InN growth

Chapter III outlined the first attempt at UCSB to grow N-polar InN layers on GaN using MOCVD. Due to the high lattice mismatch between InN and GaN, the layers relaxed through a combination of quantum dot formation and a step-mediated relaxation process resulting from the use of a vicinal substrate. Additionally, GaN/InN/GaN double heterostructures were successfully fabricated which consisted of nominally 1-5 nm thick InN layers embedded in GaN. The electrical properties of InN layers from 20-60 nm thick were also discussed, with a maximum Hall mobility of 706 cm^2/Vs measured for a 20 nm thick layer. This value is

significantly higher than previous reports on In-polar InN films grown by either MOCVD or MBE with similar thicknesses, indicating the high quality of these layers for applications in electronic devices.

The growth of N-polar InN on vicinal GaN presents many opportunities for future investigations. First, the optical properties of the InN quantum dots and thin films presented in Chapter III should be investigated in detail. Due to the lack of the necessary measurement setup at UCSB for IR emission, the optical properties were not yet assessed. Such studies would be useful to determine the extent of the carrier confinement that is expected to occur within the quantum dots. By changing the growth temperature, the density and size of the InN quantum dots could be controlled in order to tune the emission properties for long wavelength applications. Additionally, since the quantum dots were aligned along the step edges, it may be possible to produce ordered arrays of quantum dots or aligned InN nanowires which could be of interest for basic physics studies and electronic applications. As with the growth of N-polar InGaN layers, it would also be interesting to investigate the effect of the substrate miscut angle and direction on the ordering of the InN quantum dots. Since the steps arising from the vicinal substrate played a key role in the relaxation process, it is likely that widely varying morphologies could be achieved using different misorientations.

The optical and electronic performance of InN quantum dots and thin films could be further enhanced by using TEIn as the indium precursor to reduce carbon incorporation. Similar to TEGa, the ß-elimination of the ethyl radicals in TEIn leads to significantly lower carbon content.[164] Since the InN layers are grown at very low temperatures, it is difficult to avoid carbon contamination when using TMIn as the indium precursor (Chapter VI). For InN

thin films, such as those discussed in section 3.5, the electron mobility should increase as the impurity content is decreased due to a reduction in scattering processes, making these layers even more attractive for high frequency electronic device applications.

8.3 InGaN pseudo-substrates

Chapters IV and V presented two pathways for fabricating lattice-engineered InGaN substrates to reduce the compositional pulling effect, allowing for the regrowth of higher quality InGaN layers with increased indium compositions. In Chapter IV, the fabrication process for one dimensionally relaxed nanostripe arrays was discussed. In order to avoid defect formation during subsequent InGaN regrowth, it was critical that the height of the nanostripes be similar to the stripe width for elastic relaxation to occur. This system proved to be a useful tool for studying the relaxation behavior of nanopatterned layers and their applicability as lattice-matched substrates. Chapter V covered the use of relaxed PAMBE-grown InGaN pseudo-substrates, which proved to be somewhat more practical than the approach in Chapter IV for the regrowth of InGaN layers using MOCVD. The regrowth of thick N-polar InGaN layers on N-polar InGaN pseudo-substrates was presented, including a novel digital epitaxy scheme which allowed for the deposition of smooth layers with intermediate indium compositions around 0.11 which were lattice-matched to the InGaN PSs. The same N-polar InGaN PSs were used for the fabrication of MQW structures, and Ga-polar MQWs were regrown on Ga-polar InGaN PSs. For both orientations of MQW samples as well as for the thick N-polar InGaN layers, the use of the lattice-matched substrates resulted in a reduction of the compositional pulling effect as evidenced by a significant redshift in the PL emission wavelengths compared to co-loaded layers deposited on traditional GaN base layers.

While the layers discussed in Chapter IV contained relatively low amounts of indium, the results serve as a proof-of-concept and provide a starting point for growing layers with higher indium compositions on InGaN pseudo-substrates. By combining the use of N-polar InGaN PSs with the techniques discussed in Chapter II for the growth of InGaN quantum wells, it should be possible to grow InGaN active regions with compositions above 0.5. Additionally, using the InGaN PSs should allow higher growth temperatures and longer emission wavelengths for a given indium composition.[9]

To fabricate devices using the InGaN PSs, the growth of n-InGaN and p-InGaN layers will also need to be investigated. The use of a full InGaN structure (no GaN) is necessary to maximize the benefits gained from the use of the InGaN PS. In the case of the tunnel diode structure discussed in Chapter II, a full InGaN structure would likely lead to increased

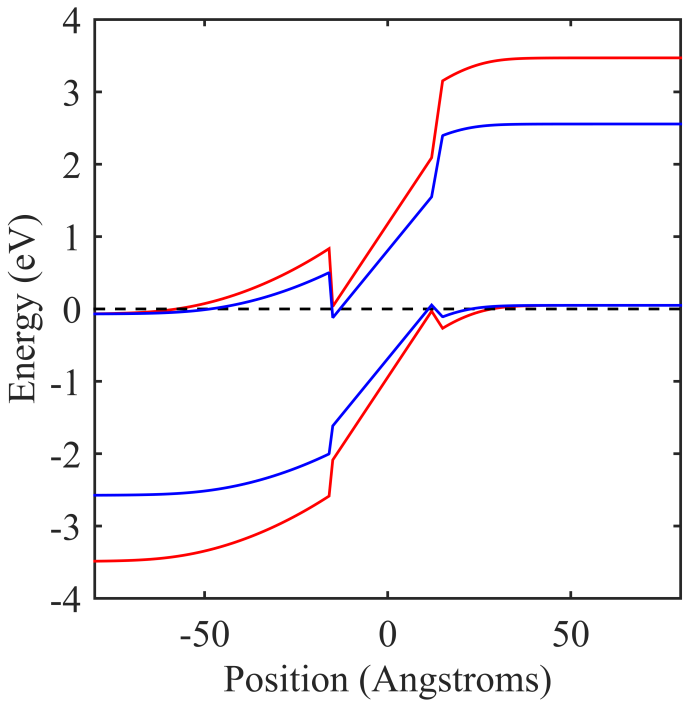

Figure 8.2. Calculated energy band diagrams for a GaN/$In_{0.3}Ga_{0.7}N$/GaN tunnel diode (red) and a $In_{0.2}Ga_{0.8}N$/$In_{0.5}Ga_{0.5}N$/$In_{0.2}Ga_{0.8}N$ tunnel diode (blue).

tunneling currents. Figure 8.2 shows the calculated band diagrams of a GaN/$In_{0.3}Ga_{0.7}N$/GaN structure as well as a $In_{0.2}Ga_{0.8}N/In_{0.5}Ga_{0.5}N/In_{0.2}Ga_{0.8}N$ structure. In both cases, the lattice mismatch between the InGaN tunneling layer and the n- and p-layers was chosen to be less than 3%. The full InGaN structure results in reduced barriers on the n- and p-sides of the junction as well as increased 2DEG and 2DHG densities, and the tunneling probability is enhanced when tunneling through a lower bandgap material. One attempt was made to fabricate a tunnel diode device on the N-polar InGaN PS, however the leakage current was very high compared to samples grown on GaN templates. Further optimization of the full layer structure including the n- and p-InGaN layers could enable the fabrication of tunnel diodes with higher indium content tunneling layers, resulting in improved electrical performance.

8.4 Device fabrication and p-layer growth

Chapter VI discussed techniques for suppressing unintentional carbon and oxygen incorporation into N-polar layers deposited at low temperatures. While it is commonly believed that the impurity incorporation in N-polar films is too high for the fabrication of high quality devices, this chapter illustrates that with the correct choice of precursor flows it is possible to grow N-polar GaN layers with carbon and oxygen contents of 2 and 3 x 10^{16} cm^{-3}, respectively, even at growth temperatures as low as 800 ºC. These results are important for the fabrication of any low temperature N-polar layers, particularly for InGaN or InN layers and p-layers grown on top of low temperature InGaN layers.

Finally, the growth of N-polar p-GaN at low temperatures was investigated in Chapter VII. When growing p-layers on top of InGaN layers with high indium contents, the temperature must be lower than the optimal p-GaN growth temperature to avoid damaging the

InGaN active regions. Although the growth conditions were carefully chosen to avoid impurity incorporation, films with Mg doping suffer from increased C and O content compared to films grown using only TEGa, especially at low temperatures, as discussed in Chapter VI. As an attempt to decrease the impurity content, ∂-doped p-layers were fabricated as well as continuously doped layers. Various parameters of the ∂-doping scheme were investigated, along with the growth of p+ contact layers. Post growth thermal annealing and p-contact fabrication were also discussed briefly, and were crucial in minimizing the p-layer resistivity and p-contact resistance. A minimum bulk resistivity of 1.83 Ωcm was achieved using a ∂-doped p-layer, and a minimum contact resistance of 2.77 Ωcm^2 was achieved using a continuously doped layer, significantly lower than previous reports on N-polar p-contacts.

While the work presented in this thesis represents significant progress in the area of low temperature N-polar p-GaN growth, it was not possible to fabricate fully ohmic p-contacts and the lowest contact resistances achieved were still around an order of magnitude higher

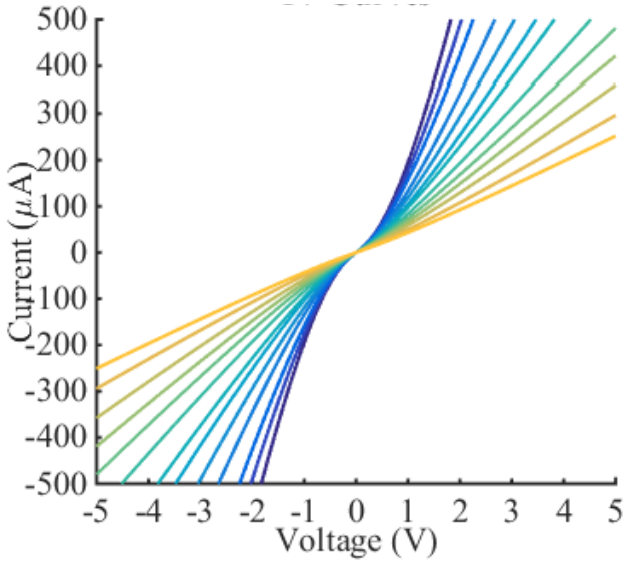

Figure 8.3. p-TLM I-V curves for all pad spacings from 1 to 25 μm for the sample containing a 350 nm thick continuously doped p-layer with n_{Mg}=700 nmol which was the closest to ohmic behavior.

than those typically seen in Ga-polar p-GaN with optimized processes. Figure 8.3 shows the TLM I-V curves for all pad spacings between 1 and 25 μm for the sample which was closest to ohmic behavior. Under low applied biases (in the regime where the tunnel diode is designed to operate), the p-contacts were more resistive than at higher voltages. Additional temperature-dependent p-TLM measurements were carried out by Prof. Patrick Fay's group at the University of Notre Dame, and indicated that the overall current in processed tunnel diode and tunnel FET devices at low biases is likely limited by the performance of the p-contacts.

To further improve the quality of N-polar p-GaN and p-contacts, there are many parameters which will need to be carefully investigated in both the growth and fabrication processes. First, the majority of the p-layers discussed in Chapter 7 contained a 12 nm p+ contact layer, although it was later determined that a thicker p+ layer significantly reduces the contact resistance. Selected delta-doped and continuously doped samples should be repeated with the improved contact layer scheme and will likely result in immediate improvement. Next, Pd/Au contacts may result in lower contact resistances if the metal thickness and contact annealing conditions are revisited. The thickness of each p-layer in the tunnel diode structure could also be further optimized, leading to reduced layer resistivities. Although the contact resistances typically seen in state-of-the-art Ga-polar devices are around an order of magnitude lower than those in this study, many years of research have gone into the optimization of Ga-polar p-layers and contacts for LED applications. Since there are very few studies on N-polar p-GaN or p-contacts, there are likely many different approaches which will allow for significant improvement in the performance of N-polar devices in the near future.

References

[1] S. Nakamura, M. Senoh, N. Iwasa, and S. Nagahama, Jpn. J. Appl. Phys. **34**, L797 (1995).

[2] M.S. Shur and M.A. Khan, MRS Bull. **22**, 44 (1997).

[3] S.C. Jain, M. Willander, J. Narayan, and R. Van Overstraeten, J. Appl. Phys. **87**, 965 (2000).

[4] Y.-F. Wu, D. Kapolnek, J.P. Ibbetson, P. Parikh, B.P. Keller, and U.K. Mishra, IEEE Trans. Electron Devices **48**, 586 (2001).

[5] W. Li, S. Sharmin, H. Ilatikhameneh, R. Rahman, Y. Lu, J. Wang, X. Yan, A. Seabaugh, G. Klimeck, D. Jena, and P. Fay, IEEE J. Explor. Solid-State Comput. Devices Circuits **1**, 28 (2015).

[6] T. Langer, A. Kruse, F.A. Ketzer, A. Schwiegel, L. Hoffmann, H. Jönen, H. Bremers, U. Rossow, and A. Hangleiter, Phys. Status Solidi C **8**, 2170 (2011).

[7] M.J. Reed, N.A. El-Masry, C.A. Parker, J.C. Roberts, and S.M. Bedair, Appl. Phys. Lett. **77**, 4121 (2000).

[8] P. Perlin, C. Kisielowski, V. Iota, B.A. Weinstein, L. Mattos, N.A. Shapiro, J. Kruger, E.R. Weber, and J. Yang, Appl. Phys. Lett. **73**, 2778 (1998).

[9] T.K. Sharma and E. Towe, J. Appl. Phys. **107**, 24516 (2010).

[10] T. Matsuoka, N. Yoshimoto, T. Sasaki, and A. Katsui, J. Electron. Mater. **21**, 157 (1992).

[11] H.K. Cho, J.Y. Lee, G.M. Yang, and C.S. Kim, Appl. Phys. Lett. **79**, 215 (2001).

[12] D.D. Koleske, A.E. Wickenden, R.L. Henry, and M.E. Twigg, J. Cryst. Growth **242**, 55 (2002).

[13] G.B. Stringfellow, J. Cryst. Growth **312**, 735 (2010).

[14] T. Yayama, Y. Kangawa, K. Kakimoto, and A. Koukitu, Phys. Status Solidi C **7**, 2249 (2010).

[15] M. V. Durnev, A. V. Omelchenko, E. V. Yakovlev, I.Y. Evstratov, and S.Y. Karpov, Phys. Status Solidi A **208**, 2671 (2011).

[16] S.F. Chichibu, A.C. Abare, M.S. Minsky, S. Keller, S.B. Fleischer, J.E. Bowers, E. Hu, U.K. Mishra, L.A. Coldren, S.P. DenBaars, and T. Sota, Appl. Phys. Lett. **73**, 2006 (1998).

[17] A. Yoshikawa, S.B. Che, W. Yamaguchi, H. Saito, X.Q. Wang, Y. Ishitani, and E.S. Hwang, Appl. Phys. Lett. **90**, 73101 (2007).

[18] T. Suski, T. Schulz, M. Albrecht, X.Q. Wang, I. Gorczyca, K. Skrobas, N.E. Christensen, and A. Svane, Appl. Phys. Lett. **104**, 182103 (2014).

[19] C. Chèze, F. Feix, M. Anikeeva, T. Schulz, M. Albrecht, H. Riechert, O. Brandt, and R. Calarco, Appl. Phys. Lett. **110**, 72104 (2017).

[20] T. Wernicke, L. Schade, C. Netzel, J. Rass, V. Hoffmann, S. Ploch, A. Knauer, M. Weyers, U. Schwarz, and M. Kneissl, Semicond. Sci. Technol. **27**, 24014 (2012).

[21] A. Tyagi, H. Zhong, N.N. Fellows, M. Iza, J.S. Speck, S.P. DenBaars, and S. Nakamura, Jpn. J. Appl. Phys. **46**, L129 (2007).

[22] M. Funato, M. Ueda, Y. Kawakami, Y. Narukawa, T. Kosugi, M. Takahashi, and T. Mukai, Jpn. J. Appl. Phys. **45**, L659 (2006).

[23] S. Keller, N.A. Fichtenbaum, M. Furukawa, J.S. Speck, S.P. DenBaars, and U.K. Mishra, Appl. Phys. Lett. **90**, 191908 (2007).

[24] D.N. Nath, E. Gür, S.A. Ringel, and S. Rajan, Appl. Phys. Lett. **97**, 71903 (2010).

[25] Z.Y. Al Balushi and J.M. Redwing, Appl. Phys. Lett. **110**, 22101 (2017).

[26] M. Stutzmann, O. Ambacher, M. Eickhoff, U. Karrer, A. Lima Pimenta, R. Neuberger, J. Schalwig, R. Dimitrov, P.J. Schuck, and R.D. Grober, Phys. Status Solidi B **228**, 505 (2001).

[27] S. Keller, H. Li, M. Laurent, Y. Hu, N. Pfaff, J. Lu, D.F. Brown, N.A. Fichtenbaum, J.S. Speck, S.P. DenBaars, and U.K. Mishra, Semicond. Sci. Technol. **29**, 113001 (2014).

[28] R. Dimitrov, M. Murphy, J. Smart, W. Schaff, J.R. Shealy, L.F. Eastman, O. Ambacher, and M. Stutzmann, J. Appl. Phys. **87**, 3375 (2000).

[29] O. Ambacher, M. Eickhoff, A. Link, M. Hermann, M. Stutzmann, F. Bernardini, V. Fiorentini, Y. Smorchkova, J. Speck, U. Mishra, W. Schaff, V. Tilak, and L.F. Eastman, Phys. Status Solidi C **0**, 1878 (2003).

[30] S. Rajan, M. Wong, Y. Fu, F. Wu, J.S. Speck, and U.K. Mishra, Jpn. J. Appl. Phys. **44**, L1478 (2005).

[31] M.H. Wong, S. Keller, N. Dasgupta, D.J. Denninghoff, S. Kolluri, D.F. Brown, J. Lu, N.A. Fichtenbaum, E. Ahmadi, U. Singisetti, A. Chini, S. Rajan, S.P. DenBaars, J.S. Speck, and U.K. Mishra, Semicond. Sci. Technol. **28**, 74009 (2013).

[32] S.Y. Karpov, K.A. Bulashevich, I.A. Zhmakin, M.O. Nestoklon, V.F. Mymrin, and Y.N. Makarov, Phys. Status Solidi B **241**, 2668 (2004).

[33] S.-H. Yen, Y.-K. Kuo, M.-L. Tsai, and T.-C. Hsu, Appl. Phys. Lett. **91**, 201118 (2007).

[34] M.L. Reed, E.D. Readinger, H. Shen, M. Wraback, A. Syrkin, A. Usikov, O. V. Kovalenkov, and V.A. Dmitriev, Appl. Phys. Lett. **93**, 133505 (2008).

[35] J. Verma, J. Simon, V. Protasenko, T. Kosel, H. Grace Xing, and D. Jena, Appl. Phys. Lett. **99**, 171104 (2011).

[36] K. Shojiki, T. Tanikawa, J. Choi, S. Kuboya, T. Hanada, R. Katayama, and T. Matsuoka, Appl. Phys. Express **8**, 61005 (2015).

[37] M. Eickhoff, J. Schalwig, G. Steinhoff, O. Weidemann, L. Görgens, R. Neuberger, M. Hermann, B. Baur, G. Müller, O. Ambacher, and M. Stutzmann, Phys. Status Solidi C **0**, 1908 (2003).

[38] Y.-L. Wang, F. Ren, U. Zhang, Q. Sun, C.D. Yerino, T.S. Ko, Y.S. Cho, I.H. Lee, J. Han, and S.J. Pearton, Appl. Phys. Lett. **94**, 212108 (2009).

[39] Z.Q. Li, M. Lestradet, Y.G. Xiao, and S. Li, Phys. Status Solidi A **208**, 928 (2011).

[40] S. Keller, N.A. Fichtenbaum, F. Wu, D. Brown, A. Rosales, S.P. Denbaars, J.S. Speck, and U.K. Mishra, J. Appl. Phys. **102**, 83546 (2007).

[41] S. Keller, H. Li, M. Laurent, Y. Hu, N. Pfaff, J. Lu, D.F. Brown, N. a Fichtenbaum, J.S. Speck, S.P. Denbaars, and U.K. Mishra, Semicond. Sci. Technol. **29**, 113001 (2014).

[42] N.A.A. Fichtenbaum, T.E.E. Mates, S. Keller, S.P.P. DenBaars, and U.K.K. Mishra, J. Cryst. Growth **310**, 1124 (2008).

[43] S.C. Cruz, S. Keller, T.E. Mates, U.K. Mishra, and S.P. DenBaars, J. Cryst. Growth **311**, 3817 (2009).

[44] C. Lund, S. Nakamura, S.P. DenBaars, U.K. Mishra, and S. Keller, J. Cryst. Growth **464**, 127 (2017).

[45] S. Krishnamoorthy, D.N. Nath, F. Akyol, P.S. Park, M. Esposto, and S. Rajan, Appl. Phys. Lett. **97**, 203502 (2010).

[46] S. Krishnamoorthy, P.S. Park, and S. Rajan, Appl. Phys. Lett. **99**, 233504 (2011).

[47] S. Krishnamoorthy, F. Akyol, P.S. Park, and S. Rajan, Appl. Phys. Lett. **102**, 113503 (2013).

[48] X. Yan, W. Li, S.M. Islam, K. Pourang, H. (Grace) Xing, P. Fay, and D. Jena, Appl. Phys. Lett. **107**, 163504 (2015).

[49] L. Esaki, Phys. Rev. **109**, 603 (1958).

[50] N. Jin, S.-Y. Chung, A.T. Rice, P.R. Berger, R. Yu, P.E. Thompson, and R. Lake, Appl. Phys. Lett. **83**, 3308 (2003).

[51] R.R. King, D.C. Law, K.M. Edmondson, C.M. Fetzer, G.S. Kinsey, H. Yoon, R.A. Sherif, and N.H. Karam, Appl. Phys. Lett. **90**, 183516 (2007).

[52] F. Bernardini, V. Fiorentini, and D. Vanderbilt, Phys. Rev. B **56**, 4 (1997).

[53] C. Wetzel, T. Takeuchi, H. Amano, and I. Akasaki, J. Appl. Phys. **85**, 3786 (1999).

[54] M. Grundmann and U. Mishra, Phys. Status Solidi C **4**, 2830 (2007).

[55] J. Simon, Z. Zhang, K. Goodman, H. Xing, T. Kosel, P. Fay, and D. Jena, Phys. Rev. Lett. **103**, 26801 (2009).

[56] M.F. Schubert, Phys. Rev. B **81**, 35303 (2010).

[57] M. Grundmann, (n.d.).

[58] E.L. Piner, M.K. Behbehani, N. a El-Masry, F.G. McIntosh, J.C. Roberts, K.S. Boutros, and S.M. Bedair, Appl. Phys. Lett. **70**, 461 (1997).

[59] S. Keller and S.P. DenBaars, J. Cryst. Growth **248**, 479 (2003).

[60] R.A. Oliver, M.J. Kappers, C.J. Humphreys, and G.A.D. Briggs, J. Cryst. Growth **272**, 393 (2004).

[61] S. Keller, S. Heikman, I. Ben-Yaacov, L. Shen, S.P. DenBaars, and U.K. Mishra, Appl. Phys. Lett. **79**, 3449 (2001).

[62] F. Jiang, R.-V. Wang, A. Munkholm, S.K. Streiffer, G.B. Stephenson, P.H. Fuoss, K. Latifi, and C. Thompson, Appl. Phys. Lett. **89**, 161915 (2006).

[63] J.-W. Ju, E.-S. Kang, H.-S. Kim, L.-W. Jang, H.-K. Ahn, J.-W. Jeon, I.-H. Leea, and J.H. Baek, J. Appl. Phys. **102**, 53519 (2007).

[64] D. Queren, M. Schillgalies, A. Avramescu, G. Brüderl, A. Laubsch, S. Lutgen, and U. Strauß, J. Cryst. Growth **311**, 2933 (2009).

[65] Y.-L. Hu, R.M. Farrell, C.J. Neufeld, M. Iza, S.C. Cruz, N. Pfaff, D. Simeonov, S. Keller, S. Nakamura, S.P. DenBaars, U.K. Mishra, and J.S. Speck, Appl. Phys. Lett. **100**, 161101

(2012).

[66] F.C.P. Massabuau, M.J. Davies, W.E. Blenkhorn, S. Hammersley, M.J. Kappers, C.J. Humphreys, P. Dawson, and R.A. Oliver, Phys. Status Solidi B **252**, 928 (2015).

[67] S.T. Pendlebury, P.J. Parbrook, D.J. Mowbray, D.A. Wood, and K.B. Lee, J. Cryst. Growth **307**, 363 (2007).

[68] S.J. Leem, Y.C. Shin, E.H. Kim, C.M. Kim, B.G. Lee, Y. Moon, I.H. Lee, and T.G. Kim, Semicond. Sci. Technol. **23**, 125039 (2008).

[69] H. Masui, S. Keller, N. Fellows, N.A. Fichtenbaum, M. Furukawa, S. Nakamura, U.K. Mishra, and S.P. DenBaars, Jpn. J. Appl. Phys. **48**, 71003 (2009).

[70] C. Wetzel, T. Suski, J.W. Ager III, E.R. Weber, E.E. Haller, S. Fischer, B.K. Meyer, R.J. Molnar, and P. Perlin, Phys. Rev. Lett. **78**, 3923 (1997).

[71] C.H. Seager, A.F. Wright, J. Yu, W. Götz, and W. Götz, J. Appl. Phys. **92**, 6553 (2002).

[72] J.L. Lyons, A. Janotti, and C.G. Van de Walle, Appl. Phys. Lett. **97**, 152108 (2010).

[73] J. Neugebauer and C.G. Van de Walle, Appl. Phys. Lett. **69**, 503 (1996).

[74] C.G. Van de Walle and J. Neugebauer, J. Appl. Phys. **95**, 3851 (2004).

[75] F. Tuomisto and I. Makkonen, Rev. Mod. Phys. **85**, 1583 (2013).

[76] G.B. Stringfellow, *Organometallic Vapor-Phase Epitaxy : Theory and Practice* (Academic Press, 1999).

[77] M.H. Xie, S.M. Seutter, W.K. Zhu, L.X. Zheng, H. Wu, and S.Y. Tong, **29**, (1999).

[78] C.-H. Lin, T. Akasaka, and H. Yamamoto, Appl. Phys. Express **6**, 35503 (2013).

[79] S. Nakamura, Science (80-.). **281**, 956 (1998).

[80] J.T. Griffiths, F. Oehler, F. Tang, S. Zhang, W.Y. Fu, T. Zhu, S.D. Findlay, C. Zheng, J. Etheridge, T.L. Martin, P.A.J. Bagot, M.P. Moody, D. Sutherland, P. Dawson, M.J. Kappers, C.J. Humphreys, and R.A. Oliver, J. Appl. Phys. **119**, 175703 (2016).

[81] F. Akyol, S. Krishnamoorthy, Y. Zhang, J. Johnson, J. Hwang, and S. Rajan, Appl. Phys. Lett. **108**, 131103 (2016).

[82] N.A. Fichtenbaum, C. Schaake, T.E. Mates, C. Cobb, S. Keller, S.P. DenBaars, and U.K. Mishra, Appl. Phys. Lett. **91**, 172105 (2007).

[83] G. Pettinari, A. Polimeni, M. Capizzi, J.H. Blokland, P.C.M. Christianen, J.C. Maan, V. Lebedev, V. Cimalla, and O. Ambacher, Phys. Rev. B **79**, 165207 (2009).

[84] V.M. Polyakov and F. Schwierz, Appl. Phys. Lett. **88**, 32101 (2006).

[85] J. Wu, W. Walukiewicz, K.M. Yu, W. Shan, J.W. Ager, E.E. Haller, H. Lu, W.J. Schaff, W.K. Metzger, and S. Kurtz, J. Appl. Phys. **94**, 6477 (2003).

[86] E. Trybus, G. Namkoong, W. Henderson, S. Burnham, W.A. Doolittle, M. Cheung, and A. Cartwright, J. Cryst. Growth **288**, 218 (2006).

[87] T.B. Fehlberg, G. a. Umana-Membreno, B.D. Nener, G. Parish, C.S. Gallinat, G. Koblmüller, S. Rajan, S. Bernardis, and J.S. Speck, Jpn. J. Appl. Phys. **45**, L1090 (2006).

[88] N. Khan, A. Sedhain, J. Li, J.Y. Lin, and H.X. Jiang, Appl. Phys. Lett. **92**, 172101 (2008).

[89] D.C. Look, H. Lu, W.J. Schaff, J. Jasinski, and Z. Liliental-Weber, Appl. Phys. Lett. **80**, 258 (2002).

[90] A. Janotti and C.G. Van de Walle, Appl. Phys. Lett. **92**, 32104 (2008).

[91] S. Ruffenach, M. Moret, O. Briot, and B. Gil, Phys. Status Solidi A **207**, 9 (2010).

[92] S. Keller, I. Ben-Yaacov, S.P. DenBaars, and U.K. Mishra, Proc. Int. Work. Nitride Semicond. Nagoya, Japan, Inst. Pure Appl. Phys. Conf. Ser. **1**, 233 (2000).

[93] S.-B. Che, W. Terashima, Y. Ishitani, A. Yoshikawa, T. Matsuda, H. Ishii, and S. Yoshida, Appl. Phys. Lett. **86**, 261903 (2005).

[94] A. Yoshikawa, K. Kusakabe, N. Hashimoto, E.S. Hwang, and T. Itoi, Appl. Phys. Lett. **108**, 22108 (2016).

[95] K. Kusakabe, N. Hashimoto, T. Itoi, K. Wang, D. Imai, and A. Yoshikawa, Appl. Phys. Lett. **108**, 152107 (2016).

[96] T. Schulz, A. Duff, T. Remmele, M. Korytov, T. Markurt, M. Albrecht, L. Lymperakis, J. Neugebauer, C. Chèze, and C. Skierbiszewski, J. Appl. Phys. **115**, 33113 (2014).

[97] C. Chèze, F. Feix, M. Anikeeva, T. Schulz, M. Albrecht, H. Riechert, O. Brandt, and R. Calarco, Appl. Phys. Lett. **110**, 72104 (2017).

[98] F. Matsuda, Y. Saito, T. Muramatsu, T. Yamaguchi, Y. Matsuo, A. Koukitu, T. Araki, and Y. Nanishi, Phys. Status Solidi C **0**, 2810 (2003).

[99] K. Xu and A. Yoshikawa, Appl. Phys. Lett. **83**, 251 (2003).

[100] G. Koblmüller, C.S. Gallinat, S. Bernardis, J.S. Speck, G.D. Chern, E.D. Readinger, H. Shen, and M. Wraback, Appl. Phys. Lett. **89**, 71902 (2006).

[101] J. Kuzmík, Š. Haščík, M. Kučera, R. Kúdela, E. Dobročka, A. Adikimenakis, M. Mičušík, M. Gregor, A. Plecenik, and A. Georgakilas, Appl. Phys. Lett. **107**, 191605 (2015).

[102] T. Matsuoka, H. Okamoto, H. Takahata, T. Mitate, S. Mizuno, Y. Uchiyama, and T. Makimoto, J. Cryst. Growth **269**, 139 (2004).

[103] T. Mitate, S. Mizuno, H. Takahata, R. Kakegawa, T. Matsuoka, and N. Kuwano, Appl. Phys. Lett. **86**, 134103 (2005).

[104] A. Jain, X. Weng, S. Raghavan, B.L. VanMil, T. Myers, and J.M. Redwing, J. Appl. Phys. **104**, 53112 (2008).

[105] T. Iwabuchi, Y. Liu, T. Kimura, Y. Zhang, K. Prasertsuk, H. Watanabe, N. Usami, R. Katayama, and T. Matsuoka, Jpn. J. Appl. Phys. **51**, 04DH02 (2012).

[106] C. Lund, B. Romanczyk, M. Catalano, Q. Wang, W. Li, D. DiGiovanni, M.J. Kim, P. Fay, S. Nakamura, S.P. DenBaars, U.K. Mishra, and S. Keller, J. Appl. Phys. **121**, 185707 (2017).

[107] S. Wienecke, B. Romanczyk, M. Guidry, H. Li, E. Ahmadi, K. Hestroffer, X. Zheng, S. Keller, and U.K. Mishra, IEEE Electron Device Lett. **38**, 359 (2017).

[108] Y.F. Ng, Y.G. Cao, M.H. Xie, X.L. Wang, and S.Y. Tong, Appl. Phys. Lett. **81**, 3960 (2002).

[109] E. Bellet-Amalric, C. Adelmann, E. Sarigiannidou, J.L. Rouvière, G. Feuillet, E. Monroy, and B. Daudin, J. Appl. Phys. **95**, 1127 (2004).

[110] A. Yoshikawa, N. Hashimoto, N. Kikukawa, S.B. Che, and Y. Ishitani, Appl. Phys. Lett. **86**, 153115 (2005).

[111] Q. Sun, C.D. Yerino, T.S. Ko, Y.S. Cho, I.-H. Lee, J. Han, and M.E. Coltrin, J. Appl. Phys. **104**, 93523 (2008).

[112] Y.H. Phang, C. Teichert, M.G. Lagally, L.J. Peticolos, J.C. Bean, and E. Kasper, Phys. Rev. B **50**, 14435 (1994).

[113] J. Tersoff, Y.H. Phang, Z. Zhang, and M.G. Lagally, Phys. Rev. Lett. **75**, 2730 (1995).

[114] M. Shinohara and N. Inoue, Appl. Phys. Lett. **66**, 1936 (1995).

[115] J. Mysliveček, C. Schelling, F. Schäffler, G. Springholz, P. Šmilauer, J. Krug, and B.

Voigtländer, Surf. Sci. **520**, 193 (2002).

[116] H. Lu, W.J. Schaff, L.F. Eastman, and C.E. Stutz, Appl. Phys. Lett. **82**, 1736 (2003).

[117] T.D. Veal, L.F.J. Piper, I. Mahboob, H. Lu, W.J. Schaff, and C.F. McConville, Phys. Status Solidi C **2**, 2246 (2005).

[118] P.D.C. King, T.D. Veal, C.S. Gallinat, G. Koblmüller, L.R. Bailey, J.S. Speck, and C.F. McConville, J. Appl. Phys. **104**, 103703 (2008).

[119] C.H. Swartz, R.P. Tompkins, N.C. Giles, T.H. Myers, H. Lu, W.J. Schaff, and L.F. Eastman, J. Cryst. Growth **269**, 29 (2004).

[120] I. Mahboob, T.D. Veal, C.F. McConville, H. Lu, and W.J. Schaff, Phys. Rev. Lett. **92**, 36804 (2004).

[121] P.D.C. King, T.D. Veal, and C.F. McConville, J. Phys. Condens. Matter **21**, 174201 (2009).

[122] T.B. Fehlberg, G. Koblmüller, G.A. Umana-Membreno, C.S. Gallinat, B.D. Nener, J.S. Speck, and G. Parish, Phys. Status Solidi B **245**, 907 (2008).

[123] C. Stampfl, C. Van de Walle, D. Vogel, P. Krüger, and J. Pollmann, Phys. Rev. B **61**, R7846 (2000).

[124] T.K. Sharma and E. Towe, Appl. Phys. Lett. **96**, 191105 (2010).

[125] S.-H. Park, Y.-T. Moon, J.S. Lee, H.K. Kwon, J.S. Park, and D. Ahn, Phys. Status Solidi A **208**, 195 (2011).

[126] J. Zhang and N. Tansu, J. Appl. Phys. **110**, 113110 (2011).

[127] M. Shimizu, Y. Kawaguchi, K. Hiramatsu, and N. Sawaki, Solid-State Electron. **41**, 145 (1997).

[128] L.-H. Yang, B.-H. Zhang, and F.-Q. Guo, Chinese Phys. Lett. **30**, 47301 (2013).

[129] Y. Liu, D. Chen, J. Xue, B. Liu, H. Lu, R. Zhang, Y. Zheng, K. Xu, J. Zhang, B. Cui, A.M. Wowchak, and A.M. Dabiran, J. Vac. Sci. Technol. B **30**, 30603 (2012).

[130] A.M. Fischer, Y.O. Wei, F.A. Ponce, M. Moseley, B. Gunning, and W.A. Doolittle, Appl. Phys. Lett. **103**, 131101 (2013).

[131] J. Däubler, T. Passow, R. Aidam, K. Köhler, L. Kirste, M. Kunzer, and J. Wagner, Appl. Phys. Lett. **105**, 111111 (2014).

[132] K. Kumakura, T. Makimoto, and N. Kobayashi, J. Appl. Phys. **93**, 3370 (2003).

[133] H. Wang, D.S. Jiang, U. Jahn, J.J. Zhu, D.G. Zhao, Z.S. Liu, S.M. Zhang, Y.X. Qiu, and H. Yang, Physica B **405**, 4668 (2010).

[134] K. Pantzas, G. Patriarche, G. Orsal, S. Gautier, T. Moudakir, M. Abid, V. Gorge, Z. Djebbour, P.L. Voss, and A. Ougazzaden, Phys. Status Solidi A **209**, 25 (2012).

[135] D. Fujita, T. Miyatake, T. Shinagawa, Y. Abe, K. Murakami, B. Li, H. Matsumoto, S. Murayama, N. Okada, and K. Tadatomo, Phys. Status Solidi C **7**, 2063 (2010).

[136] N. Okada, Y. Yamada, and K. Tadatomo, J. Appl. Phys. **111**, 2 (2012).

[137] S. Keller, C. Schaake, N.A. Fichtenbaum, C.J. Neufeld, Y. Wu, K. McGroddy, A. David, S.P. DenBaars, C. Weisbuch, J.S. Speck, and U.K. Mishra, J. Appl. Phys. **100**, 54314 (2006).

[138] S. Keller, N.A. Fichtenbaum, C. Schaake, C.J. Neufeld, A. David, E. Matioli, Y. Wu, S.P. DenBaars, J.S. Speck, C. Weisbuch, and U.K. Mishra, Phys. Status Solidi B **244**, 1797 (2007).

[139] O. Landré, D. Camacho, C. Bougerol, Y.M. Niquet, V. Favre-Nicolin, G. Renaud, H. Renevier, and B. Daudin, Phys. Rev. B **81**, 153306 (2010).

[140] S.C. Jain, M. Willander, and H. Maes, Semicond. Sci. Technol. **11**, 641 (1996).

[141] U. Pietsch, V. Holý, and T. Baumbach, in *High-Resolution X-Ray Scatt.* (Springer New York, New York, NY, 2004), pp. 179–203.

[142] R.M. Farrell, C.J. Neufeld, S.C. Cruz, J.R. Lang, M. Iza, S. Keller, S. Nakamura, S.P. Denbaars, U.K. Mishra, and J.S. Speck, Appl. Phys. Lett. **98**, 201107 (2011).

[143] F. Glas, Phys. Rev. B **74**, 121302 (2006).

[144] X. Zhang, V.G. Dubrovskii, N. V. Sibirev, and X. Ren, Cryst. Growth Des. **11**, 5441 (2011).

[145] S.J. Hearne, J. Han, S.R. Lee, J.A. Floro, D.M. Follstaedt, E. Chason, and I.S.T. Tsong, Appl. Phys. Lett. **76**, 1534 (2000).

[146] S. Srinivasan, L. Geng, R. Liu, F.A. Ponce, Y. Narukawa, and S. Tanaka, Appl. Phys. Lett. **83**, 5187 (2003).

[147] L. De Caro and L. Tapfer, Phys. Rev. B **49**, 11127 (1994).

[148] Q. Shen, S.W. Kycia, E.S. Tentarelli, W.J. Schaff, and L.F. Eastman, Phys. Rev. B **54**,

16381 (1996).

[149] L. Leprince, G.T. Baumbach, A. Talneau, M. Gailhanou, and J. Schneck, Appl. Phys. Lett. **71**, 3227 (1997).

[150] D. Lübbert, T. Baumbach, S. Ponti, U. Pietsch, L.L.J. Schneck, and A. Talneau, Europhys. Lett. **46**, 479 (1999).

[151] A.C. Abare, M.A. Hansen, J.S. Speck, S.P. DenBaars, and L.A. Coldren, Electron. Lett. **35**, 1559 (1999).

[152] A.C. Abare, PhD Thesis, University of California, Santa Barbara, 2000.

[153] J. Pal, M.A. Migliorato, C.-K. Li, Y.-R. Wu, B.G. Crutchley, I.P. Marko, and S.J. Sweeney, J. Appl. Phys. **114**, 73104 (2013).

[154] Y.K. Ooi and J. Zhang, AIP Adv. **5**, 57168 (2015).

[155] S. Keller, C. Lund, T. Whyland, Y. Hu, C. Neufeld, S. Chan, S. Wienecke, F. Wu, S. Nakamura, J.S. Speck, S.P. DenBaars, and U.K. Mishra, Semicond. Sci. Technol. **30**, 105020 (2015).

[156] K. Hestroffer, F. Wu, H. Li, C. Lund, S. Keller, J.S. Speck, and U.K. Mishra, Semicond. Sci. Technol. **30**, 105015 (2015).

[157] K. Hestroffer, C. Lund, H. Li, S. Keller, J.S. Speck, and U.K. Mishra, Phys. Status Solidi B **253**, 626 (2016).

[158] K. Hestroffer, C. Lund, O. Koksaldi, H. Li, G. Schmidt, M. Trippel, P. Veit, F. Bertram, N. Lu, Q. Wang, J. Christen, M.J. Kim, U.K. Mishra, and S. Keller, J. Cryst. Growth **465**, 55 (2017).

[159] K.N. Lee, S.M. Donovan, B. Gila, M. Overberg, J.D. Mackenzie, C.R. Abernathy, and R.G. Wilson, J. Electrochem. Soc. **147**, 3087 (2000).

[160] N. Kobayashi, T. Makimoto, Y. Yamauchi, and Y. Horikoshi, J. Appl. Phys. **66**, 640 (1989).

[161] S. Keller, U.K. Mishra, and S.P. Denbaars, J. Electron. Mater. **26**, 1118 (1997).

[162] B. Bonef, M. Catalano, C. Lund, S.P. Denbaars, S. Nakamura, U.K. Mishra, M.J. Kim, and S. Keller, Appl. Phys. Lett. **110**, 143101 (2017).

[163] G. Parish, S. Keller, S.P. Denbaars, and U.K. Mishra, J. Electron. Mater. **29**, 15 (2000).

[164] N. Kobayashi and T. Makimoto, Jpn. J. Appl. Phys. **24**, L824 (1985).

[165] M.. Kappers, M.. Warddrip, and R.. Hicks, J. Cryst. Growth **191**, 332 (1998).

[166] L.M. Dyagileva, V.P. Mar'in, E.I. Tsyganova, and G.A. Razuvaev, J. Organomet. Chem. **175**, 63 (1979).

[167] G. Namkoong, W.A. Doolittle, and A.S. Brown, Appl. Phys. Lett. **77**, 4386 (2000).

[168] U. Kaufmann, P. Schlotter, H. Obloh, K. Köhler, and M. Maier, Phys. Rev. B **62**, 10867 (2000).

[169] Y.T. Moon, D.J. Kim, K.M. Song, C.J. Choi, S.H. Han, T.Y. Seong, and S.J. Park, J. Appl. Phys. **89**, 6514 (2001).

[170] C.E.C. Wood, G. Metze, J. Berry, and L.F. Eastman, J. Appl. Phys. **51**, 383 (1980).

[171] K. Ploog, J. Cryst. Growth **81**, 304 (1987).

[172] S.P. Guo, W. Lin, X. Zhou, M.C. Tamargo, C. Tian, I. Kuskovsky, and G.F. Neumark, J. Appl. Phys. **90**, 1725 (2001).

[173] H. Wang, J. Liu, N. Niu, G. Shen, and S. Zhang, J. Cryst. Growth **304**, 7 (2007).

[174] C. Simbrunner, M. Wegscheider, M. Quast, T. Li, A. Navarro-Quezada, H. Sitter, A. Bonanni, and R. Jakiela, Appl. Phys. Lett. **90**, 142108 (2007).

[175] C. Bayram, J.L. Pau, R. McClintock, and M. Razeghi, J. Appl. Phys. **104**, 83512 (2008).

[176] Y. Chen, H. Wu, G. Yue, Z. Chen, Z. Zheng, Z. Wu, G. Wang, and H. Jiang, Appl. Phys. Express **6**, 41001 (2013).

[177] M.L. Nakarmi, K.H. Kim, J. Li, J.Y. Lin, and H.X. Jiang, Appl. Phys. Lett. **82**, 3041 (2003).

[178] Y. Chen, H. Wu, E. Han, G. Yue, Z. Chen, Z. Wu, G. Wang, and H. Jiang, Appl. Phys. Lett. **106**, 162102 (2015).

[179] T. Li, C. Simbrunner, M. Wegscheider, A. Navarro-Quezada, M. Quast, K. Schmidegg, and A. Bonanni, J. Cryst. Growth **310**, 13 (2008).

[180] P. Kozodoy, PhD Thesis, University of California, Santa Barbara, 1999.

Appendix: Key Growth Recipes

Sample	Description	Section in thesis
150928an	N-polar $In_{0.46}Ga_{0.54}N$/GaN 3QW	2.1
160415bn	N-polar $In_{0.3}Ga_{0.7}N$ tunnel diode with 370 nm p-GaN	2.5
160707bn	N-polar GaN/4.5 nm $In_{0.3}Ga_{0.7}N$/GaN TFET	2.1
170426bi	N-polar InN layer, 20 nm	3.1
170111ar	N-polar 200 nm digital InGaN regrowth on MBE InGaN PS	5.2
170302an	N-polar p-n junction with ∂-doped p-layer	7.3